Wave Propagation in Nonlinear Systems of Coupled Oscillators

by

Brian P. Bernard

Department of Mechanical Engineering and Materials Science
Duke University

Date: _____

Approved:

_____
Brian P. Mann, Supervisor

_____
Lawrence Virgin

_____
Laurens Howle

_____
Steven Cummer

Dissertation submitted in partial fulfillment of the requirements for the degree of Doctor of Philosophy in the Department of Mechanical Engineering and Materials Science
in the Graduate School of Duke University
2014

Abstract

Wave Propagation in Nonlinear Systems of Coupled Oscillators

by

Brian P. Bernard

Department of Mechanical Engineering and Materials Science
Duke University

Date: _____

Approved:

_____
Brian P. Mann, Supervisor

_____
Lawrence Virgin

_____
Laurens Howle

_____
Steven Cummer

An abstract of a dissertation submitted in partial fulfillment of the requirements for the degree of Doctor of Philosophy in the Department of Mechanical Engineering and Materials Science
in the Graduate School of Duke University
2014

Abstract

Mechanical oscillators form the primary structure of a wide variety of devices including energy harvesters and vibration absorbers, and also have parallel systems in electrical fields for signal processing. In the area of wave propagation, recent study in periodic chains have focused on active tuning methods to control bandgap regions, bands in the frequency response in which no propagating wave modes exist. In energy harvesting, several coupled systems have been proposed to enhance the peak power or bandwidth of a single harvester through arrays or dynamic magnification. Though there are applications in several fields, the work in this dissertation can all fit into the category of coupled non-linear oscillators. In each sub-field, this study demonstrates means to advance state of the art techniques by adding nonlinearity to a coupled system of linear oscillators, or by adding a coupled device to a nonlinear oscillator.

The first part of this dissertation develops the analytical methods for studying wave propagation in nonlinear systems. A framework for studying rotational systems is presented and used to design an testbed for wave propagation experiments using a chain of axially aligned pendulums. Standard analytical methods are also adapted to allow uncertainty analysis techniques to provide insight into the relative impact of variations in design parameters. Most analytical insight in these systems is derived from a linearlized model and assumes low amplitude oscillations. Additional study on the nonlinear system is performed to analyze the types of deviations from this

behavior that would be expected as amplitudes increase and nonlinear effects become more prominent.

The second part of this dissertation describes and demonstrates the first means of passive control of bandgap regions in a periodic structure. By imposing an asymmetrical bistability to an oscillator in each unit cell, it is analytically shown that each potential well has different wave propagation behaviors. Experimental demonstrations are also provided to confirm the simulated results.

The final section performs analytical and numerical analysis of a new system design to improve the performance of a nonlinear energy harvester by adding an excited dynamic magnifier. It is shown that this addition results in higher peak power and wider bandwidth than the uncoupled harvester. Unlike standard dynamic magnifiers, this performance does not come at the expense of power efficiency, and unlike harvester arrays, does not require the added cost of multiple energy harvesters. Most importantly, in the frequency range with coexisting solutions, it improves upon the nonlinear harvester's primary limitation by making the high amplitude solution much easier to achieve with a significantly expanded basin of attraction.

Contents

List of Tables

List of Figures

Acknowledgements

Two of the first graduate students I met when I visited Duke were Sam Stanton and Firas Khasawneh. Though they may not have realized how important their advice was at the time (and in fact it was two years before I realized it myself), I owe them a significant debt. Some students enter graduate school with set projects and advisors and can quickly succeed. When my progress appeared to stall, their advice was extremely helpful. Their persistence paid off, and ever since I joined Brian Mann's Nonlinear Dynamics Group, my trajectory has been upward.

There couldn't have been a more perfect advisor for me than Brian. Each professor has their own styles of teaching and mentorship, and he's been a role model for exactly the type of professor I will strive to be. He cares about teaching and enjoys his time in the classroom and in developing new projects. We have similar views on the importance of work-life balance and of the importance of teaching and working with undergraduates, something that I'm glad to have been given the opportunity to continue doing. Jeffrey Peyser, Jake Greenstein, and Charlie Arentzen, the three Pratt Fellows I supervised over the past three years, all complemented my research style and together we were able to accomplish far more than we would have done separately. Even with prioritizing family and being an effective teacher, Brian has still shown research excellence and instilled in me the standards expected to publish, obtain funding, and increase my standing in the community. I think I still have room for improvement in this area, but he has shown confidence in me when I needed it.

I hope to continue working with him as a collaborator and that my future students have as much regard for me as I have for him.

I'd also like to thank my other committee members for their help over the past several years. Lawrie Virgin has driven my preparation far more than he may realize from our limited interactions. Most projects have multiple possible avenues that could be investigated, each with different possible paths to completion. Lawrie always seems to be most interested in the ones I chose not to pursue. Going forward, more carefully considering those questions will help me in preparing to teach my classes and lead a research group. There were several times when I seriously considered joining Laurens Howle's lab group both before and after starting at Duke, and had I not joined Brian Mann, I'm sure I could also have been very happy and successful working with him. We've gotten along great inside class and out, and he has been a great resource for advice during my job hunt and in preparation for my upcoming job. I invited Steven Cummer to join my committee since there was some overlap between our fields and I had hoped to be able to leverage that to expand my work slightly or even collaborate with a student in his research lab. I'm disappointed a good time for this never presented itself, but nonetheless glad to have had him on the committee in case the opportunity presents itself in the future.

There are two groups of collaborators that I'd also like to thank. The Michigan State University group of Brian Feeny and Smruti Panigrahi approached us to do experimental work with them. Our project has proceeded extremely slowly as priorities have shifted and other more urgent projects have displaced them, but I do hope that we are able to finish in the future. The University of Florida group of David Arnold and Nicolas Garraud joined us at the perfect time and provided a lot of help in a recent article submission and I hope I am able to return the favor during their upcoming work.

When it comes to troubleshooting, I've developed a two-stage process to work my

way through seemingly simple problems that have for some reason gotten me stuck. The first step is to draw it on the whiteboard in our office and ask Charlie Freundlich and Andrew Schicho to let me know if anything I put up is obviously wrong for some trivial reason that I didn't notice. If they fail to spot the error, I move over to Ben Owens and Genevieve Lipp's office and ask them. They've all helped me out in several instances, and saved me lots of time in troubleshooting code, equations or block diagrams. I can't remember any times that none of them were able to solve the issue, but if it happened, it was probably because I was proposing something that was impossible and had no answer.

Dennis Tweten, Zach Ballard, and Clark McGehee, these students were the carrot. They were just far enough ahead of me in their degrees that I could never catch up to them, but close enough that they were still able to urge me forward. Clark helped me out with setting up experiments, Dennis was always willing to look at some equations with me, and Zach came to basketball games with me, which is equally important at Duke. They showed me the importance of having students at different stages of degree completion in a lab, and a lot of my training occurred through their turnover.

I hope that I was able to be similarly helpful to Michael Mazzoleni, since he has been a great addition to the lab. There's nothing better for a PhD student trying to finish up than a fellow student who approaches and says "what can I do to help?", and that's what Michael did this spring. He's a quick learner and forthcoming in his skills, able to ask for step-by-step help when he needs it or go off and work on his own once he's got the hang of it. I hope to continue collaborations with him and Brian over the next several years as I work to try and setup my own lab at Schreiner.

In my job search, Brian Mann, Scott Calvert, Laurens Howle and Lawrie Virgin all agreed to write recommendation letters for me. I had an extremely successful job search, with many interviews at a wide variety of schools, and I know that these would not have happened if you all hadn't written kind words on my behalf. And

though no one admitted to making any extra calls or emails to help me get an inside track anywhere I will throw in a thank you anyway, because I do appreciate it. Schreiner will be quite a bit different than Duke or Stanford, but the match was obvious as soon as I arrived for the interview, so I couldn't be happier or more excited about starting there.

Doug James and Steve Shapiro also provided essential help in my job search and faculty preparation. I would not have been prepared for the Schreiner interview if I hadn't spent time with Steve at Guilford, which is very similar. When it came to the faculty job search, through PFF and CCT courses, Doug answered most of the questions that I didn't even realize I had, and gave me an advantage over my peers who were not involved in similar programs.

Finally, none of my work would have been possible without financial support. The Army Research Office and Office of Naval Research provided the bulk of my tuition and fellowship, so I hope that my future research and teaching will demonstrate that their investment paid off. The National Science Foundation also covered travel expenses to a recent conference so I'd also like to thank them for what turned out to be a very productive trip. It can be tough to leave a high paying job to return to graduate school and the change in lifestyle could have been disruptive, but the James B. Duke 100th Anniversary Fund and Department of Veterans Affairs each provided extra stipend amounts, and I've been very happy to be a 'slightly less poor' grad student over the past few years.

I'll add one more name in Kathy Parrish. I know that there's a ton of paperwork and bureaucracy in running a university. That I've been shielded from it and been able to focus on my work is no doubt a testament to your effectiveness. To all the other graduate students, professors, administrators, friends and anyone else that have helped me along the way, here is a blanket apology for not identifying you by name, and a thank you for all your help.

1

Introduction

Within the past two decades, energy manipulation has become an increasingly important area of study in a variety of applications. The signal processing field is interested in wave propagation and wave shaping for modern wireless devices. Mechanical systems often require wave attenuation to minimize vibrations. Energy harvesters may instead prefer to reshape a signal in order to increase the amount that can be captured.

This dissertation primarily focuses on fundamental research into the field of energy manipulation, specifically the ways in which nonlinear systems of coupled oscillators can provide design advantages for propagation, attenuation, or other manipulation of an energy source. Each system studied can be represented by a block diagram similar to Fig. 1.1. Though mechanical oscillators are modeled, mathematically equivalent systems are also seen in other areas such as granular chains [2–4] and signal processing applications [5].

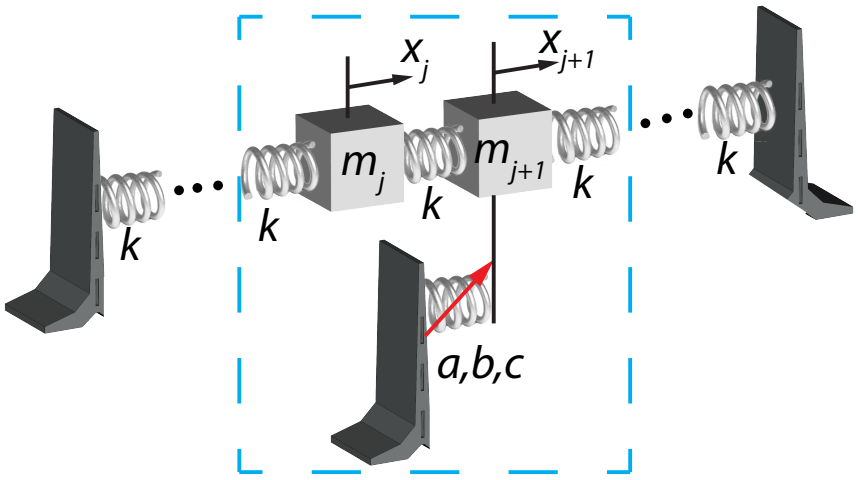

FIGURE 1.1: General block diagram of a 1D chain of coupled oscillators representing the specific system of Chapter 3, but which is qualitatively similar to the model for every chapter. The spring connecting two masses is referred to as the coupling stiffness, and the spring connecting a mass to ground is the restoring stiffness or on-site stiffness. Fixed boundary conditions are shown here, though some systems in this dissertation will use free boundary conditions.

1.1 Coupled Oscillators Background

The background concept most important in Chapters 2-5 is the bandgap. In studying wave propagation applications [6–9], a system's frequency response is generally divided into two possible classifications, propagation or attenuation [10, 11]. In a propagation zone (or pass band), wave propagation occurs, and the signal is transmitted through the chain. In an attenuation zone (or stop band), the signal degrades along the length of the chain and is not fully transmitted. For discrete chains with periodically repeating segments called unit cells [12], when all masses and stiffness are identical, a 1D chain will typically have a single propagation zone with a maximum frequency, and above that frequency an attenuation zone. A bandgap forms when asymmetry [13] is introduced in the form of a changed mass or an introduced defect [14, 15]. This bandgap splits the single propagation zone into two (in the case of a dimer chain) or more (in the case of longer unit cells) propagation zones, each

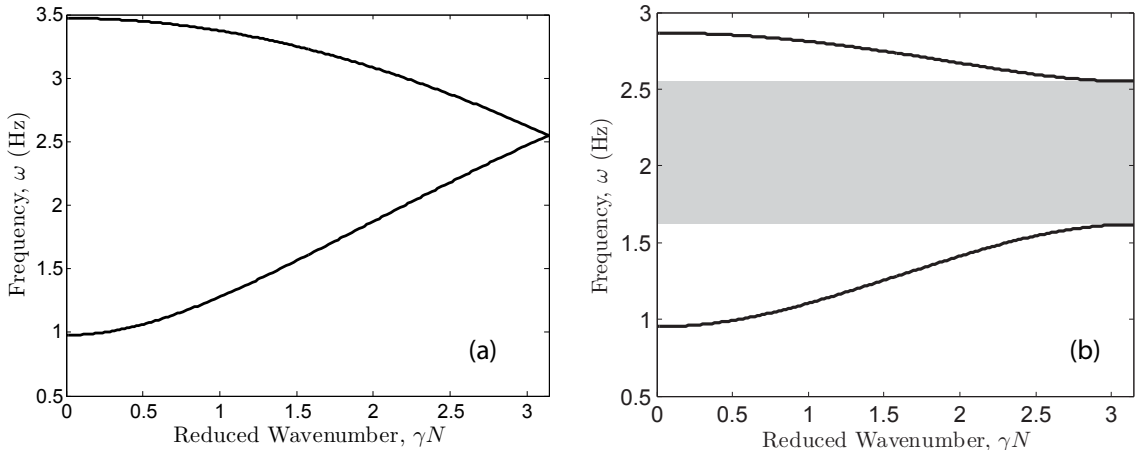

FIGURE 1.2: Frequency response for the system of Chapter 4. (a) When all masses are identical, 1.0-3.5 Hz is a single propagation zone in this example. (b) When two masses comprising a unit cell are different, a central bandgap (shaded) separates the two propagation zones.

separated by a narrow attenuation zone which is referred to as a bandgap.

Theoretically, bandgap regions can be calculated for linear chains through analyzing a single unit cell. By modeling the cell as a circulant matrix, the system represents an infinite chain. The eigenvalue problem [16] can then be solved for frequency in terms of the wave number using the propagation constant technique [17]. Figure 1.2 shows an example solution for the system of Chapter 4. This type of plot will be shown throughout the dissertation as it provides fundamental insight into the behavior of the system. The most important information on this plot is derived from the vertical axis, frequency. Each frequency at which a solution exists is a propagation zone for that frequency. Where there is no solution for any wave number, the system has an attenuation zone at that frequency. The specific wave number that corresponds to a given frequency can provide additional information about the solution, for example phase difference between adjacent oscillators, but this aspect will not be a focus of the following research.

Though bandgaps in linear systems are well understood, nonlinear systems are

still an active research area. The previously mentioned propagation constant technique does not fully describe nonlinear behaviors [18] and only gives reasonable approximations for linearized models with low amplitude oscillations [19]. However, intentionally introducing nonlinearities can provide additional functionality not possible in linear counterparts [20]. Previous work in this area has focused on active control techniques to manipulate bandgap regions through parameter tuning [21–23], component replacement [24–26], or the application of external forces [27]. The following chapters will supplement these techniques by demonstrating a method of passive control as well as by providing a framework for performing uncertainty analysis.

The study of coupled oscillators expands beyond the field of wave propagation. The final chapter of this dissertation will apply some related techniques to the field of energy harvesting. Like wave propagation, active research in this field has moved beyond the well understood linear case and is instead focused on the benefits of intentionally introduced nonlinearities [28]. Two of the most promising paths are the bistable oscillator [29–31] in which multiple stable solutions can coexist in each potential well or cross-well, and the hardening-type oscillator [1, 32–34] in which the frequency response is curved such that higher amplitude solutions occur at higher frequencies allowing a wider solution bandwidth than the narrowband linear case.

Previous research in introducing coupling into energy harvesting applications have been in the areas of dynamic magnification and arrays [35–37]. Addition of a dynamic magnifier can be thought of as the reverse of the classic dynamics problem of adding a vibration absorber to an excited mass. Here, the dynamic magnifier can be added between the harvester and excitation source [38–41], or on the outside of the harvester [42], and it's purpose is to be tuned such as to amplify the harvester's response. Though several systems have been able to improve a harvester's peak power, this has come at the expense of power per unit mass in some cases, and through changing the response frequency in others [43, 44].

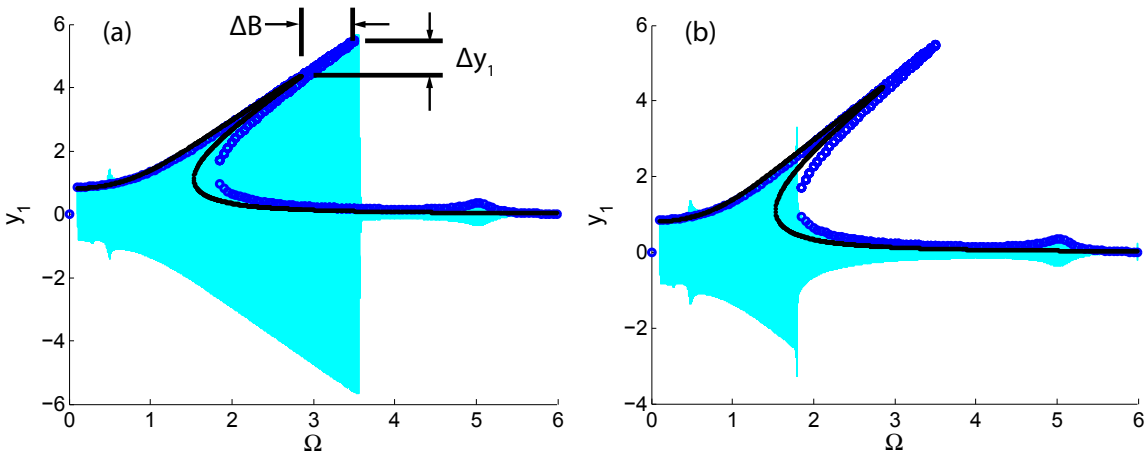

FIGURE 1.3: Cyan (light gray shaded) area represents (a) forward and (b) reverse frequency sweeps for a hardening-type energy harvester with excited dynamic magnifier, as described in Chapter 6. The solid black line shows the standalone energy harvester for reference, and the blue open circles show the analytical solution of the coupled system, highlighting the expanded bandwidth and increased amplitude.

Arrays of oscillators are different than dynamic magnifiers in that all masses are directly connected to the excitation source, and all are capable of harvesting energy [45–47]. A common array model mis-tunes each oscillator to a different natural frequency, so that the overall system has a wide bandwidth, even though only a small number of harvesters would be active at any given frequency. The primary drawback of this type of system is obviously cost since the harvesters are the most expensive component, and it is cost-inefficient to have idle harvesters. The final chapter of this dissertation combines the array and magnifier models to investigate the so-called excited dynamic magnifier. Figure 1.3 shows an example performance improvement of excited dynamic magnification over a standalone nonlinear harvester.

1.2 Research Contributions

The objective of this work is to theoretically and experimentally investigate the behavior of nonlinearly coupled oscillators and the mechanisms by which they manipulate energy, specifically contrasting against either uncoupled systems or linearly

coupled systems. Simplicity is generally preferred in mechanical systems. Fewer or more basic moving components typically result in a less expensive and more robust product. However, there can be cases where the addition of such parts can significantly improve performance. The following sections describe advantageous phenomena that can occur with nonlinear coupling that are not present in their linear counterparts, and where the addition of a coupled oscillator can significantly improve the performance of the previously standalone device.

1.2.1 Uncertainty Propagation

The propagation constant technique has previously been used to predict band gap regions in linear oscillator chains by solving an eigenvalue problem for frequency in terms of a wave number. This chapter describes a method by which selected design parameters can be separated from the eigenvalue problem, allowing standard uncertainty propagation techniques to provide closed form solutions for the uncertainty in frequency. Examples are provided for different types of measurement or environmental uncertainty showing the varying robustness of a band gap region to changes in parameters of the same or different order. The system studied in this paper is comprised of repelling magnetic oscillators using a dipole model and has been the basis for follow up study in solitary waves [48]. Numerical simulation has been performed to confirm the accuracy of analytical solutions up to a certain level of base excitation amplitude after which nonlinear effects change the predicted band gap regions to low energy chaos.

1.2.2 Passive Reconfiguration

Current periodic structures are constrained to have fixed energy transmission behavior unless active control or component replacement is used to alter their wave propagation characteristics. The introduction of nonlinearity to generate multiple

stable equilibria is an alternative strategy for realizing distinct energy propagation behaviors. A reconfigurable bandgap system is created by implementing passive switching between multiple stable states of equilibrium, to alter the level of energy attenuation in response to environmental stimuli. The ability to avoid potentially catastrophic loads is demonstrated by tailoring the band pass and bandgap regions to coalesce for two stable equilibria and varying an external load parameter to trigger a bifurcation. The proposed phenomenon could be utilized in remote or autonomous applications where component modifications and active control are impractical.

1.2.3 Propagation in a Rotational System

Wave propagation and energy absorption are studied in a 1D array of axially aligned pendulums under various forms of base excitation. In the system studied, each pair of pendulums comprising a single unit cell is connected through linear torsional coupling, and asymmetry is introduced by varying their masses. Similar to translational systems, when subjected to harmonic base excitation, band gaps are observed in this rotational system over predictable frequency ranges. It is observed that varying the uncoupled restoring force parameters (mass and gravitational strength) shifts the expected band gap regions under harmonic excitation. This asymmetry in pendulum masses can also be exploited for the purposes of energy absorption when the system is subjected to base excitation in the form of an impulse. Numerical simulations are performed to demonstrate the accuracy of analytical solutions for both types of external forcing.

1.2.4 Experimental Passive Bandgap Reconfiguration

By applying an asymmetric on-site restoring force in a 1D chain of oscillators, we demonstrate experimentally that a morphing in the bandgap structure or passive bandgap reconfiguration can be triggered by an increase in environmental excitation

amplitude. Recent studies on wave propagation have focused on new capabilities and behaviors resulting from intrinsic nonlinearities. This chapter details a bistable experimental design that achieves amplitude dependent filtering through passive bandgap reconfiguration which is triggered by a bifurcation. The system studied comprises a 1D chain of axially aligned pendulums in dimer unit cells with geometrically nonlinear nearest neighbor coupling where bistability is induced through repulsive magnets. When the bistability is asymmetric, each potential well has a different linear spectra. Though this paper uses mechanically coupled oscillators as an example, the phenomenon itself could be used in any wave propagation media where asymmetric bistability can be implemented.

1.2.5 Excited Dynamic Magnification

Dynamic magnifiers and coupled harvester arrays are two strategies that have been developed over the past decade to improve peak power and bandwidth as compared to a single tuned energy harvester. However, both of these methods come with drawbacks. Dynamic magnifiers require retuning since they change peak response frequency of the driven oscillator and some designs result in decreased power per unit mass. Coupled harvester arrays' increased bandwidth include central valleys between peaks and also significantly increase system cost. This chapter will describe an excited dynamic magnifier which borrows design characteristics from both traditional dynamic magnifiers and harvester arrays in order to overcome these drawbacks. A hardening-type tuned energy harvester with excited dynamic magnifier can achieve higher peak power, greater power per unit mass, and wider bandwidth without the need for retuning and for a minimal added cost as compared to the uncoupled harvester. It also significantly improves upon the performance of an uncoupled nonlinear harvester in the frequency range of coexisting solutions by expanding the basin of attraction for the high amplitude solution.

1.3 Thesis Organization

This dissertation is thematically grouped into three different sections. Chapters 2 and 3 are the first section and they propose new analytical and numerical techniques for studying energy manipulation. Chapter 2 describes a method for rearranging the standard form of systems of wave propagation equations in order to allow the application of standard uncertainty propagation techniques. It also numerically qualifies behavior of nonlinear systems, and contrasts them with linearized models, specifically noting areas in solution space that are more or less robust to nonlinearity. Chapter 3 describes a method of passive bandgap reconfiguration through asymmetric bistability within each unit cell.

Chapters 4 and 5 then build off this theoretical foundation by developing and testing an experimental testbed to confirm the viability of passive bandgap reconfiguration. Chapter 4 describes the beneficial features of using a chain of axially aligned pendulums for studying wave propagation. Chapter 5 then consists primarily of experimental demonstration of the passive bandgap reconfiguration phenomenon.

Finally, Chapter 6 transitions into the field of energy harvesting. Unlike the previous chapters which all focused on chains of repeating unit cells, this section focuses instead at the more basic level of introducing coupling to extend the system beyond a single oscillator. This analytical and numerical model predicts significant improvement in peak power and bandwidth of a hardening type energy harvester when the added excited dynamic magnifier is tuned to have its natural frequency slightly greater than the peak frequency of the uncoupled harvester.

2

Uncertainty Propagation in the Bandgap Structure of a 1D Array of Magnetically Coupled Oscillators

2.1 Introduction

Wave propagation is a commonly studied area with applications in acoustics, optics, and vibrations. Depending on the application, it may be desirable to minimize wave propagation for purposes of energy absorption or wave guiding. Waves are normally modeled using harmonic vibration of repeated elements. For the present study, wave propagation occurs along a path in which the repeated elements exhibit only nonlinear coupling and have no independent restoring forces.

Much of the current research in energy absorbtion can be traced back to the study of elementary granular collisions of simple one dimensional waves analytically [2, 6, 8, 9], numerically [7] and experimentally [3, 4]. Decorated and tapered diameter chains showed significantly better impulse absorption properties than the uniform case [49–52]. Though this chapter primarily focuses on the linear regime of a nonlinear system, several recent works on similar nonlinear systems provided fundamental insight of the differing expected behaviors. These include work on nonlinear solitary

waves in compressed granular chains [27] and strongly nonlinear traveling waves in uncompressed homogenous chains [53].

A well documented method of absorption of vibrational base excitation is through the identification of band gaps [12], frequency ranges in which no propagating wave modes exist [13]. An elegant solution method for linear problems, that formed the basis for Section 2.4, was derived in Ref. [17] and extended to doubly periodic structures in Ref. [54], in which a traveling wave solution form is assumed and the model reduces to a standard eigenvalue problem. Ref. [16] connects the granular chain studies to this band gap research through analysis of realistic discontinuous interactions such as loss of contact between adjacent beads.

Furthering band gap research, the typical linear mass-spring model was advanced by including an additional cubic spring that was solved using a nonlinear map approach [55]. In Ref. [56], perturbation analysis was performed on a similar nonlinear mass-spring model which identified amplitude dependent behavior that was not observed in the previous linear cases, but was also observed in the nonlinear system of this chapter. Experimental validation of nonlinear band gaps occurred through measuring wave propagation along a diatomic chain of steel and aluminum balls under Hertzian contact [57]. The standing wave solution form (applicable in attenuation zones) was solved using nonlinear normal modes against the more common traveling wave form (applicable in propagation zones) which was solved using a multiple scales perturbation analysis in Ref. [19].

In contrast to many prior works that used generic springs to represent the restoring forces, this chapter models magnetic interactions to provide nonlinear coupling between adjacent elements. The most common models for magnetic forces are the electric loop model [58], in which the magnet is assumed to be a dipole at its center of mass, and the point charge model in which it is modeled as two monopoles at opposite edges of its mass. Analytical comparisons of these two models confirmed that

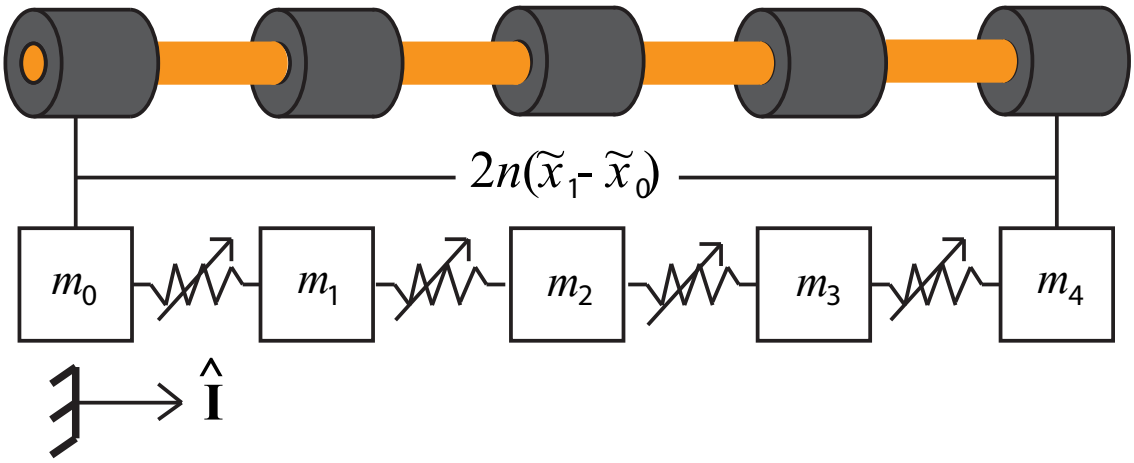

FIGURE 2.1: An example configuration showing $n = 2$ unit cells

as the separation distance between magnets increased, these two models converge to the same value [59]. Due to the centralization of the forces at a single point, the dipole model is simpler to use in practice, and experimental validation has shown this model is accurate for distances greater than the size of the magnet [60].

The rest of the chapter is organized as follows. Sections 2.2-2.3 describe the physical system and its mathematical model, respectively. Section 2.4 derives analytical solutions for small oscillations about a nonlinear static equilibrium. Section 2.5 then performs uncertainty analysis on the analytically predicted band gap regions for changes in selected parameters. Finally, Section 2.6 uses numerical simulation to study the nonlinear effects of increased excitation amplitude.

2.2 System Description

A schematic of the hypothetical system is shown in Fig. 2.1. The primary components of the system were modeled as grade N42 cylindrical ring magnets on a rigid inner rail. Magnets were added in pairs, with one adjacent pair of magnets comprising a single unit cell. Though identical magnets are used for each oscillator, differences were introduced, such as adding an external mass to one magnet, in order to create

Table 2.1: Constants used in numerical simulations

Name	Designation	Value
Mass	m	.04 kg
Volume	V	$1.51 \cdot 10^{-6}$ m^3
Magnetization	M	$1.05 \cdot 10^{6}$ A/m
Equilibrium Separation Distance	$\tilde{x}_j - \tilde{x}_{j-1}$	.05 m
Viscous Damping	c	.02 Ns/m

a desired level of disorder. Magnets were aligned such that all magnets repelled each adjacent neighbor. Additionally, a final magnet (identical to the first magnet) was added such that there was always an odd number of magnets on the rail. If the unit cell was repeated n times, the total number of magnets in the system was $2n + 1$.

The first and last magnets on each end of the system were fixed in place, with a constant relative position on the rail. All other magnets were free to move in the axial direction. Rotation of the magnets was not considered. Base excitation was then applied to the rail with a prescribed amplitude and frequency in the axial direction, causing prescribed translational motion of the two fixed magnets. It was assumed that there was no frictional force between the free moving magnets and the rail in the application of this exterior force, however linear viscous damping was later considered in numerical simulations of the system.

2.3 Mathematical Model

Since the oscillators are assumed to be aligned in the horizontal plane, the only forces on the system in the direction of motion are from magnetic interactions and damping. Placing the origin at the center of the left most magnet at time $t = 0$, the position of the j^{th} magnet at time t is described by $x_j(t)$.

Since all magnets are aligned to repel their neighbors, by convention, the dipole

moment of the first magnet in each unit cell will be

$$\mathbf{m}_{odd} = (MV)\hat{\mathbf{I}} \tag{2.1}$$

and $\mathbf{m}_{even} = -\mathbf{m}_{odd}$, where M is the magnetization, V is the volume of the each magnet, $\hat{\mathbf{I}}$ is the axial unit vector and all magnets are assumed to be of identical size and strength. The relative position of magnet i with respect to magnet j is then

$$\mathbf{r}_{ij} = (x_i - x_j)\hat{\mathbf{I}}. \tag{2.2}$$

The generic three-dimensional attractive or repulsive force [60] on magnet i due to magnet j is then

$$\mathbf{F}_{ij} = -\frac{\mu_0}{4\pi}\nabla\left(\frac{\mathbf{m}_i \cdot \mathbf{m}_j}{r_{ij}^3} - 3\frac{(\mathbf{m}_i \cdot \mathbf{r}_{ij})(\mathbf{m}_j \cdot \mathbf{r}_{ij})}{r_{ij}^5}\right) \tag{2.3}$$

where r_{ij} is the magnitude of $\mathbf{r}_{ij}$. When motion and magnet orientation are restricted to one dimension, summing Eq. 2.3 for the interactions with neighboring magnets results in

$$\mathbf{F}_j = \frac{3\mu_0}{2\pi}\left(\frac{\mathbf{m}_j \cdot \mathbf{m}_{j+1}}{(x_j - x_{j+1})^4} - \frac{\mathbf{m}_j \cdot \mathbf{m}_{j-1}}{(x_j - x_{j-1})^4}\right). \tag{2.4}$$

2.3.1 Equation of Motion

Using Newton's Second Law, the generalized coordinates will be x_j for $j = 2, 3...n-1$, the magnets that are free to move along the rail. When m_j is the mass for the j^{th} magnet, and its associated acceleration is $\ddot{x}_j$, the $n-1$ equations of motion for the central magnets are then of the form

$$m_j\ddot{x}_j = F_j. \tag{2.5}$$

After substituting the results of Eqs. 2.1 and 2.4, and adding linear damping, the final form is

$$m_j\ddot{x}_j + c\dot{x}_j - \frac{3\mu_0 M^2 V^2}{2\pi}\left(\frac{1}{(x_j - x_{j-1})^4} - \frac{1}{(x_j - x_{j+1})^4}\right) = 0. \tag{2.6}$$

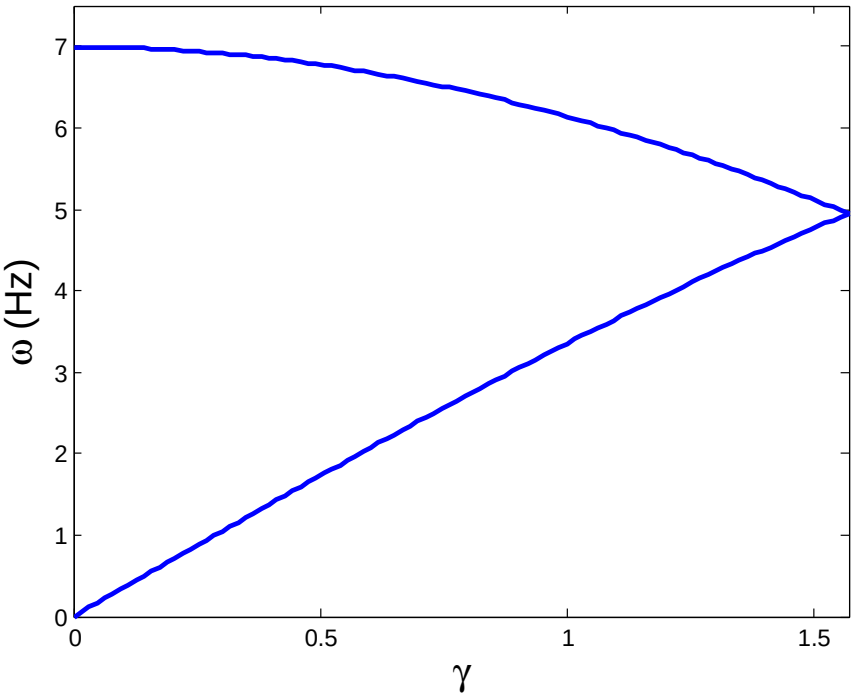

FIGURE 2.2: The frequency band structure shows the plotted solutions to Eq. 2.14 for the case when m_1=.04 kg, m_2=.02 kg and shows that there is a propagation constant for all frequencies < 7 Hz

2.4 Perturbations About the Nonlinear Equilibrium

To analyze the expected response of this system, an infinitely long chain will be modeled by wrapping a single unit cell upon itself as a circulant matrix. In the case where M and V are the same for all oscillators, the equilibrium position is trivially calculated through placing all magnets equidistant from both of its neighbors. The system is then linearized about this equilibrium position and evaluated after introducing a small perturbation. The solution is then assumed to be in the form of a traveling wave. Finally, the system of equations can be rewritten in the form of a standard eigenvalue problem that can be solved for the frequency and amplitude of oscillations. Section 2.6 will analyze these assumptions at increased excitation levels to assess their suitability for realistic nonlinear systems.

The first step in the analysis of this infinite chain will be linearization about the

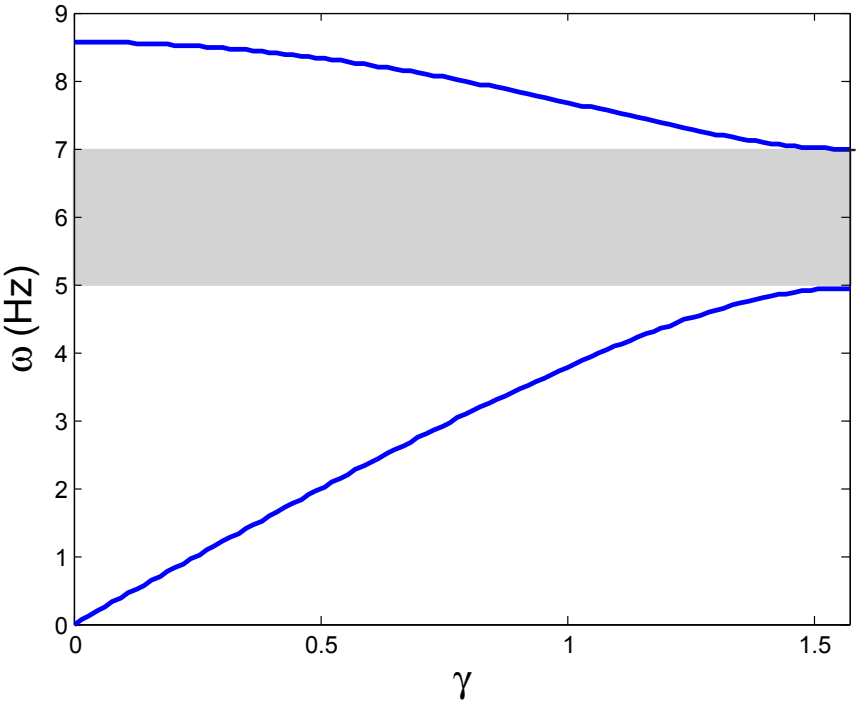

FIGURE 2.3: The frequency band structure shows the plotted solutions to Eq. 2.14 for the case when m_1=.04 kg, m_2=.02 kg. The shaded region illustrates the attenuation zone between frequencies $5-7$ Hz where Eq. 2.14 has no propagation constant solutions.

stable system equilibrium, $\tilde{x}$. The Taylor series expansion of Eq. 2.4 for a small perturbation from equilibrium results in

$$\begin{aligned} F \quad & (\tilde{x}_{j-1}+\xi_{j-1}, \tilde{x}_j+\xi_j, \tilde{x}_{j+1}+\xi_{j+1}) \\ = \quad & F(\tilde{x}_{j-1}, \tilde{x}_j, \tilde{x}_{j+1}) + \xi_{j-1}C_2 + \xi_j C_3 + \xi_{j+1}C_4 + H.O.T. \end{aligned} \tag{2.7}$$

where $F(\tilde{x}_{j-1}, \tilde{x}_j, \tilde{x}_{j+1}) = 0$ by definition and the constants have the following values

$$C_2(j) = \frac{6\mu_0}{\pi(\tilde{x}_j - \tilde{x}_{j-1})^5} \tag{2.8}$$

$$C_3(j) = \frac{-6\mu_0}{\pi(\tilde{x}_{j+1} - \tilde{x}_j)^5} + \frac{6\mu_0}{\pi(\tilde{x}_{j-1} - \tilde{x}_j)^5} \tag{2.9}$$

$$C_4(j) = \frac{-6\mu_0}{\pi(\tilde{x}_j - \tilde{x}_{j+1})^5} \tag{2.10}$$

In a propagation zone, the system solution will take the form of a traveling wave

[19],

$$\xi_j = A_j e^{i(j\gamma - \omega t)} \tag{2.11}$$

where A_j is the amplitude of vibration of the j^{th} magnet, ω is the frequency of base excitation, and γ is the wave number. Noting that $\ddot{x}_j = \ddot{\xi}_j$, the acceleration of each magnet can be represented by

$$\ddot{x}_j = -\omega^2 \xi_j. \tag{2.12}$$

After substituting Eqs. 2.7-2.12 into Eq. 2.6, assuming that damping is negligible, dividing by $e^{i(j\gamma - \omega t)}$ and rearranging, Eq. 2.6 becomes

$$\frac{M^2V^2}{m}\left(-\frac{C_2}{m_j}A_{j-1}e^{-i\gamma} - \frac{C_3}{m_j}A_j - \frac{C_4}{m_j}A_{j+1}e^{i\gamma}\right) - \omega^2 A_j = 0, \tag{2.13}$$

where m represents the mass of the first oscillator and m_j is now a nondimensional scaling factor so that $m_j m$ now equals the mass of the j^{th} oscillator in kg. This equation can be rewritten as a standard eigenvalue problem of the form

$$(\mathbf{S}(\gamma) - W(\omega)\mathbf{I})\mathbf{A} = 0 \tag{2.14}$$

where $\mathbf{I}$ is the identity matrix,

$$\mathbf{S} = \begin{bmatrix} -\frac{C_3}{m_1} & -\frac{C_2}{m_1}e^{-i\gamma} - \frac{C_4}{m_1}e^{i\gamma} \\ -\frac{C_2}{m_2}e^{-i\gamma} - \frac{C_4}{m_2}e^{i\gamma} & -\frac{C_3}{m_2} \end{bmatrix}, \tag{2.15}$$

and

$$W = \frac{m\omega^2}{M^2V^2} \tag{2.16}$$

for the circulant unit cell with 2 elements.

Solving for the frequency, ω, across the irreducible Brillouin zone (γ ranging from 0 to $\pi/2$) [17] when the two magnets have the same mass, Fig. 2.2 shows that Eq. 2.14 has a solution across the entire usable frequency band with no gaps. However, as seen in Fig. 2.3, once the mass ratio is changed, a band gap becomes clearly visible.

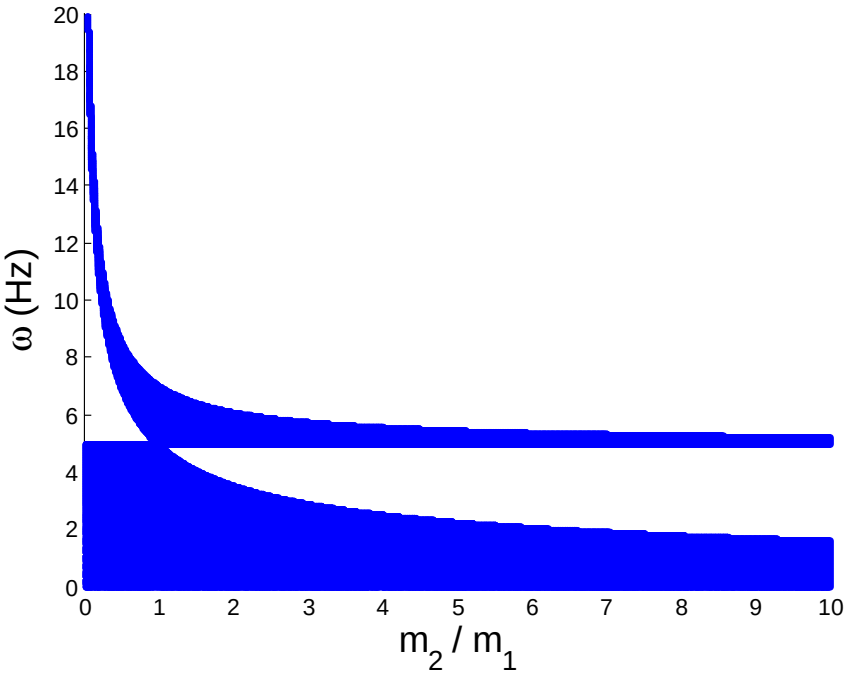

FIGURE 2.4: The frequency band structure shows the plotted solutions to Eq. 2.14 for different mass ratios by holding m_1=.04 kg constant and varying m_2. Blue regions represent propagation zones and white space corresponds to attenuation zones.

In this case, between $5 - 7$ Hz, there is no solution to the eigenvalue problem of Eq. 2.14, and therefore waves cannot propagate in this region. This frequency region is referred to as an attenuation zone.

The size and location of a band gap can be partially controlled through the initial system construction by choosing appropriate sizes for each mass. Figure 2.4 shows the changing locations and size of band gaps for ratios up to $m_2/m_1 = 10$ while holding $m_1 = .04$ kg constant. Specifically, the size of the band gap grows as the difference between the masses gets larger. Whether the band gap occurs above or below the critical frequency (5 Hz in Fig. 2.4) is determined by whether the varied mass (m_2 in this case) becomes larger or smaller than the reference constant mass (m_1). If the varied mass is smaller (larger) than the reference mass, the band gap will occur above (below) the critical frequency. It should be noted that m_1 and m_2 are completely interchangeable and either can be used as reference or varied. As can be

seen in the matrix of Eq. 2.15, if m_1 and m_2 are reversed, S will still have the same characteristic equation and the same system behavior will be observed. Thus, a large m_1 with a small m_2 will show the same system behavior as a small m_1 and large m_2. The same results of the previous example could have alternatively been attained by holding $m_2 = .02$ kg constant, causing a 7 Hz critical frequency. Then setting the varied $m_1 = .04$ kg would result in a band gap below the critical frequency since the varied mass would be larger than the reference mass, which would again result in the same band gap between 5-7 Hz.

2.5 Uncertainty Analysis

Given that $\omega = f(m, M, V)$ from Eq. 2.16, the absolute uncertainty in frequency $\Delta\omega$ can be solved using the absolute uncertainty in magnetization ΔM, mass Δm, volume ΔV, and

$$\Delta\omega^2 = \left(\frac{\partial\omega}{\partial M}\right)^2 \Delta M^2 + \left(\frac{\partial\omega}{\partial Y}\right)^2 \Delta Y^2, \tag{2.17}$$

where $Y = V^2/m$ has been temporarily substituted since V and m are assumed to be perfectly correlated, and M and Y are completely uncorrelated [61]. Solving Eq. 2.17 and substituting for Y results in the final equation for the uncertainty of frequency as a function of the uncertainty in magnetization and mass,

$$\Delta\omega = \sqrt{\frac{WV^2}{m}\Delta M^2 + \frac{WM^2m^2}{4V^2}\Delta m^2}. \tag{2.18}$$

The uncertainty in frequency can be graphically shown for variation in each parameter individually or in conjunction. In the first example, it is assumed that the mass and volume of each oscillator and the overall system length are constant and can be accurately measured to a desired level of accuracy. This then leaves only the magnetization level as an uncertain parameter. The provided manufacturer specifi-

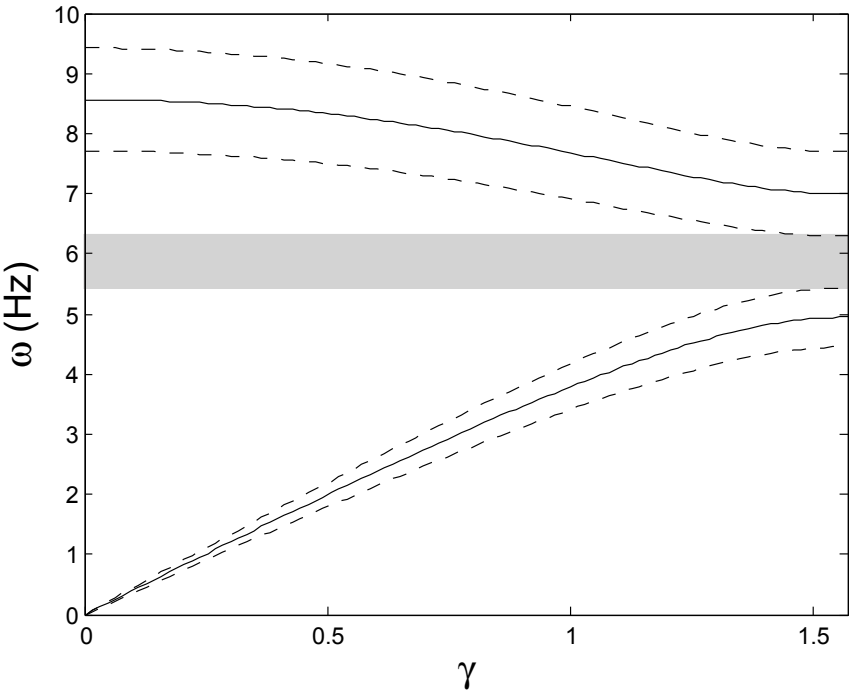

FIGURE 2.5: The frequency band structure shows the plotted solutions to Eq. 2.14 for the case when m_1=.04 kg, m_2=.02 kg. Dotted lines represent uncertainty boundaries corresponding to $+/-10\%$ of M, which significantly reduce the size of the shaded attenuation zone.

cations for the magnets used in this system included tolerances between .75-1.5% for residual flux density. It has been assumed for this example that these errors occur as a systemic bias affecting all oscillators produced in a particular batch equally as opposed to independent randomness in the parameters of each oscillator (in which case, this technique would not be applicable). To account for this and other potential sources of environmental error such as temperature fluctuation, this factor has been artificially inflated in Fig. 2.5 which shows the frequency band structure for a system where M is only known to within $+/-10\%$ of its given value. This plot shows that the original band gap between $5-7$ Hz for the case where M is known exactly has been reduced to $5.4-6.3$ Hz after uncertainty is introduced. In this example, 10% uncertainty in a variable affecting the coupling strength between adjacent oscillators has resulted in a 55% reduction in the band gap range.

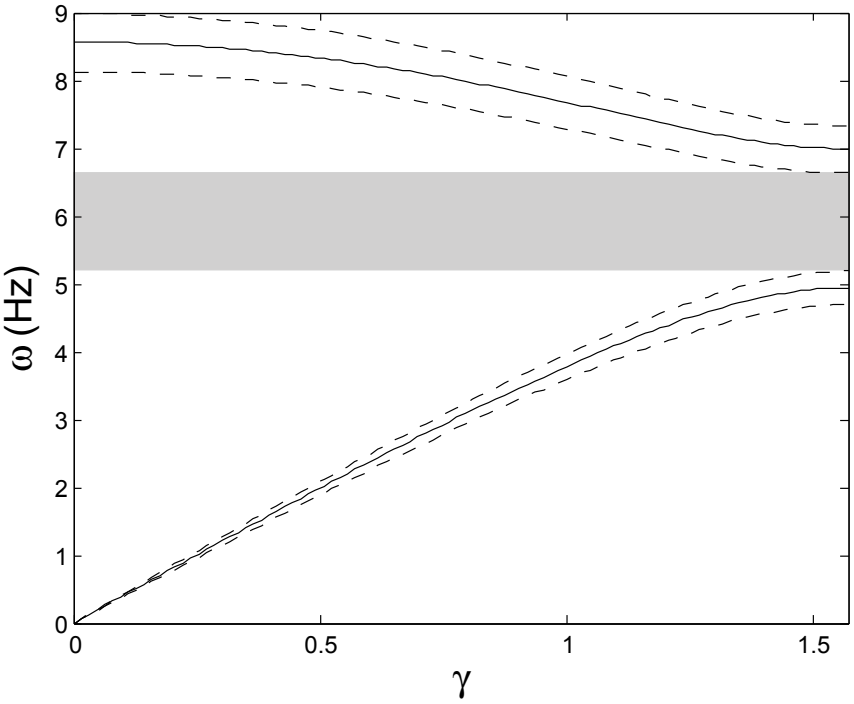

FIGURE 2.6: The frequency band structure shows the plotted solutions to Eq. 2.14 for the case when m_1=.04 kg, m_2=.02 kg. Dotted lines represent uncertainty boundaries corresponding to $+/-10\%$ of m and V, which slightly reduce the size of the shaded attenuation zone.

Instead of a confidence level type of uncertainty, some systems are better characterized by degradation uncertainty, in which a parameter's initial value can be accurately assessed, but this value will uniformly change over time for all oscillators due to environmental factors. An example of this would be the change in magnetization of a ferromagnetic material with changes in temperature [62]. Figure 2.7 shows an example where the initial magnetization level is precisely known, but is subject to deterioration. From the initial $5-7$ Hz band gap, as the magnetization level decreases and the coupling strength between each oscillator lowers, the band gap frequencies also decrease. By the time 30% degradation has occurred, the band gap region has dropped to $3.4-4.9$ Hz and no longer overlaps the original attenuation zone.

An interesting feature of magnetization in this system is that since it is of the

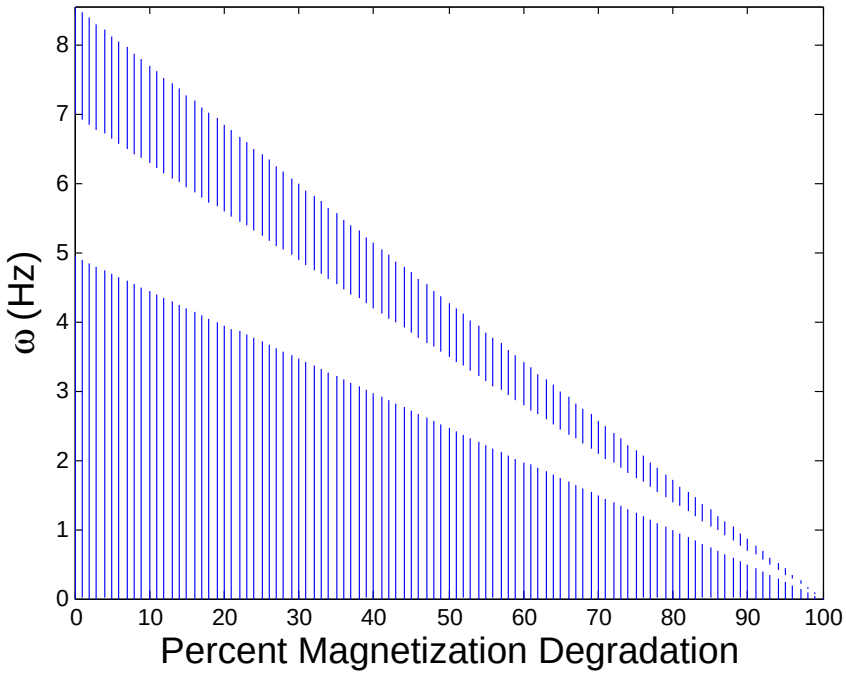

FIGURE 2.7: Propagation zones for the case when m_1=.04 kg, m_2=.02 kg as magnetization (M) suffers degradation

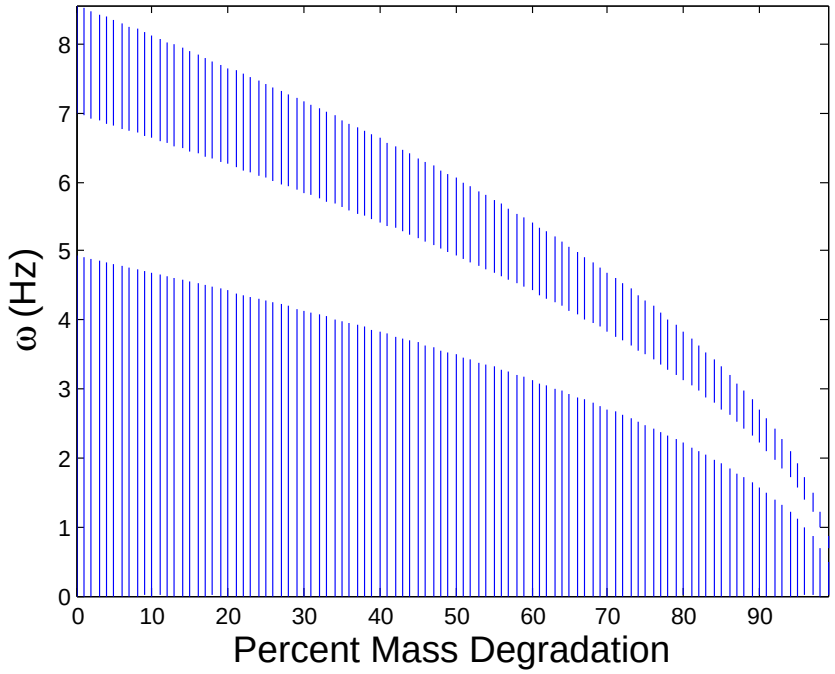

FIGURE 2.8: Propagation zones for the case when m_1=.04 kg, m_2=.02 kg as mass and volume suffer degradation

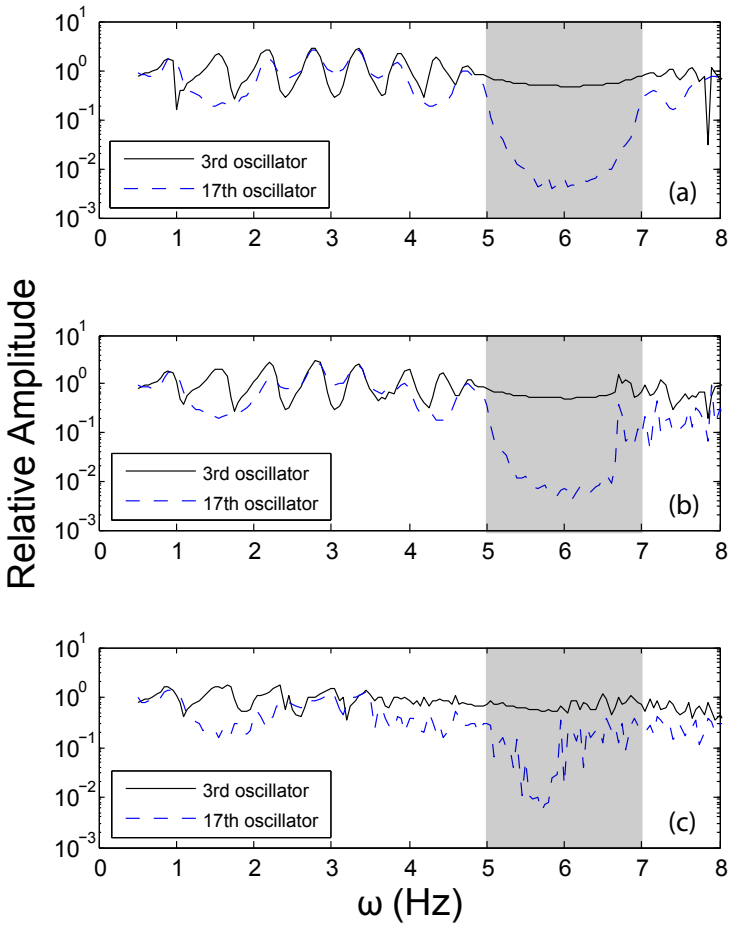

FIGURE 2.9: Numerically simulated frequency response (relative to the displacement amplitude of the driven oscillator) of 2 oscillators in a 20 unit cell chain using the constants from Table 4.2 for the case when m_1=.04 kg, m_2=.02 kg and base excitation is (a) A = .0005 m, (b) A = .003 m, (c) A = .01 m.

same order as ω in Eq. 2.16, frequency changes linearly with adjustments to magnetization. Figure 2.7 illustrates this linear affect since it can be clearly seen that as magnetization is reduced, minimum and maximum frequencies that define the propagation zones decrease correspondingly. Similarly in Fig. 2.5, each dotted line representing the confidence intervals is exactly 10% above and below its corresponding base value.

Assuming that density is held constant, mass and volume will change identically. Since Eq. 2.16 has V^2 in the numerator and m in the denominator, that leaves V

proportional to ω^2 (contrasted with previously M^2 proportional to ω^2). Figures 2.6-2.8 show that the system is much more robust in accommodating uncertainty in mass and volume. With 10% uncertainty in the mass of each oscillator, the known band gap region still covers $5.2 - 6.6$ Hz. Though this correlates to a 30% reduction from the original gap size without uncertainty, it is 50% larger than the gap size with the same level of uncertainty in the magnetization. In the case of mass degradation over time, it is not until 50% degradation is reached that the band gap range ceases to overlap the original region. As proposed in Ref. [63], different behavior is observed when the uncertainty is contained in a parameter of a different order from frequency, confirming that greater design emphasis and stricter tolerances need to be enacted over certain parameters, in this case, magnetization.

2.6 Nonlinearity

In order to assess the applicability of the assumed traveling wave solution form, simulations were run on a chain comprising 20 unit cells using the constants of Table 4.2 with increasing base excitation. The first and last magnets were given prescribed motion of the form $x_1 = x_{2n+1} = A\cos(\omega t)$ and motion of the central magnets was computed by numerically integrating Eq. 2.6 using the Matlab function ODE45, a 4th order Runge-Kutta based algorithm. Figures 2.9-2.10 do not represent a frequency sweep, but rather are a compilation of separate single frequency simulations, each of which was run for 200 periods of excitation to ensure steady state was reached. The amplitudes in Fig. 2.9 were found by nonlinear regression using the Matlab function NLINFIT.

In the case where the masses of each magnet in a unit cell were not identical, band gaps were observed. Figure 2.9(a) shows 3 distinct regions of behavior. In the first and last regions (< 5 Hz, > 7 Hz respectively), the system behaves almost identically to the case in which the masses of each oscillator are the same. That is, each magnet

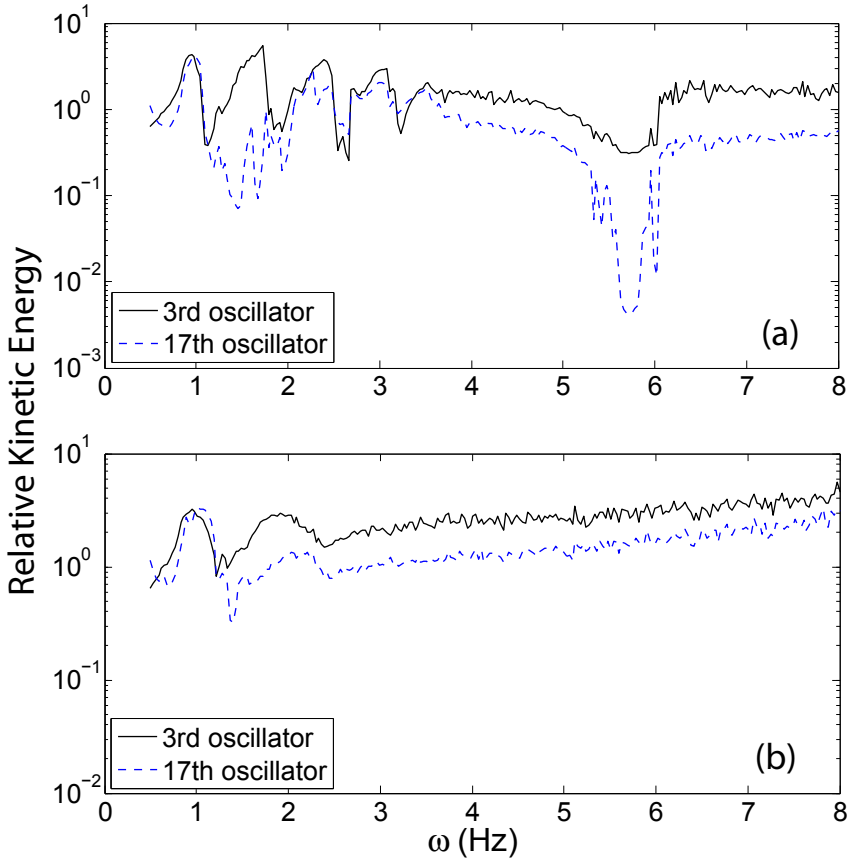

FIGURE 2.10: Numerically simulated relative asymptotic kinetic energy of 2 oscillators in a 20 unit cell chain using the constants from Table 4.2 for the case when m_1=.04 kg, m_2=.02 kg and base excitation is (a) A = .01 m, (b) A = .025 m.

drifts in and out of phase with the base excitation and has a correspondingly lower or higher amplitude. Between $5-7$ Hz, the system shows a band gap region. In this attenuation zone, it can be seen that amplitudes along the chain have decreased by several orders of magnitude.

Ref. [64] demonstrated that changing the excitation amplitude in a nonlinear chain can affect a band gap location. That work is supported by Figures 2.9(b) and 2.9(c) that show the effect of increasing the base excitation amplitude. Once the assumed small perturbations are exceeded, the predicted band gap region begins to be noticeably affected with base excitation amplitude of 6% of the static equilibrium separation. However, even with moderate excitation at 20% of the initial separation

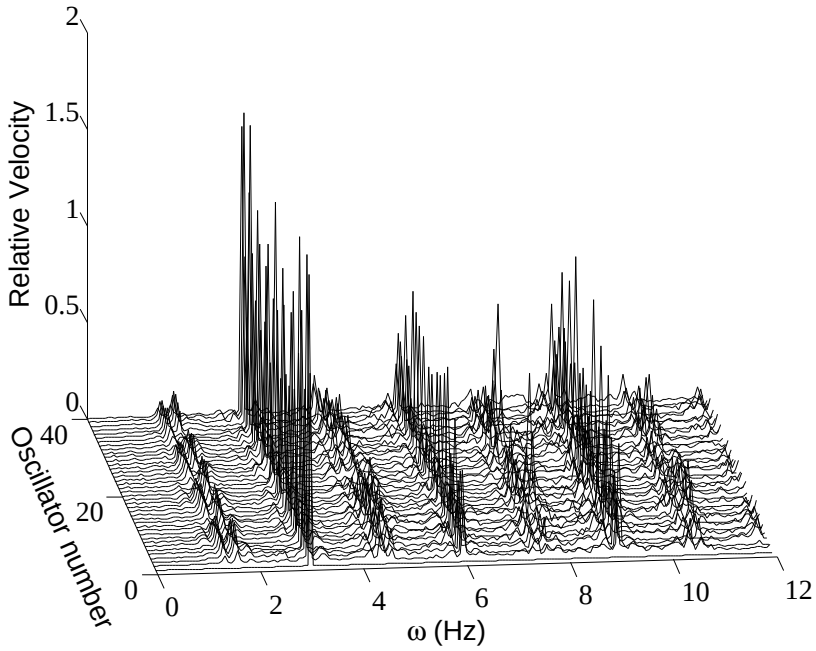

FIGURE 2.11: Response of each oscillator of a 20 unit cell chain under base excitation of $A = .01$ m at $\omega = 3$ Hz (propagation zone)

distances, although the nonlinear effects are clearly visible in Fig. 2.9(c), a band gap is still evident with a similar level of attenuation as the low amplitude cases, albeit over a narrower frequency range. Ref. [18] provides a simple proof of the non-existence of a propagation constant for nonlinear systems, explaining deviation of these systems from the linear predicted responses.

Beyond moderate excitation amplitudes, the response of each oscillator no longer resembled a simple sine wave and was much more chaotic, so NLINFIT solutions were no longer accurate. To more thoroughly account for this nonlinear behavior, Fig. 2.10 instead shows the relative kinetic energy in reference to the excited magnets, computed as the time average kinetic energy of each oscillator over a large number of periods once steady state had been reached. It can be seen in Fig. 2.10(b) that the band gap has effectively disappeared once amplitude has reached $A = .025$ m, corresponding to half the static equilibrium separation distance. This provides some level of insight into the implementation limitations for this particular nonlinear system.

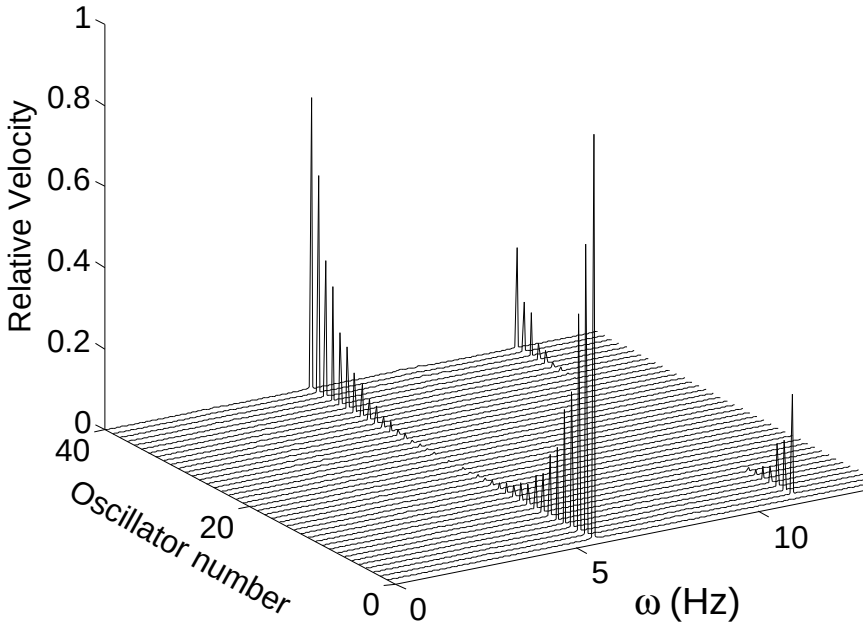

FIGURE 2.12: Response of each oscillator in a 20 unit cell chain under base excitation of $A = .01$ m at $\omega = 5.66$ Hz (attenuation zone)

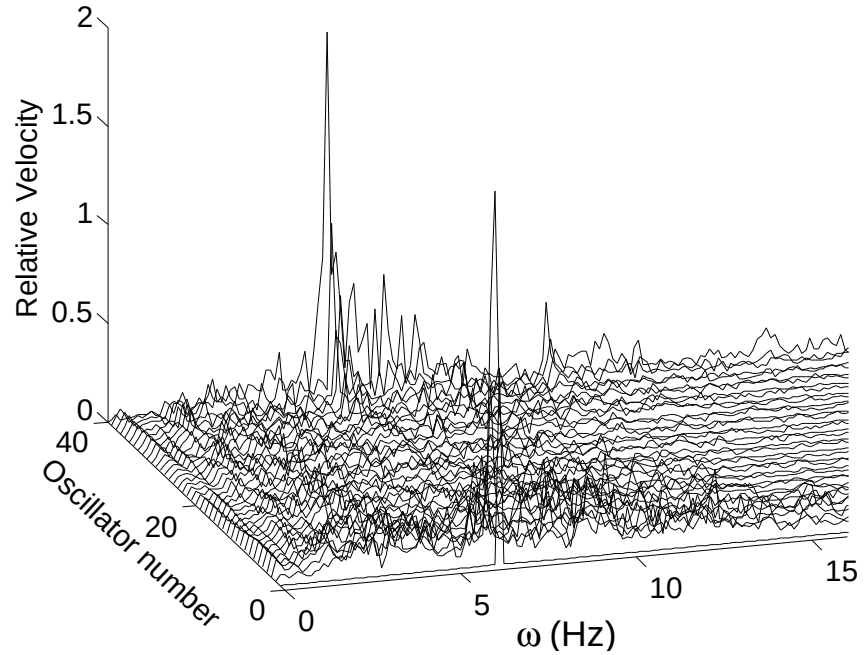

FIGURE 2.13: Response of each oscillator in a 20 unit cell chain under base excitation of $A = .01$ m at $\omega = 6.25$ Hz (analytically predicted propagation zone, numerically predicted attenuation zone)

The influence of nonlinearity is apparent in both the propagation of oscillations throughout the array and the distribution of energy through harmonics of the excitation frequency. For low amplitude excitation, the system is in the linear regime and oscillations occur as predicted by standard methods with each oscillator's energy entirely located at the excitation frequency. As the excitation level is increased however, the nonlinear nature of the oscillator interactions become apparent, as shown by the Fast Fourier Transforms in Figs. 2.11-2.13. Using the same example system comprised of 20 unit cells, Fig. 2.11 shows the frequency content relative to the driven oscillator for excitation amplitude and frequency at 0.01 m and 3 Hz, respectively. At this excitation level (20% of the separation distance), the oscillators respond nonlinearly, spreading the energy about harmonics and subharmonics of the excitation frequency.

Figure 2.12, however, shows the continued existence of a narrow band gap. This example used the same excitation amplitude but with a frequency of 5.66 Hz, squarely within the band gap as shown by the narrow valley of Fig. 2.9(c). The nonlinear effects are shown by the presence of a small peak at 11.32 Hz, but otherwise this plot looks exactly like a linear system's behavior inside a band gap. It should be noted that wave propagation in this particular system works from the outsides inward, as opposed to starting at one end of the chain and working forward. This results from the system design that uses capping magnets on each end that are both equally excited and maintain a fixed relative distance between them.

Figure 2.13 then shows the result of increasing the excitation frequency to 6.25 Hz, placing the system inside the analytically predicted band gap region, but outside this narrower simulated band gap region. Amplitudes are not reduced to near zero levels as in the attenuation zone. Instead, the energy is spread across a wide frequency range in motion resembling chaotic noise. These three plots suggest that this type of nonlinear magnetic system could still be used in applications desiring linear band

gap properties, even at amplitudes that would create significant nonlinear behavior at other frequencies.

2.7 Conclusions

This chapter described a method to reorganize the equations of motion of oscillating systems that are analytically solved using the propagation constant technique, to allow the application of standard uncertainty analysis procedures. By separating a function of frequency, magnetization, and mass from the system's equation of motion, a closed form equation for the uncertainty of frequency was found. This would allow a system designer to account for uncertainty in parameter values due to discrete component size availability, variations in environmental conditions, or desired safety factors. The different effects caused by parameters of the same or unequal order as frequency was observed, and it was specifically noted that the system was much more robust to changes in the lower order parameter, mass, and much more susceptible to changes in magnetization which is of the same order as frequency.

The chain of magnetically coupled oscillators modeled in this system provides a base comparison for realizable physical experimental systems. The numerical simulations were performed to provide fundamental understanding of the applicability and limitations of the propagation constant method for this nonlinear system. As predicted in the literature, the analytically derived band gaps appeared to change as amplitude was increased. However, this chapter has supplemented those results by showing that even at moderate levels of excitation, the predicted level of attenuation inside the band gap remained relatively constant, albeit over a narrower frequency range. This chapter also provided illustrations of the type and form of nonlinear behavior observed in amplitude dependent systems by showing that at high levels of excitation amplitude where the small perturbation assumption no longer applied, energy was transmitted through harmonics and subharmonics at low frequencies, but

low energy chaos was observed at higher frequencies.

In a constructed system, the oscillator masses would not normally be adjustable after the system has been deployed. Chapter 3 will describe a theoretical method by which changes in parameters such as the application of an external magnetic field might be passively implemented to manipulate the band gap regions, so that the system could be controlled in a manner to provide switching or filtering capabilities. Chapter 5 then describes the construction of a physical experiment to confirm the affects of this passive control technique.

3

Passive Bandgap Reconfiguration Born from Bifurcation Asymmetry

3.1 Introduction

When asymmetry [12, 13] or imperfections [14, 15] are incorporated into a chain of otherwise identical repeating, periodic cells of oscillators, system frequency behavior is split into propagation zones (pass bands) where wave propagation occurs and attenuation zones (bandgaps) where oscillator amplitudes tend towards zero and no propagation exists. Exploitation of these frequency regions has allowed advances in materials science, optics, acoustics and vibrations.

Much of the current research in energy absorption can be traced back to the study of elementary granular collisions of simple one dimensional waves analytically [2, 8, 9] and numerically [7]. Though these systems are often modeled linearly, the beneficial and detrimental properties of many nonlinear behaviors have also been explored [18, 19, 54–57, 64, 65]. Several recent studies have also considered wave propagation in high amplitude, multi-stable systems [66] and have noted bifurcation based switching [67] for rectification [68, 69].

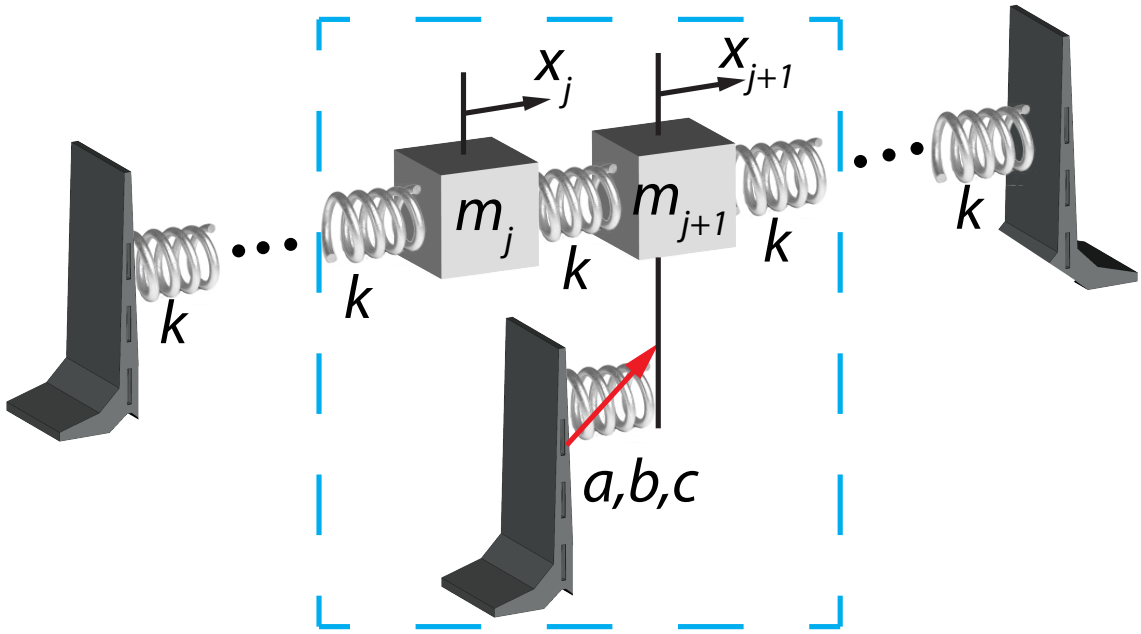

FIGURE 3.1: (Generalized block diagram showing both coupled and uncoupled forces. The dashed box shows the repeating unit cell, and the total chain is capped by rigid boundaries at each end.

The development of reconfigurable bandgap waveguide devices is a field of active research in photonics and phononics. Previous advances have focused on reconfiguration that require manual operation of a switch [5, 70, 71], active tuning through component replacement to change size, mass, or material properties [23, 25, 72, 73], or varying design parameters such as precompression [27, 74] to change the system's characteristics. However, those devices would not be appropriate for remote or autonomous settings which require automatic or passive switching of single-frequency propagation attributes to time-varying environmental stimuli. This study demonstrates how a nonlinear restoring force can create a multi-stable system, designed for passive, bifurcation induced filtering, with distinct narrowband wave propagation behavior in each potential well. Using uniform periodic structures, this passive technique provides results complementary to active tuning for the realization of differing wave propagation behaviors.

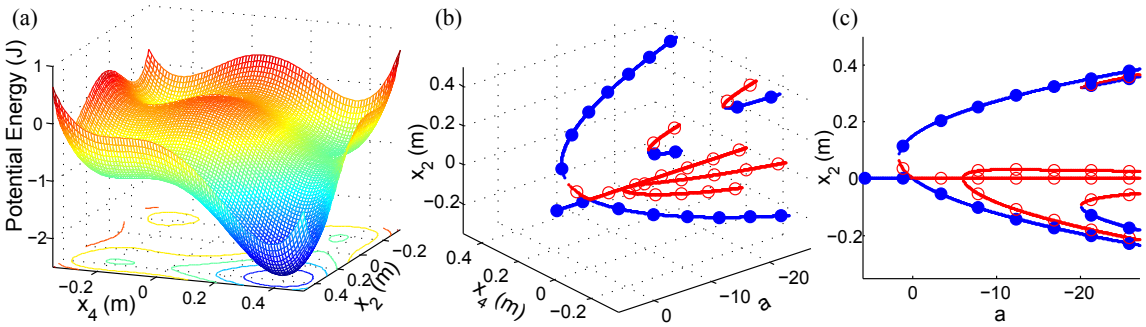

FIGURE 3.2: Properties of a two unit cell chain with restoring force coefficients $b = -45$ N/m^2, and $c = 300$ N/m^3. (a) Potential energy as a function of position of the two bistable oscillators, with $a = -27$ N/m. (b) Bifurcation diagram shows the varying number of possible stable (solid) and unstable (open) equilibria when varying the coefficient of the linear term in the uncoupled restoring force. (c) 2D projection of the bifurcation diagram for a single oscillator highlights equilibrium asymmetry resulting from $b \neq 0$.

3.2 Mathematical Model

A Duffing-type restoring force is introduced as a specific example of a general bistable system to address these challenges. Fig. 3.1 illustrates a hypothetical chain where the bandgap structures can passively reconfigure during transitions through a bifurcation in the system's response. There are two masses per unit cell, linear interconnections

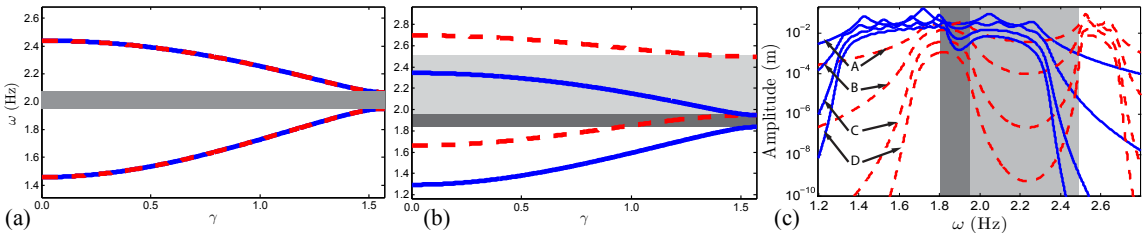

FIGURE 3.3: Wave propagation characteristics. (a) Frequency band structure in the bistable infinite periodic lattice shows a single bandgap in the symmetric case ($b = 0$). (b) An asymmetric case ($b \neq 0$) shows distinct bandgap regions in the negative (solid) and positive (dashed) potential wells. (c) Linearized frequency response of the last oscillator in an $N = 2$ (A), 5 (B), 10 (C), and 15 (D) chain mirrors expected behavior from the infinite case. The parameters used to create these results were $m_1 = 0.04$ kg, $m_2 = 4m_1$, $d = 0.02$ Ns/m, $k = 3$ N/m, $a = -10.5$ N/m, $b = -45$ N/m^2, and $c = 300$ N/m^3.

(assumed for simplicity), and a nonlinear restoring force on alternating oscillators. Mathematically, this system is described by

$$m_j\ddot{x}_j + d\,\dot{x}_j + k\,(2x_j - x_{j+1} - x_{j-1}) = 0 \tag{3.1a}$$

$$m_j\ddot{x}_j + d\,\dot{x}_j + k\,(2x_j - x_{j+1} - x_{j-1}) + ax_j + bx_j^2 + cx_j^3 = 0\,, \tag{3.1b}$$

where x_j is the relative position of the j^{th} oscillator, the constants a–c describe the uncoupled restoring force, Eq. 3.1a is applicable $\forall\, j = (1, 3, 5, \dots)$ and Eq. 3.1b is applicable $\forall\, j = (2, 4, 6, \dots)$.

A method to solve linear bandgap problems was derived in Ref. [17] that assumed a solution in the form of a traveling wave. The model reduced to a standard eigenvalue problem where an infinite chain was modeled as a single unit cell wrapped upon itself as a circulant matrix. Displacements for the j^{th} oscillator were written as small oscillations $\xi_j(t)$ about the equilibrium position $\tilde{x}_j$, or $x_j = \tilde{x}_j + \xi_j(t)$. Rewriting the oscillations in the form of a traveling wave provides

$$\xi_j = A_j e^{i(j\gamma - \omega t)}, \tag{3.2}$$

where A_j is the oscillation amplitude of the j^{th} mass, ω is the frequency of the base excitation, and γ is the wave number. From Eq. 3.2 we find $\ddot{\xi}_j = -\omega^2\xi_j$ and then insert this relationship, along with Eq. 3.2, into Eqs. 3.1a and 3.1b. The final form for the eigenvalue problem becomes

$$\left(\mathbf{K}(\gamma) - \omega^2\mathbf{M}\right)\mathbf{A} = \mathbf{0}\,, \tag{3.3}$$

where the matrices that appear in Eq. 5.10 are

$$\mathbf{M} = \begin{bmatrix} m_1 & 0 \\ 0 & m_2 \end{bmatrix} \text{ and } \mathbf{K} = \begin{bmatrix} 2k & -2k\cos\gamma \\ -2k\cos\gamma & \sigma \end{bmatrix}, \tag{3.4}$$

where $\sigma = 2k + a + 2\,b\,\tilde{x}_j + 3\,c\,\tilde{x}_j^2$ and $2\cos\gamma$ was substituted for $e^{-i\gamma} + e^{i\gamma}$.

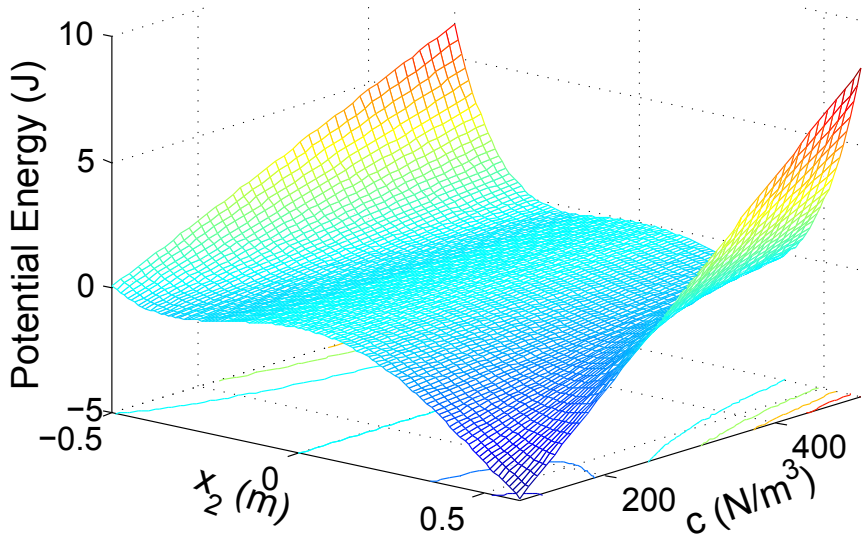

FIGURE 3.4: Potential energy of a cubic bistable oscillator with $a = -10.5$ N/m, and $b = -45$ N/m^2 for varying values of c. Increasing this coefficient of the cubic forcing term brings the stable equilibria closer to zero, thereby making the potential wells shallower and reducing the threshold to well escape.

3.3 Parameter Selection

The uncoupled restoring force gives rise to multiple equilibrium positions $\tilde{x}_j$, possible asymmetries in the neighboring wells, and can be used to set a bifurcation threshold for a well escape phenomena. These three behaviors can be tuned using the coefficients a, b, and c respectively.

In general, a chain with N bistable oscillators can have up to 2^N stable equilibria. Long chains can potentially have a large number of hybrid system equilibriums allowing stable solutions where bistable oscillators are in opposite wells, as shown in Fig. 3.2(a) for a two unit cell chain with four possible stable equilibriums. This study will instead focus on an example case with only two stable equilibriums resulting from $a = -10.5$ N/m (see Figs. 3.2(b)-3.2(c) where all $\tilde{x}_j$ are equal (that is, all bistable oscillators are in the same potential well), one where $\tilde{x}_j < 0$ (negative well) and the other $\tilde{x}_j > 0$ (positive well). By selecting a value of coefficient a that limits the number of stable equilibria to two, well escape analysis is simplified since there

is only one alternative potential well that can result from escape.

To explain the unique behaviors of this system resulting from an asymmetric restoring force, first consider the case of a symmetric potential, which requires $b = 0$ in Eq. 3.1b. After solving the nonlinear algebraic equations to find the system equilibria and expanding for small oscillations about these equilibria, Fig. 3.3(a) shows the resulting frequency band structure, which yielded identical behavior in both potential wells. While bandgaps did occur, they were identical for oscillations about either stable equilibrium, as would be expected owing to symmetry.

To contrast this result, consider the asymmetric case when $b \neq 0$; the frequency band structure of Fig. 3.3(b) shows the bandgap regions for an example case when the adjacent wells are imbalanced. Specifically, it can be seen in Fig. 3.3(b) that each bandgap region is coincident with a propagation zone of the other well. This differing bandgap structure is an important feature because a transition from one equilibrium to another will shift the bandpass and filtered (or bandgap) regions by an amount proportional to the parameter b. With increasing absolute value of b, in addition to shifting the location of each bandgap, the propagation and attenuation zones will become increasingly unbalanced from one well to the other, with the shallower well having wider pass bands and a narrower bandgap, and the deeper well having narrow pass bands and a wider bandgap.

The asymmetric potential wells can be further refined through tuning of the cubic coefficient c. Figure 3.4 illustrates the primary effects of increasing the cubic forcing term, which brings the stable equilibria closer to zero and decreases the depth of each potential well. This coefficient should be set based on material properties and expected environmental input to control the threshold to well escape.

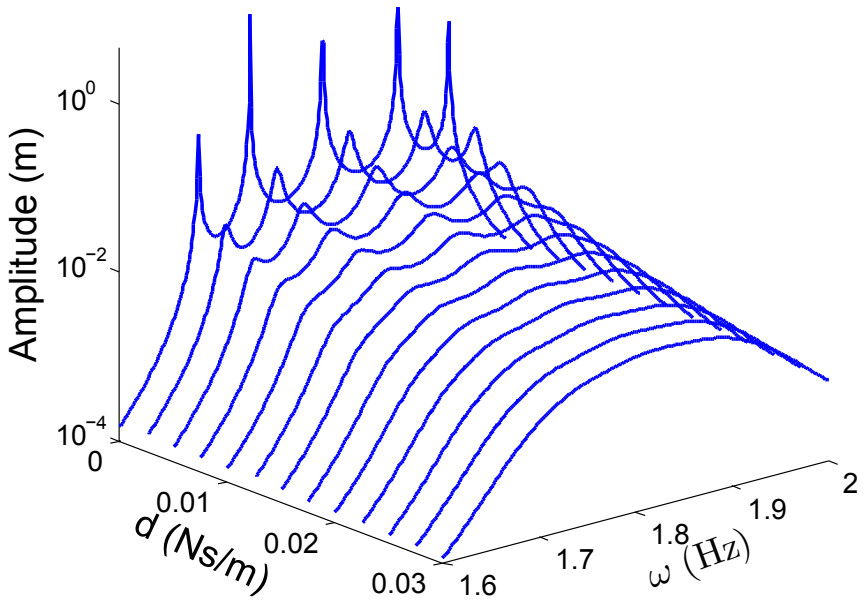

FIGURE 3.5: Visualization of propagation zone behavior with increased damping shows reduced localized peaks, decreased plateau amplitude, and decreased frequency width of the pass band. This example uses the same physical parameters as Fig 3.3(c) and shows the acoustic propagation zone for the N=5 unit cell chain in the positive potential well.

3.4 Linearized System Response

Since the results of the bandgap predictions shown previously were for an infinite chain, this section derives an approximate analytical solution for the frequency response of a finite number of oscillators. More specifically, an approximate expression for the small periodic motions about the stable equilibria is viewed as a complementary tool that will enable a systematic investigation of how finite dimensions alter the bandgap regions and frequency response.

For a damped finite chain with forcing of the form

$$F_1 = \Gamma \cos(\omega t), \tag{3.5}$$

Eqs. 3.1a and 3.1b can be rewritten as

$$m_1\ddot{\xi}_1 + d\dot{\xi}_1 + k\left(2\xi_1 - \xi_2\right) = F_1, \tag{3.6a}$$

$$m_j\ddot{\xi}_j + d\dot{\xi}_j + (2k + a + 2b\tilde{x}_j + 3c\tilde{x}_j^2)\xi_j - k\left(\xi_{j+1} + \xi_{j-1}\right) + \mathcal{O}(\xi^2) = 0, \tag{3.6b}$$

$$m_j\ddot{\xi}_j + d\dot{\xi}_j + k\left(2\xi_j - \xi_{j+1} - \xi_{j-1}\right) = 0, \tag{3.6c}$$

$$m_n\ddot{\xi}_n + d\dot{\xi}_n + (2k + a + 2b\tilde{x}_n + 3c\tilde{x}_n^2)\xi_n - k\xi_{n-1} + \mathcal{O}(\xi^2) = 0, \tag{3.6d}$$

where ξ_j represents small oscillations about an equilibrium. Since the first and last oscillators will only be coupled on one side and attached via springs to rigid boundaries on the other, as shown in Fig. 3.1. Eqs. 3.6b and 3.6c apply $\forall\, j = (2, 4, 6, \ldots, n-2)$ and $\forall\, j = (3, 5, 7 \ldots, n-1)$ respectively.

Eqs. 3.6 can be rewritten in matrix form as

$$\mathbf{M}\ddot{\vec{\xi}}_j + d\dot{\vec{\xi}}_j + \mathbf{K}\vec{\xi}_j = \mathbf{F} \tag{3.7}$$

where the assumed solution form is

$$\vec{\xi}_j = \mathbf{A}\cos\omega t + \mathbf{B}\sin\omega t. \tag{3.8}$$

After substituting Eq. 3.8 into Eq. 3.7 and performing a harmonic balance, the expressions for the coefficients $\mathbf{A}$ and $\mathbf{B}$ become

$$\mathbf{A} = [\omega^2 d^2(\mathbf{K} - \omega^2\mathbf{M})^{-1} + (\mathbf{K} - \omega^2\mathbf{M})]^{-1}\mathbf{\Gamma} \tag{3.9a}$$

$$\mathbf{B} = \omega d(\mathbf{K} - \omega^2\mathbf{M})^{-1}\mathbf{A}. \tag{3.9b}$$

where $\mathbf{\Gamma}$ is a vector of length n with the forcing amplitude Γ in its first term and zeros elsewhere. Figure 3.3(c) shows the solution of Eqs. 3.9a and 3.9b for the displacement amplitude of the last oscillator in chains of various lengths for small oscillations $\xi_j(t)$ about both the negative and positive equilibrium positions $\tilde{x}_j$. It should be noted that the dominant peaks and valleys in Fig. 3.3(c) correspond to the propagation and attenuation zones predicted in Fig. 3.3(b). It can be clearly seen that a well escape

out of a propagation zone will have the most dramatic affect on system response when excitation frequency is in the middle of a large bandgap of the target well, for example in the lightly shaded region of Fig. 3.3(c) around 2.2 Hz.

Smaller, local peaks and valleys result from the oscillator drifting in or out of phase with the base excitation at each frequency and are partially smoothed through assumed light viscous damping. Each propagation zone will have N resonant peaks, one for each unit cell in the finite length chain. An example of this can be clearly seen in Fig. 3.5 where $N = 5$, and five resonant peaks are most prominent with little or no damping. Another side effect of this damping is a decrease in propagation zone amplitude over longer chains, as shown by the lower plateau heights in Fig. 3.3(c) for chains of increased length.

The influences of damping on a given chain are further illustrated in Fig. 3.5 which plots a single propagation zone using a range of damping coefficient values. The three prominent effects as damping is increased are reduced resonant peak amplitudes, reduced plateau amplitudes and reduced frequency range of the pass band. The localized peaks are drastically reduced after incorporating even a minimal amount of damping. Applications that exploit this energy localization would need to prioritize damping reduction much more than an application primarily interested in general propagation since the amplitude and frequency of the propagation zone are much more robust to increases in damping.

3.5 Numerical studies

Using the same constant and coefficient values of Fig. 3.3, an $N = 20$ unit cell chain was modeled and subjected to slowly increasing base excitation of the form of Eq. 3.5, as seen in Fig. 3.6(b). The results of Figs. 3.6-3.7 illustrate how the bifurcation threshold for an escape phenomenon can be used to transition the system to a new bandgap configuration. More specifically, the numerical results show how

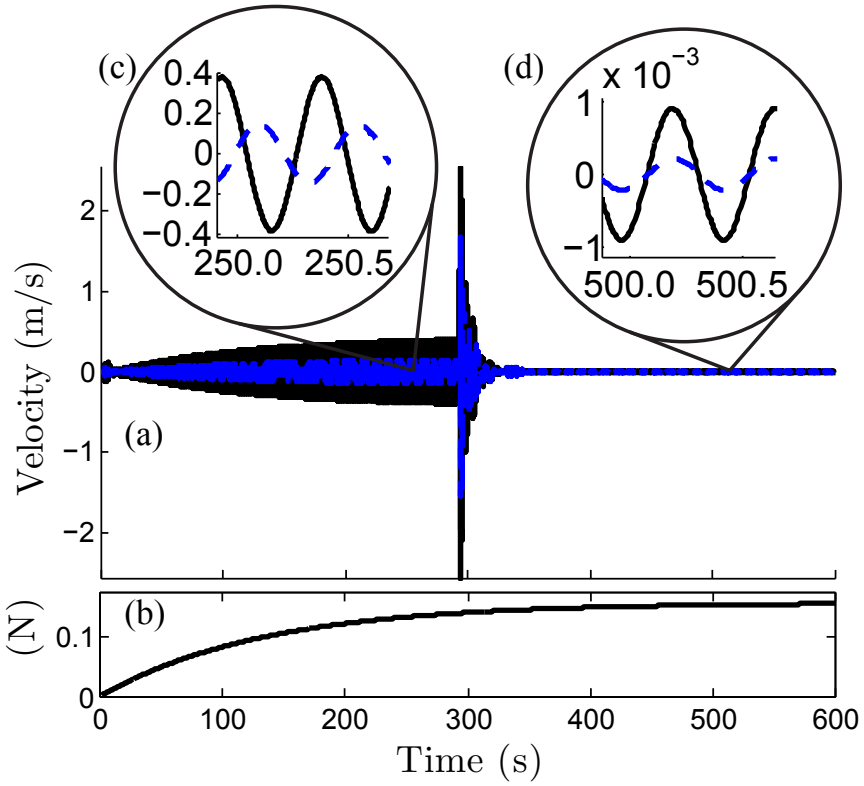

FIGURE 3.6: (a) Velocity profile of a representative unit cell in a 20 cell chain is shown with base excitation $\omega = 2.2$ Hz during a (b) slowly increasing amplitude sweep. (c) Initial wave propagation in the negative potential well which Fig. 3.3(b) shows is a pass band is followed by well escape and (d) velocity reduced by a factor of 100 since the excitation frequency is in the bandgap region of the positive well.

the escape phenomenon transitions the system from the shallower potential well to the deeper well while quenching the oscillation amplitude and velocity by several orders of magnitude.

Since initial positions for the chain are in the negative potential well Fig. 3.7(b), the system is in a propagation zone at the excitation frequency 2.2 Hz. It can be seen in Fig. 3.6(a), that as base excitation increases during a slow amplitude sweep, peak oscillator velocity is similarly increasing. However, once the bifurcation threshold is exceeded, Fig. 3.7(c), the oscillators shift into the deeper, positive potential well. There is a brief period of high velocity movement during the escape, but since 2.2 Hz falls in a bandgap region for the positive equilibrium position, velocities throughout

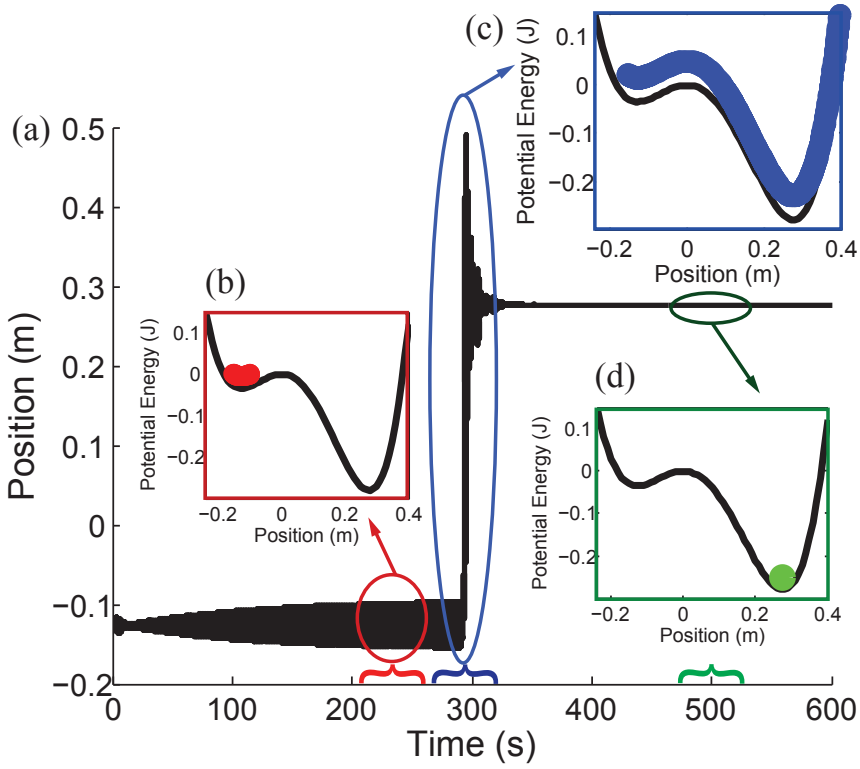

FIGURE 3.7: Transition through the bifurcation region resulting in a filtered response when subjected to 2.2 Hz base excitation. (a) Time series of positions of a representative oscillator during a single frequency, slowly increasing amplitude sweep. (b) Medium amplitude oscillations in the negative potential well at a frequency corresponding to a pass band. (c) High amplitude oscillations during potential well escape. (d) Very low amplitude oscillations occur in the positive potential well where the same input frequency corresponds to a bandgap.

the chain rapidly decrease by several orders of magnitude as shown from Fig. 3.6(c) to Fig. 3.6(d). The filtered behavior is also evident in Fig. 3.7(d), with minimal oscillations, resulting from the same excitation frequency now being in a reconfigured system bandgap.

3.6 Conclusions

This chapter demonstrated a chain of oscillators with passively reconfigurable bandgap regions. This provides an automated alternative to the manually controlled systems in the literature. Implementation of a nonlinear restoring force on alternating os-

cillators resulted in a bistable equilibrium. It was shown that through deliberate selection of particular stiffness components, potential wells could be made asymmetric with each equilibrium having different wave propagation attributes, i.e. bandgap and bandpass regions.

The observed phenomenon is potentially useful to systems which may be subject to shock loads. For example, it would be possible to create a system that would perform a primary well escape when subjected to an unusually large impulse. If equilibrium positions have opposing pass and stop bands, this could passively force a transition from propagation to attenuation zone behavior whenever large vibrations are present, thus protecting delicate components.

4

Energy Absorption in a 1D Array of Axially Aligned Pendulums with Linear Torsional Coupling

4.1 Introduction

Mechanical wave propagation is a field of ongoing research with applications in shock attenuation, energy harvesting, and vibration dampening [6–9, 12]. There are also parallel fields in acoustics and optics in which many of the same principles are used in MEMS devices. This chapter will demonstrate a general rotational system with behavior similar to translational systems in the literature.

Classification of system propagation and attenuation zones is an important step in wave propagation analysis in systems subjected to harmonic excitation [19]. Bandgaps, frequency regions in which no propagating wave modes exist [13], can be used to filter input over a designed frequency range. The use of bandgaps is less straightforward in nonlinear systems, since they do not have a propagation constant [18] and system behavior can be largely amplitude dependent [57, 65]. A variety of nonlinear systems have been presented in the literature, with unique approaches to analyzing their propagation behaviors [16, 51, 53–56, 64, 75]. In this chapter, the nonlinear

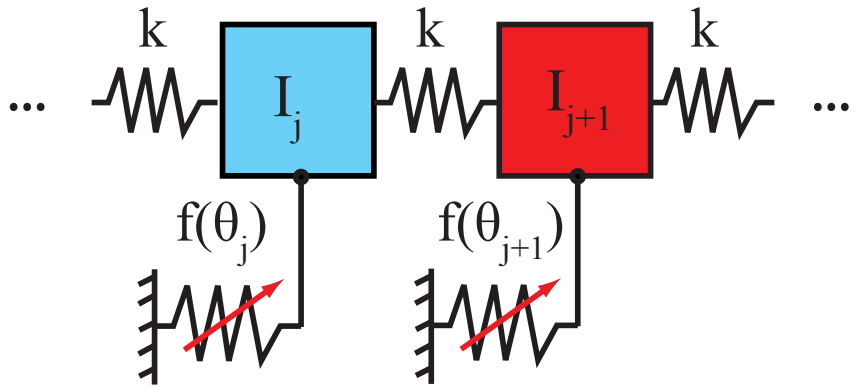

FIGURE 4.1: The 1D unit cell with N pendulums of mass moment of inertia I_j and torsional couplings k that makes up the infinite system. The nonlinear gravitational restoring force is a function of each pendulum's deflection angle θ.

restoring forces will be simplified by only considering small amplitude oscillations.

Since vibrational systems can often be subjected to shock loads, this chapter also considers the system response to an impulsive load. There has been significant study of shock propagation in one dimensional granular chains [2–4], and it has been identified that varying the properties of each adjacent bead can provide significant absorption advantages [49, 50, 52, 76]. This work will demonstrate that coupled oscillators of varying masses similarly achieve decreased amplitude when subjected to impulsive loads.

4.2 System Description

This chapter examines wave propagation and energy absorption in a 1D array of axially aligned pendulums. Two related versions of the same system are investigated. The first will consider an unforced chain where one unit cell consists of two pendulums of different masses. This unit cell will represent a chain of infinite length by wrapping it upon itself through use of circulant matrices as in Eqs. 4.2 and 4.3. The block diagram for this system can be seen in Fig. 4.1 where $f(\theta)$ represents the uncoupled restoring force due to gravity acting on the swinging pendulum. Unit cell analysis

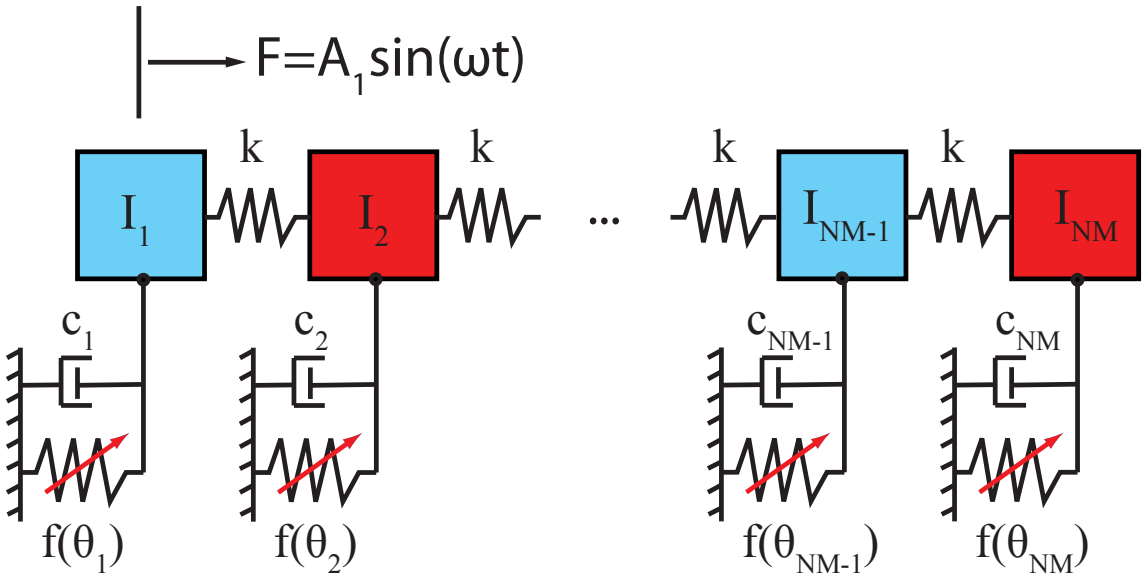

FIGURE 4.2: Block diagram of the finite system composed of M unit cells each containing N=2 pendulums. To contrast the individual unit cell of Fig. 4.1, for this finite representation, the first pendulum is subjected to harmonic excitation at frequency ω and each pendulum has a small amount of viscous damping c.

will provide insight in the design of a realistic finite system since most qualitative behavior will be comparable, and it can be regarded as an ideal case.

The second case discussed in this chapter considers a finite chain of pendulums composed of a variable number of unit cells. Dampeners have been introduced to this system in addition to base excitation as shown in the block diagram of Fig. 4.2. A visualization of the general system can be seen in Fig. 4.3. While not depicted in this figure, torsional couplings are considered to link each pendulum to its neighbors.

This design provides beneficial physical characteristics not present in the systems of the preceding chapters, while still illustrating desired wave propagation behaviors. The effect of damping can be significantly reduced from the already low levels in the ball bearing by increasing length or mass of the pendulum. There is no risk of collision of adjacent oscillators since the plane of motion is perpendicular to the plane of wave propagation. This perpendicular direction of motion also allows easier

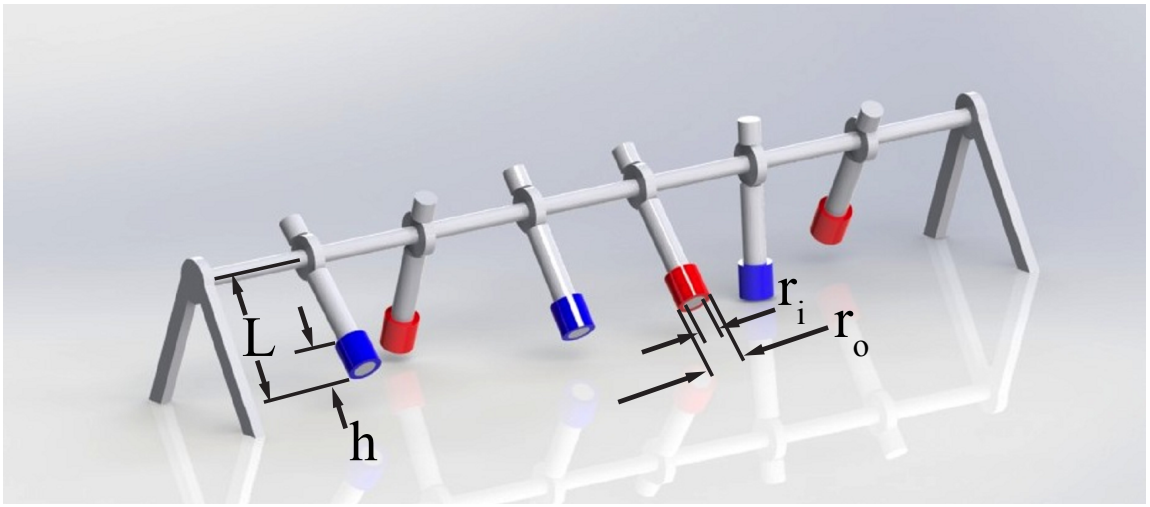

FIGURE 4.3: Visual representation of a finite chain of $M = 3$ unit cells of axially aligned pendulums.

external manipulation of specific oscillators.

4.3 Mathematical Model

This chapter will explore the band gap regions associated with both the infinite and finite cases of the system described above. The pendulums will be modeled as cylindrical ring masses of mass m_a and m_b (for the first and second pendulums comprising a single unit cell) attached to uniform, rigid, slender rods of radius r_i and length l. The masses have an inner radius r_i and outer radius r_o and a height of h. Linear torsional couplings will apply forces to each pendulum proportional to the difference in angular displacement between the pendulum and each of its neighbors.

4.3.1 Equations of Motion

A generalized equation for the j^{th} pendulum is given by

$$I_j\ddot{\theta}_j = k\left(\theta_{j+1} - \theta_j\right) + k\left(\theta_{j-1} - \theta_j\right) - (m_j + m_{rod})gL_j \sin\left(\theta_j\right), \tag{4.1}$$

for $j = 1, ..., N$, where I_j is the pendulum's mass moment of inertia about the point of rotation and L_j is the length from the point of rotation to the pendulum's center

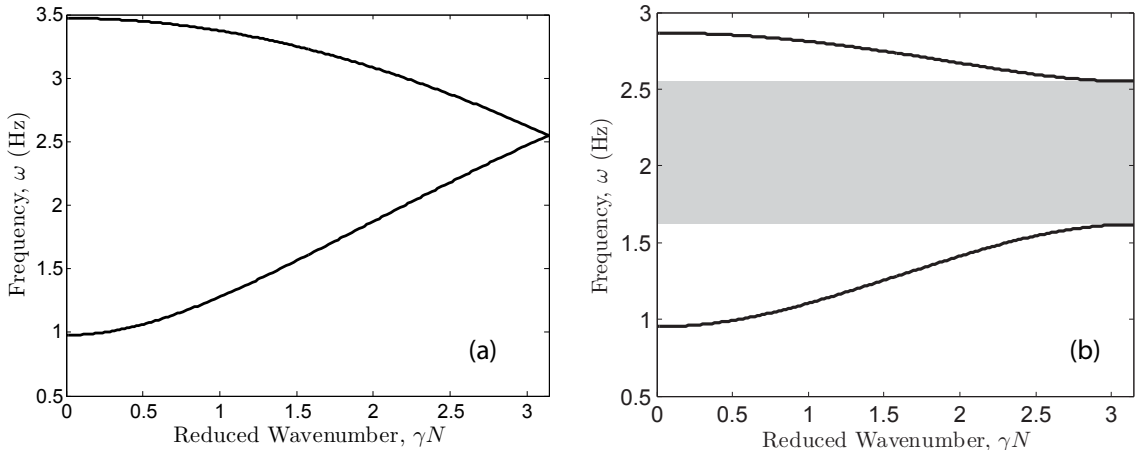

FIGURE 4.4: Using parameters from Table 4.1, (a) the homogeneous case where $m_2 = m_1$ shows a single large propagation zone between $1 - 3.5\ Hz$ and (b) the varied case where $m_2 \neq m_1$ (specifically $m_2 = 4m_1$) shows a large central bandgap (shaded) between 2 propagation zones ($.95 - 1.65\ Hz$ and $2.55 - 2.85\ Hz$).

of mass. To model an infinite number of identical unit cells as a single cell wrapped upon itself, the boundary condition $j - 1 = j + 1$ is applied for the case of $N = 2$ oscillators per unit cell. Therefore, the governing equations of motion for a two-pendulum unit cell are

$$I_1\ddot{\theta}_1 = 2k\left(\theta_2 - \theta_1\right) - (m_1 + m_{rod})gL_1 \sin\left(\theta_1\right), \tag{4.2}$$

$$I_2\ddot{\theta}_2 = 2k\left(\theta_1 - \theta_2\right) - (m_2 + m_{rod})gL_2 \sin\left(\theta_2\right). \tag{4.3}$$

4.3.2 Bandgap Regions

As the energy propagation through this system takes the form of a traveling wave, a traveling wave solution was assumed in the form

$$\theta_j = A_j e^{i(j\gamma - \omega t)} \tag{4.4}$$

where A_j is the amplitude of the j^{th} oscillator, γ is the wavenumber, and ω the frequency.

Inserting the assumed solution into Eq. 4.1 generates a series of complex equations. A nonlinear displacement model would result in amplitude dependent behavior [57, 65], but by assuming a small angle of displacement, these equations take the form of the approximation

$$-I_j\omega^2 A_j = ke^{-i\gamma}A_{j-1} + ke^{i\gamma}A_{j+1} - (2k + (m_j + m_{rod})gL_j)A_j. \tag{4.5}$$

These equations can therefore be simplified into a standard eigenvalue problem [17] of the form

$$\left(\mathbf{S}\left(\gamma\right) - w^2\mathbf{I}\right)\mathbf{A} = \mathbf{0}, \tag{4.6}$$

where $\mathbf{S}(\gamma)$ is a combination of the mass and stiffness matrices, $\mathbf{I}$ is the NxN identity matrix, and $\mathbf{A}$ is an Nx1 vector containing the oscillation amplitudes for each pendulum.

The eigenvalues of this equation were then solved using MATLAB, yielding the band structure of wave frequencies ω for varying wave numbers γ, as shown in Fig. 4.4 (reduced wavenumber γN is plotted to maintain the convention often used in the literature). The left plot, Fig. 4.4(a) represents the case where $m_2 = m_1$ and there are no bandgaps. Energy will be able to propagate through the homogeneous system across the entire usable frequency band. As expected [77], changing $m_2 = 4m_1$ results in a central bandgap, indicated by the shaded region of Fig. 4.4(b).

4.3.3 Oscillation Amplitudes

In addition to an infinite chain of pendulums, a finite system of a varying number of unit cells was analyzed. A periodic forcing function was added to the first pendulum and dampeners were introduced to all oscillators in this scenario. The resulting

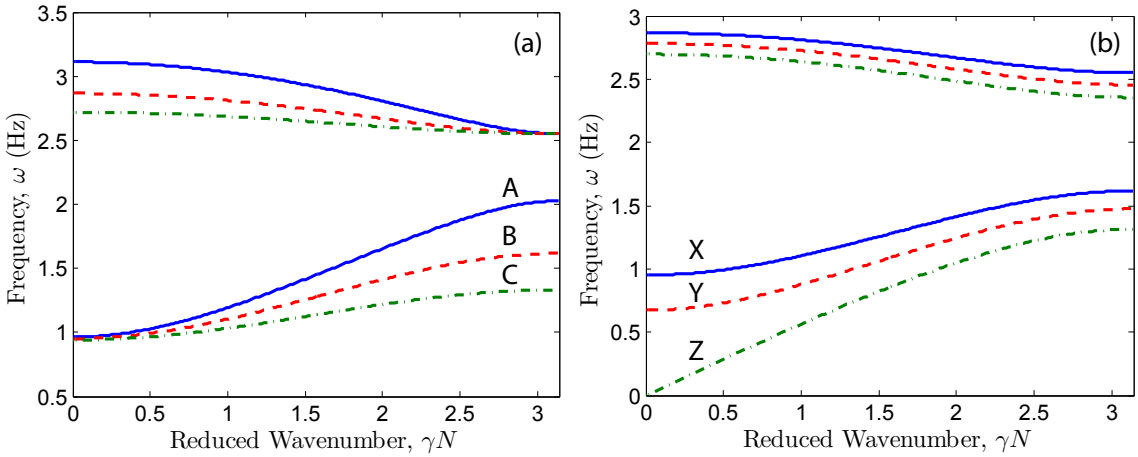

FIGURE 4.5: (a) Resultant increase in the size of the band gap from increasing the value of m_b, (A) $m_b = 2m_a$, (B) $m_b = 4m_a$, (C) $m_b = 8m_a$, and therefore the difference between m_b and m_a and (b) resultant downward shift in the location of the band gap region from decreasing the strength of the uncoupled restoring force (X) $g = 9.81m/s^2$ (Y) $g_2 = 0.5 * g$, (Z) $g_3 = 0$. The lower pass band starts at zero when the restoring force is zero and the only forces acting on each oscillator are coupled.

equations of motion for each pendulum in a chain of M unit cells are

$$I_1\ddot{\theta_1} = k\left(\theta_2 - \theta_1\right) - c_1\dot{\theta_1} + F_1 e^{i\omega t} - (m_1 + m_{rod})gL_1 \sin\left(\theta_j\right), \tag{4.7}$$

$$I_j\ddot{\theta_j} = k\left(\theta_{j+1} - \theta_j\right) + k\left(\theta_{j-1} - \theta_j\right) - c_j\dot{\theta_j} - (m_j + m_{rod})gL_j \sin\left(\theta_j\right), \tag{4.8}$$

$$I_{NM}\ddot{\theta}_{NM} = k\left(\theta_{NM-1} - \theta_{NM}\right) - c_2\dot{\theta}_{NM} - (m_2 + m_{rod})gL_2 \sin\left(\theta_{NM}\right). \tag{4.9}$$

These equations of motion can be written in matrix form as

$$\mathbf{I}\ddot{\theta} + \mathbf{C}\dot{\theta} + \mathbf{K}\theta + \mathbf{G} = \mathbf{F}. \tag{4.10}$$

Inserting a solution form

$$\theta_j = A_j e^{i\omega t} \tag{4.11}$$

into Eq. 4.11 yields a linear set of equations which can be solved for the amplitude of each pendulum,

$$\left(-\omega^2\mathbf{I} + i\omega\mathbf{C} + \mathbf{K} + \mathbf{G}\right)\vec{A} = \vec{F}. \tag{4.12}$$

Table 4.1: Physical Parameters for Infinite System

Name	Designation	Value
Rod Mass	m_{rod}	0.04 kg
Rod Length	L_{rod}	0.3 m
Cylinder 1 Mass	$m_a = m_{1,3,5,...}$	0.04 kg
Cylinder 2 Mass	$m_b = m_{2,4,6,...}$	0.16 kg
Cylinder Height	h	0.02 m
Cylinder Inner Radius	r_i	0.005 m
Cylinder Outer Radius	r_o	0.01 m
Linear Coupling	k	0.5 Nm/rad
Pendulums per Unit Cell	N	2

4.3.4 Analysis

This section will perform parameter analysis of the ideal (infinite) case, and identify several variables that cause differing behavior in the finite system. The two design parameters for the ideal system are the difference in mass between adjacent pendulums and the strength of the uncoupled restoring force. In the finite system, the overall system length and viscous damping are the two parameters that will cause the realistic system behavior to differ from the ideal case.

4.3.5 Unit Cell Parameters

The first half of this investigation focused on an infinite periodic structure composed of pendulums and torsional couplings. Table 4.1, depicts the physical parameters inserted into the model.

Note that the mass of the second cylindrical weight is four times that of the first mass in the unit cell. This difference is necessary to ensure the existence of a band gap region as energy of all frequencies will propagate through a homogeneous unit cell. By applying the mathematical model to this system and solving for the band structure of wave frequencies ω for varying wave numbers γ, it became apparent that a large band gap region exists for this system as illustrated in Fig. 4.4.

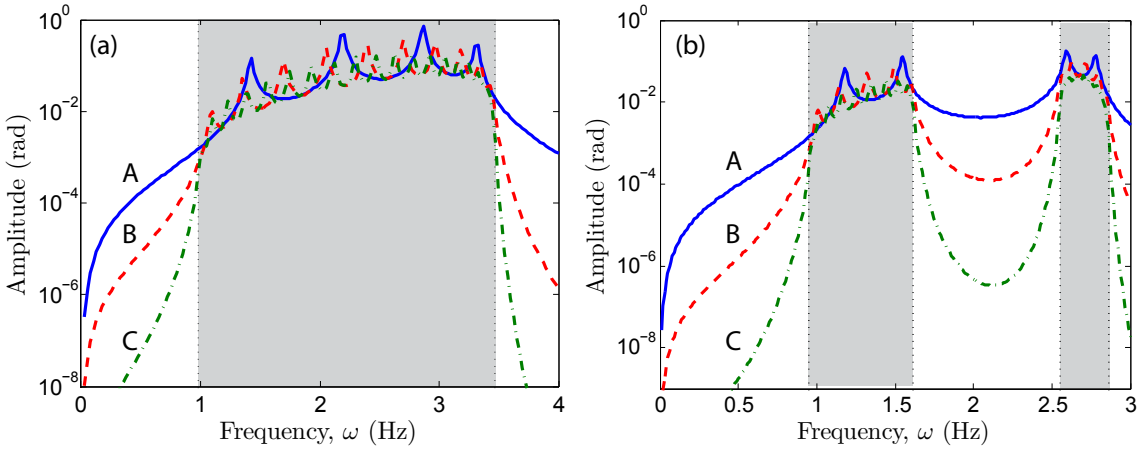

FIGURE 4.6: Amplitude of the last oscillator in chains of various lengths (A) M=2, (B) M=5, (C) M=10, (a) in the homogeneous system of Fig. 4.4(a) without bandgaps and (b) the varied masses system of Fig. 4.4(b) with a central bandgap. Though propagation zone (shaded) behavior is largely consistent between chains of varying lengths, amplitude attenuation is significantly increased in the attenuation zones (unshaded) of longer chains.

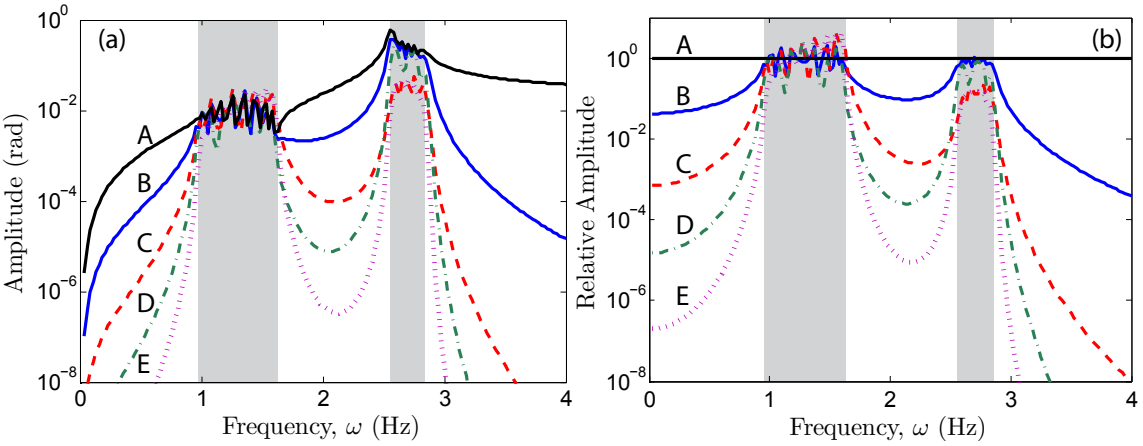

FIGURE 4.7: (a) Amplitude of selected, representative pendulums [(A) Pendulum 1 (the excited pendulum), (B) Pendulum 5, (C) Pendulum 10, (D) Pendulum 15, and (E) Pendulum 20] throughout the length of an M=10 unit cell chain when the first pendulum is excited and (b) normalized in reference with the excited pendulum's motion. The propagation zones are shaded, and although the second pass band has higher absolute amplitude, the relative motion noticeably decreases along the chain in this region. Even though attenuation is much less than in the adjacent bandgap where amplitudes are predictably lower further along the chain, the factor of 10 reduction in amplitude in the second propagation zone is still significant. Force and viscous damping are listed in Table 4.2.

Using these parameters, energy is not expected to propagate through the system for excitation between 1.62 Hz and 2.55 Hz. Furthermore, excitation at frequencies below 0.95 Hz and above 2.87 Hz will not propagate through the system. Figure 4.5(a) demonstrates the impact of the relative difference between the masses in the unit cell. When the disparity between the masses is increased, the band gap grows in size and propagation zones become smaller.

Variations in the uncoupled restoring force can also affect the propagation zone sizes and boundaries. As seen in Fig. 4.3, a horizontal support beam ensures that the planar rotation of each pendulum is affected by a full 1g gravitational force. However, this restoring force could be adjusted by misaligning the gravitational field from the motion of the planar pendulums, for example, by tilting the support bar such that each end is at a different height and each pendulum's swing is no longer in the vertical plane. Figure 4.5(b) depicts the influence of gravity. The primary effect of this uncoupled restoring force is to increase the starting frequency of the lower propagation zone, so that it no longer begins at $\omega = 0$ Hz. Thus, the presence of the restoring force creates an additional low frequency attenuation zone. In the extreme, the support bar could be set vertical such that pendulums pivot in the horizontal plane, thus resulting in zero gravitational restoring force and the lower propagation zone would begin at $\omega = 0$ Hz.

4.3.6 Finite System Realization

The second half of this investigation looks at the response of the finite system to a sinusoidal forcing function acting on the first pendulum. The same parameters from Table 4.1 were utilized along with the additional values seen in Table 4.2 representing the external force on the first pendulum and assumed viscous damping. The model described above was used to predict the response of each mass in the system as a function of the forcing frequency. Figure 4.6 shows the predicted response of the last

Table 4.2: Physical Parameters for Finite System

Variable	Value
$c_1 = 0.01(m_1 + m_{rod})$	0.0008 Nms/rad
$c_2 = 0.01(m_2 + m_{rod})$	0.002 Nms/rad
F_1	0.0001 Nm

pendulum in a chain composed of 2, 5, and 10 unit cells ($M = 2, 5, 10$).

The amplitude of each pendulum drops significantly when the frequency of the forcing function is within the band gap predicted by analysis of the infinite system. Furthermore, it can be seen that this response drops further as the length of the chain increases. This result makes intuitive sense as the finite system more closely resembles the infinite case when more unit cells are added to the chain. The smaller local valleys and peaks result from the plotted oscillator being in or out of phase with the base excitation, respectively. These local effects lessen as damping levels increase.

Whereas Fig. 4.6 showed the amplitude of the last pendulum for a system with a varying number of unit cells, Fig. 4.7 shows the amplitude of different pendulums in the same system composed of 10 unit cells. The drop in amplitude along the chain is most noticeable in attenuation zones, however the cause for this phenomenon also occurring in propagation zones is damping. The effect is more clear when amplitudes are normalized in reference to the first pendulum as in Fig. 4.7(b). Though the first propagation zone shows oscillations on the same order of amplitude throughout the entire chain, the second propagation zone actually has a factor of 10 decrease along the chain. Since the applied damping is a function of angular velocity, when amplitude is held constant, velocity is significantly higher as frequency increases. This results in more noticeable energy losses. In an experimental system, where friction is likely to be non-negligible, it is important to anticipate the differing behavior that

each propagation zone is likely to exhibit as a result of increased energy losses at higher frequency.

4.3.7 Impulse Absorption

Vibrational systems are often subjected to impulsive loads. This section numerically analyzes the behavior of the same chain of pendulums when subjected to a single half-sinusoid of input, representing a short duration shock. Figure 4.8 shows the resulting behavior when the pulse's duration is structured to resemble the initial wave of signals that would fall in different attenuation and propagation zones. The magnitude of each pendulum's displacement is primarily a function of the amplitude and duration of the pulse. There is also no discernible affect on the system behavior based on whether the pulse resembles a wave from a propagation zone or band gap, that is, the shock is equally dissipated in all regions, accounting for the difference in duration.

However, these results can be contrasted with Fig. 4.9, which shows the performance of the pendulum chain when subjected to the same impulse, but with each pendulum having identical masses. In this case, initial displacement amplitudes are much greater than the case of Fig. 4.8 where $m_2 = 4m_1$, but settling time is also much faster. The increased settling time in the case of different masses is an example of energy trapping similar to that in Ref. [21]. This would suggest that there are trade offs to energy absorption. Creating a system to dampen harmonic excitation through use of a band gap at the excited frequency will lose some effectiveness in a noisy environment where the system is exposed to additional short duration shocks due to the increased settling time as compared to the homogeneous case.

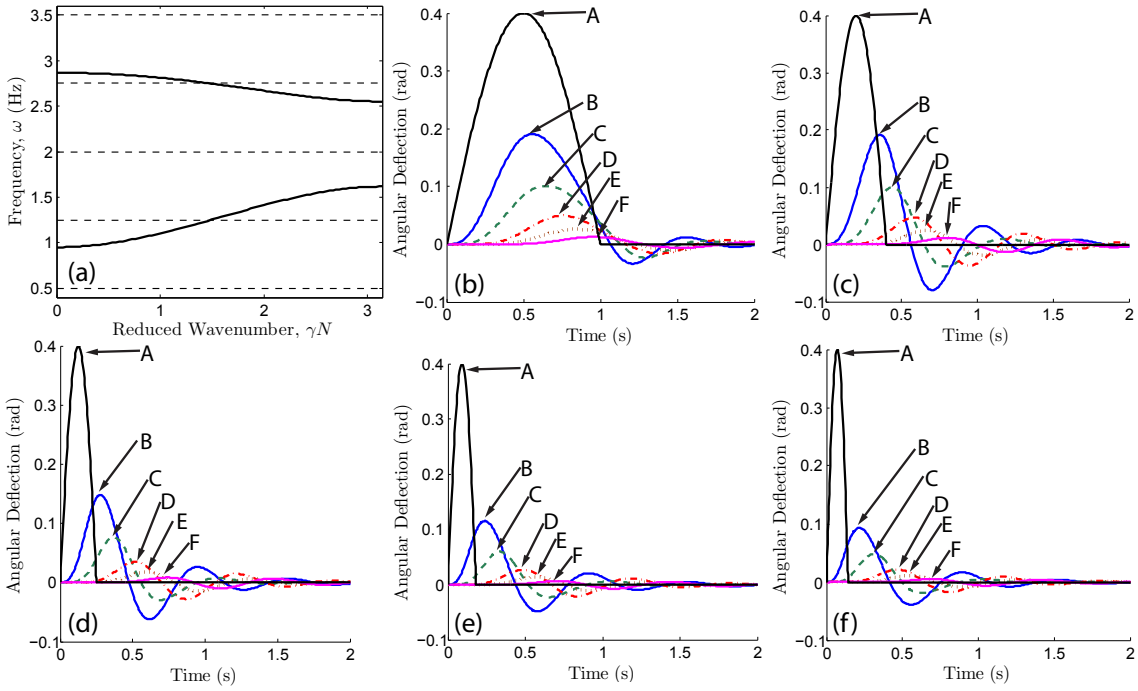

FIGURE 4.8: Impulse absorption in the (A) 1^{st}, (B) 2^{nd}, (C) 3^{rd}, (D) 4^{th}, (E) 5^{th}, and (F) 6^{th} pendulum when a chain is subjected to a single half-sinusoid impulsive force (in the form of prescribed motion of the first pendulum) of duration corresponding to the frequencies shown in (a), each of which falls in a different pass or stop band (due to $m_2 = 4m_1$). Figures (b)-(f) show that shock attenuation is primarily driven by the impulse duration and not by whether the single wave corresponded to a propagation or attenuation zone.

4.4 Conclusions

This chapter demonstrated a method to perform wave propagation analysis on a system of rotating oscillators, coupled torsionally. It was shown that in the case of small angular deflections the analysis mirrored previously studied translational cases. Rotating systems have several practical benefits that a translational system lacks. Since the direction of motion is out of plane with the length of the chain, rigid, permanent, external controls are easier to implement. The uncoupled restoring forces are also easily variable for this type of gravitational system. By increasing the tilt angle, this restoring force can be reduced to zero, thereby eliminating the low frequency attenuation zone if propagation in this range is desired.

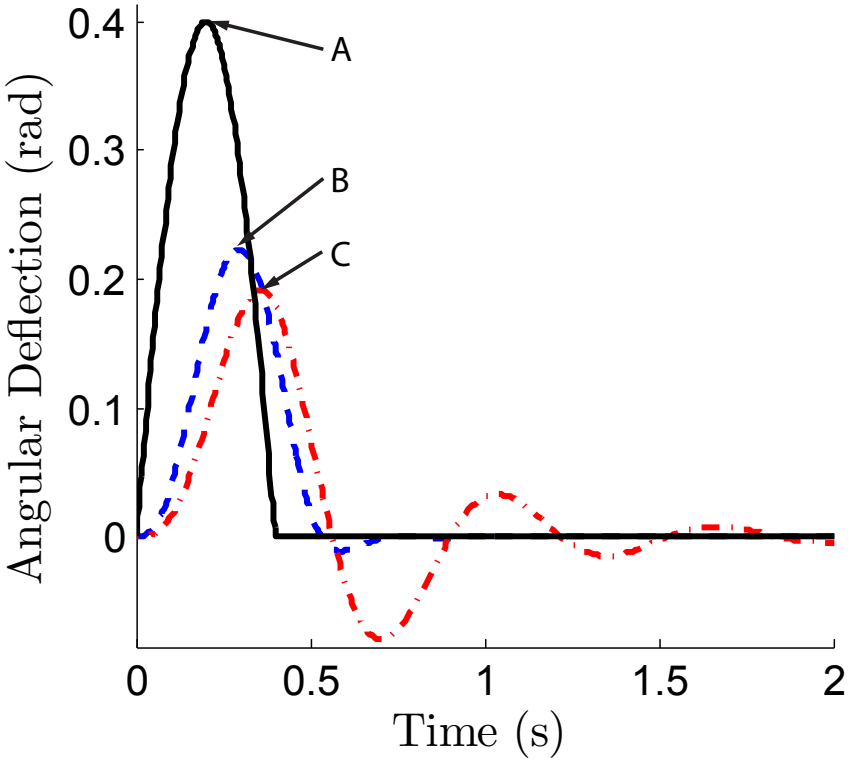

FIGURE 4.9: The lower initial amplitude and longer settling time resulting from energy trapping are evident in this comparison of the 2^{nd} pendulum in (B) homogeneous vs (C) varied mass chains when subjected to (A) a single half-sinusoid impulsive force.

The numerical simulations provide several fundamental insights for construction of the physical experiment used in Chapter 5. It was shown that propagation zones have distinct behavior in realistic systems. In a system where oscillators are subject to viscous damping proportional to velocity, higher frequency propagation zones may actually be indistinguishable from their adjacent attenuation zones depending on the accuracy of measurement devices. The provided example showed a factor of 10 decrease in amplitude throughout the chain in the higher frequency propagation zone as compared to the lower frequency band which required much lower speeds for the same amplitude.

This study also demonstrated the benefits and drawbacks to this system's behavior when subjected to shock loads. In agreement with past studies, it was shown

that the same configuration that causes bandgaps to occur (using different masses for each pendulum) also results in lower amplitude deflection to impulse forces. However, this advantage came with the trade off of a longer settling time. Further study is required to determine which factors are dominant when the shock load occurs during harmonic excitation.

5

Experimental Investigation of Bifurcation Induced Bandgap Reconfiguration

5.1 Introduction

Wave propagation [6–8] in mechanical oscillators has parallels in photonic, phononic and electrical systems. Past studies on the behavior of periodic structures [12] has led to advances in signal processing, wave guiding, filtering, vibration absorbers, and localization. The wave propagation characteristics of discrete lattices can often be grouped into two categories, propagation zones (pass bands) or attenuation zones (bandgaps) [10, 11]. Bandgaps are frequency ranges where no propagating wave modes exist, and typically result from non-homogeneity of masses or stiffnesses, or from defects in the lattice.

The propagation constant technique [13, 17] is a useful tool for analyzing both infinite systems to best visualize idealized behavior as well as practical applications with finite length chains [78]. Nonlinear systems do not have a propagation constant [18], but they can still exhibit propagation and attenuation zone behavior [19] and linearization can still explain system behavior in many nonlinear systems when the

excitation is small and nonlinear effects are not yet dominant [65]. There are many types of nonlinearity [16, 55, 79] that provide useful functionality [20] that would be difficult or impossible to achieve in a linear system such as rectification [68] and wave speed scaling [80].

Active research in the area of wave propagation has largely centered around design and control of bandgap frequency ranges. To match a given system's behavior to the environment in which it will be implemented often requires some level of tuning, which can be performed either during the construction of the device, or through feedback control. Some design advancements [81] have detailed techniques whereby tuning a chain's frequency behavior can be achieved during initial construction through material selection [21, 22], component [82] or lattice [83] shape or dimensions [50, 73], inserted defects or intruders [14, 15, 64, 84], or applied external forces [27]. Alternately, active control techniques have also been proposed to allow a generically designed chain to modify its propagation characteristics through component replacement [24–26], applied currents [74, 85], adjustment of a design variable [23] or operation of a manual switch [5]. However, these techniques all require human intervention and may not be suitable for remote or autonomous operation.

Passive reconfiguration techniques instead allow a chain to alter its wave propagation characteristics as a result of environmental stimuli [56]. This provides a complementary benefit to design and active control, since bifurcation [75, 86] induced changes are inherent to the system design. Some previous systems have described bifurcation induced chaos [66], rectification in a granular chain [67] and filtering in a chain of mechanical oscillators [87]. This chapter will showcase an experimental example of bifurcation induced filtering. Through an external force, the mechanically coupled oscillators comprising a chain will be asymmetrically bistable, resulting in functional behavior similar to a circuit breaker whereby small signals are transmitted through the chain, but high amplitude oscillations instead result in a "trip" in the

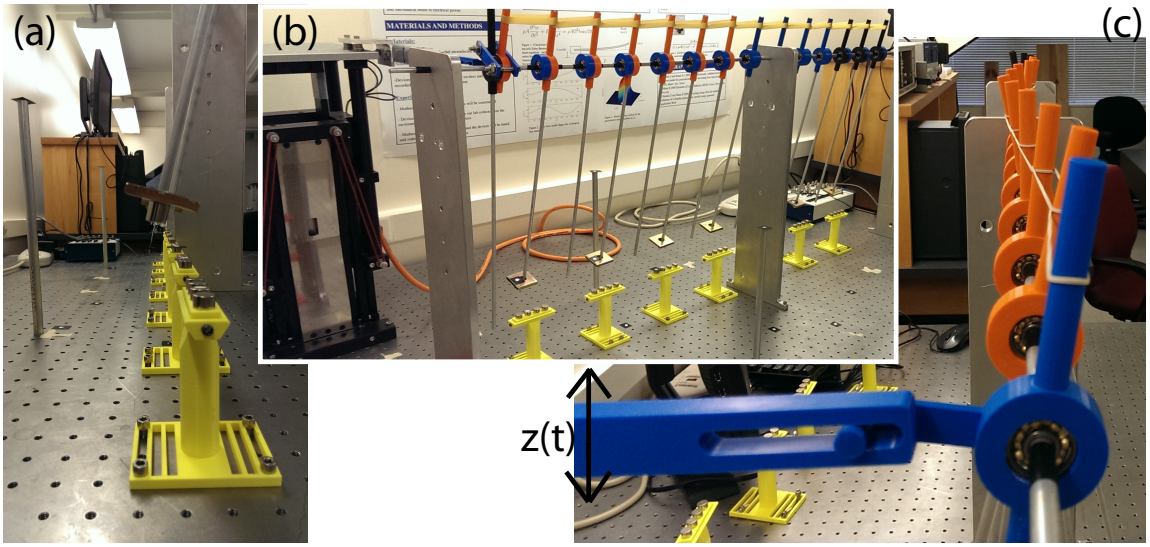

FIGURE 5.1: Photographs of the experimental setup. (a) Pendulums at static equilibrium in the shallow potential well due to gravitational and repulsive magnetic forces. (b) Side view of the 7 unit-cell chain with the vertical shaker on the far left. (c) Front-view closeup of the excitation source. The horizontal slotted section is rigidly attached to a vertical shaker providing prescribed motion $z(t)$, which creates angular rotation in the first pendulum via the pin in slot design.

system and are attenuated. In end applications, this phenomenon could function as a safety feature to protect delicate design components that are unable to withstand sustained exposure to large amplitude input excitation.

5.2 System Description

The system used in this study comprises a 1D chain of axially aligned pendulums made up of repeating dimer unit cells, as seen in Fig. 5.1 and represented by the Hamiltonian

$$\mathcal{H} = \sum_{n=2}^{N} \frac{1}{2} I_n \dot{\theta}_n^2 + E_n(\theta_n) + U_n(\theta_n - \theta_{n-1}). \tag{5.1}$$

Here, θ_n is the pendulum rotation angle of the n^{th} oscillator in a chain of N oscillators where the first is driven by prescribed motion and the N^{th} oscillator in the chain has a free boundary condition. I_n is the pendulum mass moment of inertia, E_n is

the on-site potential including a combination of gravitational and repulsive magnetic forces, and U_n is the interaction potential from nearest neighbor coupling. A ceramic and stainless steel ball bearing is placed inside a 3D printed hub. The pendulum arm consists of a long, slender aluminum rod, press fit into the hub. The printed hub also comprises a short leverage arm above the axis of rotation to allow mechanical coupling between adjacent pendulums. The highly tunable design allows the stiffness coefficient to be easily adjusted by changing the attachment position. Attachment closer to the axis of rotation reduces stiffness and oppositely, increased leverage increases the stiffness coefficient.

The two pendulums in each unit cell consist of one light pendulum without added mass, and a second pendulum with a magnetic tip mass and added mass, visible in Fig. 5.1(b). The magnetic tip and added mass facilitate bandgap creation as well as allow for system bistability through use of additional repulsive magnets affixed to pedestals placed beneath the pendulums. Figure 5.1(a) illustrates an example of asymmetric bistability by aligning the pedestals off-center, that is, not directly beneath the axis of rotation. The use of multiple magnets in the pedestal ensures only planar motion of the pendulums through a channel between two base magnets, whereas a single base magnet could induce out of plane motion as the strong repulsive forces tend to force the pendulum around the pedestal instead of over it.

The system is excited by a vertical shaker, which oscillates periodically with a prescribed motion. The pin and slot mechanism shown in Fig. 5.1(c) is used to convert this vertical excitation to rotational motion of the first pendulum in the chain. Wave propagation occurs between axially adjacent pendulums via mechanical, nearest-neighbor coupling. These nonlinear coupling forces are described in more detail in Sec. 5.3.1 while nonlinear on-site restoring forces are described in Sec. 5.3.2.

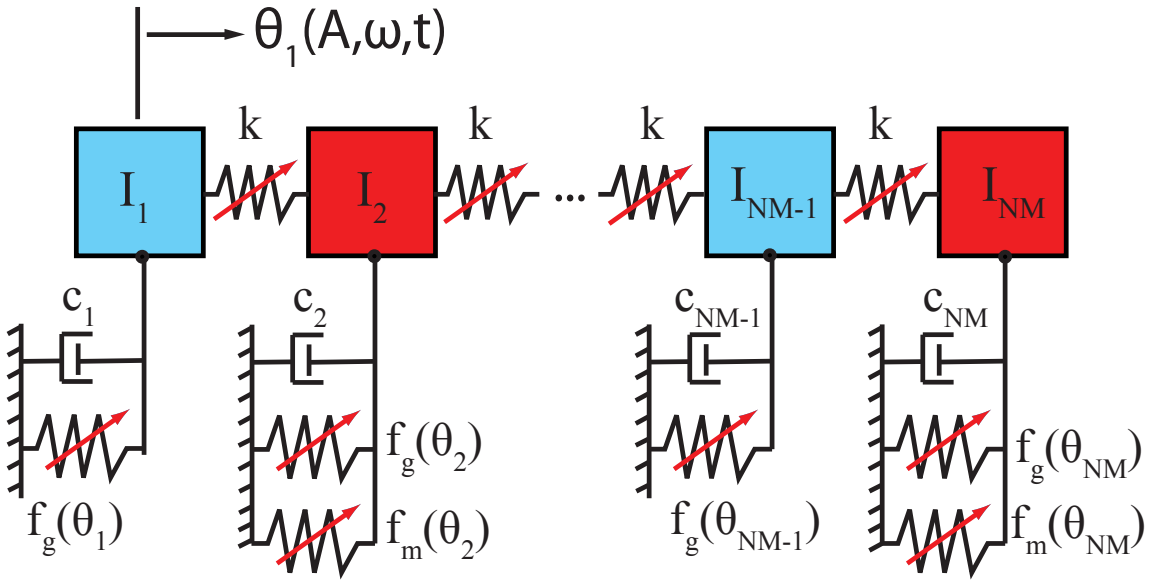

FIGURE 5.2: Block diagram of a finite length chain showing geometrically nonlinear coupling between adjacent oscillators, free boundary counditions, and an applied force to the first mass. All oscillators have an independent, nonlinear, restoring force f_g (gravity), light damping, and alternating masses have an additional nonlinear force f_m due to repulsive magnets on a pedestal beneath the pendulum swing. Blue (light gray) and red (dark gray) mass coloration represent the two repeated masses comprising the dimer chain.

5.3 Mathematical Model

This section mathematically describes the forces present in the system. Although the coupling nonlinearity was not required to achieve the desired reconfiguration, it provides a highly customizable torsional spring. Similarly, the use of repulsive magnetics beneath alternating pendulums lends itself to tuning through changing the position and rotation angle of the base magnet pedestal. Physical parameters were specifically chosen in this case to only allow two stable static equilibria, with all pendulums in the same potential well. By decreasing the stiffness coefficient of the coupling force between nearest neighbors, it would alternately be possible to have a much more complicated system with a very large number of equilibria. In those hybrid equilibrium states where adjacent pendulums can be in opposite

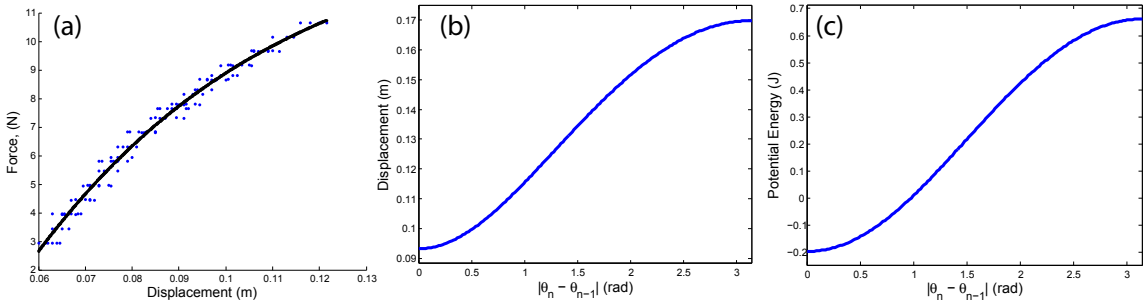

FIGURE 5.3: (a) Experimental force versus displacement points that characterize the behavior of the elastic coupling bands. A cubic polynomial regression (solid black line) shows a good fit of the experimentally collected data (blue dots) over the range of motion seen in the experiments. (b) The mapping from angular separation between adjacent pendulums to the stretched displacement of the elastic nearest neighbor coupling shows the nonlinear relationship from the 0.071 m leverage arm above the axis of rotation and 0.093 m separation between outer edges of adjacent pendulum hubs. (c) Resulting potential energy of the elastic coupling between neighboring pendulums as a function of their angular separation.

potential wells, there are potentially many more distinct sets of wave propagation characteristics besides the two present with the current configuration.

5.3.1 Geometrically Nonlinear Coupling

Two sources of geometrically nonlinear coupling are introduced in the design of this system. As seen in Fig. 5.1(c), the first occurs in converting the vertical motion of the external shaker device $z(t)$ into rotational motion of the driven pendulum θ_1. The external excitation will take the form of prescribed motion as

$$z(t) = \Gamma(t)\sin(\omega(t)t), \tag{5.2}$$

where $\Gamma(t)$ and $\omega(t)$ are the amplitude and frequency at time t, and where the amplitude and frequency may themselves be functions of time as in the case of a frequency sweep. Using a pin in slot connection, the rotational motion of the first pendulum can then be represented by

$$\theta_1 = \sin^{-1}\left(\frac{z(t)}{l_z}\right), \tag{5.3}$$

where l_z is the length in the $y-z$ plane from the pin to the axis of rotation at the center of the first pendulum's bearing.

Coupling between adjacent oscillators is achieved using elastic bands connected to a short leverage arm protruding above each ball bearing hub, also visible in Fig. 5.1(c). The mapping that converts the difference in angular rotation between adjacent pendulums to a change in linear displacement of the elastic band is shown in Fig. 5.3(b). The bands used were measured as having variable stiffness coefficients for changes in elongation. Force versus displacement was fit by a cubic polynomial over the usable range of values as seen in Fig. 5.3(a). Viscoelastic effects were assumed to be negligible.

The potential energy of each coupling band is then represented by the equation

$$U_n = \frac{p_1}{4}x_{n,n-1}^4 + \frac{p_2}{3}x_{n,n-1}^3 + \frac{p_3}{2}x_{n,n-1}^2 + p_4 x_{n,n-1}, \tag{5.4}$$

where $p_1 - p_4$ are the coefficients of the nonlinear stiffness solved via a polynomial regression of the experimentally collected characterization data and $x_{n,n-1}$ is the linear elongation of the band connecting pendulum n to pendulum '$n-1$'. $x_{n,n-1}$ is a function of the rotation angles of each pendulum and is represented by the equation

$$x_{n,n-1} = \sqrt{x_0^2 + \left(2l\sin\left(\frac{\theta_n - \theta_{n-1}}{2}\right)\right)^2}, \tag{5.5}$$

where x_0 is the separation distance between each pendulum along the x-axis, l is the leverage distance in the $y-z$ plane between the band connection and the axis of rotation, and θ_n and θ_{n-1} represent the angular displacements of adjacent pendulums. Fig. 5.3(c) illustrates the effect of this geometric nonlinear coupling. Small angular displacements result in a convex potential energy curve. This can be a beneficial feature in systems in which the desired behavior would be to exploit the large amplitude oscillations that result when adjacent oscillators are out of phase with each

other by allowing larger angular separations than would occur with linear coupling for a given potential energy.

5.3.2 On-Site Restoring Forces

Two nonlinear, on-site, restoring forces also affect the oscillators in the system. Gravitational forces act on all pendulums, and repulsive magnetic forces act on alternating (even) pendulums. The gravitational potential energy is represented by

$$E_g = m_n g h_n (1 - \cos(\theta_n)), \tag{5.6}$$

where m_n is the pendulum's total mass, g represents the gravitational constant and h_n is the radius of gyration.

The energetic interactions between the magnetic tip mass and the pedestal magnets can be described most simplistically by assuming a magnetic dipole model for each magnet, and that eddy current effects of the added mass are negligible. The analytical solution of the magnetic energy interaction between two dipoles of magnetic moments $\mathbf{m}_1 = |\mathbf{m}_1|\mathbf{n}_1$ and $\mathbf{m}_2 = |\mathbf{m}_1|\mathbf{n}_2$ separated by the distance vector $\mathbf{r} = r\mathbf{n}_0$ is given by

$$E_m = \frac{\mu_0 |\mathbf{m}_1||\mathbf{m}_2|}{4\pi r^3} \left((\mathbf{n}_1 \cdot \mathbf{n}_2) - 3(\mathbf{n}_1 \cdot \mathbf{n}_0)(\mathbf{n}_2 \cdot \mathbf{n}_0) \right), \tag{5.7}$$

where $\mathbf{n}$ is the directional unit vector indicating magnet orientation and μ_0 is the permeability of free space.

Finite element modelings are performed to verify the accuracy of the magnetic dipole assumption. The numerical calculations are performed on COMSOL Multiphysics 4.3 using the module Magnetic Fields, No Current. The total magnetic energy E_m of the pendulum magnet is extracted after each calculation for different pendulum position from $\theta = -30^\circ$ to $\theta = 30^\circ$. The total magnetic energy obtained is the sum of the internal magnetic energies, the magnetic interaction energy between the pedestal magnets, and the magnetic interaction energy between the pendulum

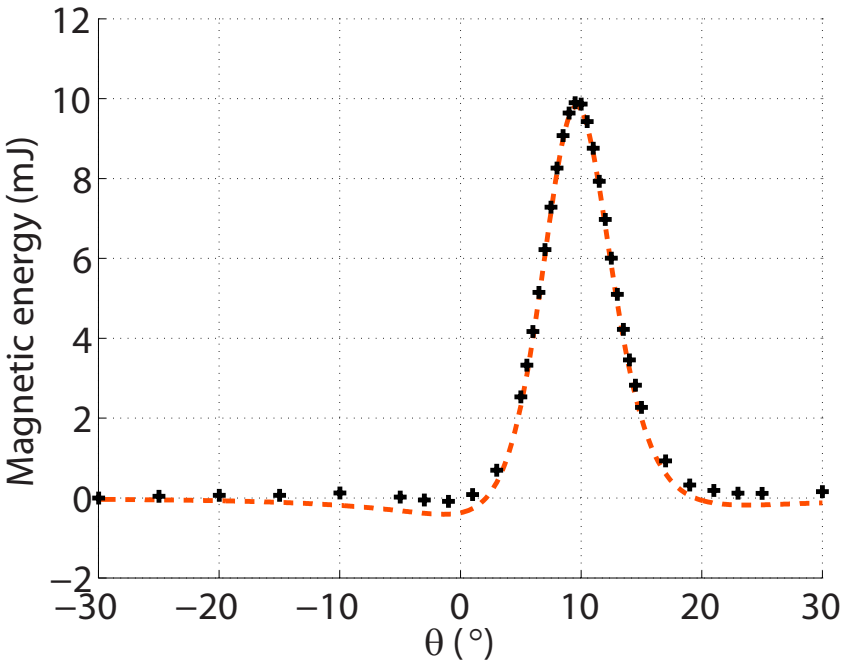

FIGURE 5.4: Comparison of the magnetic energies given by the analytical magnetic dipole model (orange curve) and the numerical calculations (black crosses) when the base pedestal magnets are aligned 7.62 cm. off-center and oriented vertically.

and the pedestal magnets. This last energy is extracted by subtracting the total energy with the other magnetic energies calculated separately (1.7 J).

Fig. 5.4 shows the good accuracy of the magnetic dipole assumption (orange curve) with the numerical simulations (black crosses) that account for the size and shape of the physical magnets. Because the directions of the magnets are opposite, the magnetic interactions are mainly repulsive (i.e. positive energy). The maximum interactions occur at $E_m = 9.8\ mJ$ for $\theta = 9.6°$ when the magnets are the closest. The interactions decrease rapidly and are almost null below $\theta = 0°$ and above $\theta = 20°$. This good match between the magnetic dipole model and the finite element model can be explained by the sufficiently large distance of separation between the magnets (four times their height). The maximum differences of 0.35 mJ are observed near $\theta = 0°$ and $\theta = 20°$.

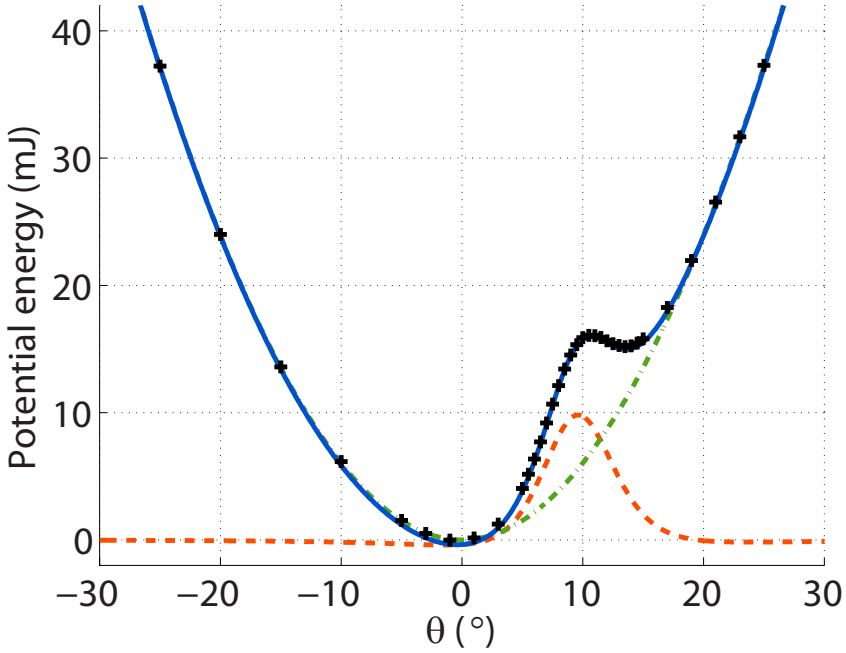

FIGURE 5.5: The total potential energy (blue, solid) is the sum of the gravitational energy (green, dash-dot) and the magnetic energy (orange, dash). The software numerical calculation results (black crosses) match very closely with the analytical model over the entire range.

5.3.3 Solving for System Equilibria

The total potential energy of each even pendulum's on-site restoring force is the sum of the magnetic and the gravitational energies

$$E_n(\theta_n) = E_m + E_g, \tag{5.8}$$

and has been plotted for representative cases in Fig. 5.5. Unlike the magnetic energy, the gravitational energy is minimal for $\theta = 0°$ and increases at extreme angles. Their inverted evolutions lead to two energy wells and consequently to a bi-stable system. Indeed, the total potential energy reaches a local maximum at $\theta = 9.7°$, and two local minimums at $\theta = -1°$ and $\theta = 18.5°$, stable positions of the pendulum.

Since the gravitational energy minimum and the magnetic energy maximum occur at different angles, non-symmetric behavior is observed around the local maximum,

with different energy levels in the two wells.

The two masses that comprise a unit cell will also have slightly different equilibrium positions than each other, the difference of which is inversely proportional to the stiffness coefficient of the coupling force. This can be easily visualized by considering that even pendulums are repulsed from the downward pendulum position by magnetic forces, and the odd pendulums are not. This will cause the odd pendulums to sag to an angle closer to 0°, while being held up by the even pendulums. This coupling force will also pull the even magnets to an equilibrium position at an angle slightly closer to 0° than predicted in Fig. 5.5, which did not include the coupling terms.

For the bistable system, the two sets of equilibria are solved numerically by minimizing Eq. 5.1, after setting velocity equal to zero and substituting Eq. 5.4 for each coupling band, Eq. 5.7 for each repulsed even pendulum, and Eq. 5.6 for the non-magnetic, odd pendulums.

5.4 Theoretical Behavior

Bandgap and bandpass regions occur for small oscillations about each stable equilibria and can be calculated by modeling an unforced, infinite chain as a single unit cell with periodic boundary conditions. Since the analyzed chain is bistable, it will need to be linearized around both stable equilibria using the following assumed solution form of a traveling wave

$$\xi_n = A_n e^{i(n\gamma - \omega t)}, \tag{5.9}$$

where A_n is the amplitude of the n^{th} oscillator, and γ is the wave number. The two equations of motion for the dimer unit cell are then rearranged into an eigenvalue problem

$$\left(\mathbf{K}(\gamma) - \omega^2 \mathbf{M}\right) \mathbf{A} = \mathbf{0}\,, \tag{5.10}$$

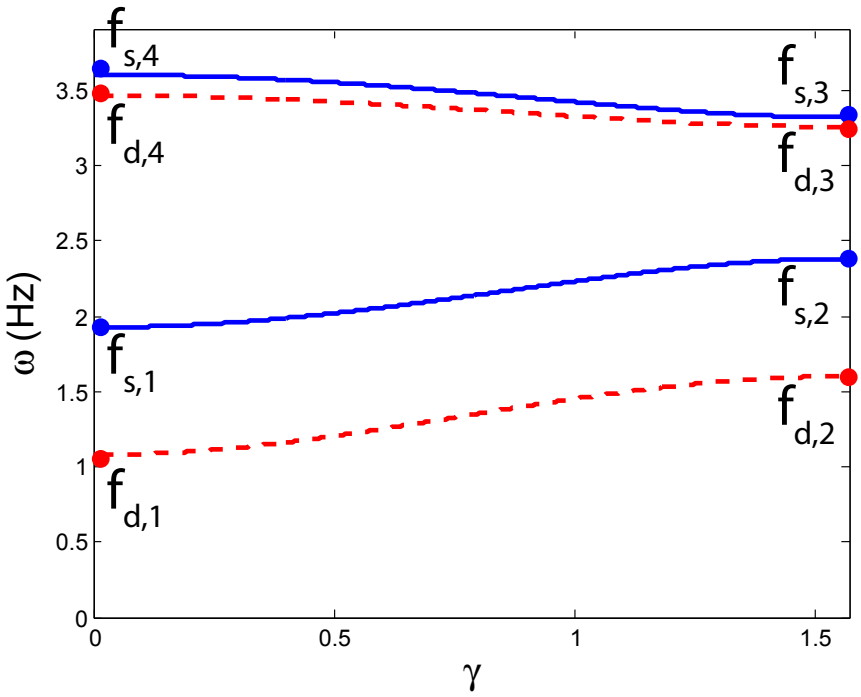

FIGURE 5.6: Linear spectrum of the bistable dimer chain over the first Brillouin zone. Expected propagation zones are seen in the deep potential well (red dashed) and shallow potential well (blue solid). The attenuation zone between 0-1 Hz exists due to the onsite gravitational restoring force on each oscillator. The presence of a shallow well propagation zone in a deep well attenuation zone around $\omega = 2\ Hz$ provides the opportunity for bifurcation induced filtering.

for mass and stiffness matrices $\mathbf{M}$ and $\mathbf{K}$ respectively.

Using the masses and stiffnesses relevant to the experimental setup used in this chapter, the expected linear spectra of the experimental system are solved and plotted in Fig. 5.6, where the blue solid lines represent the shallow potential well and red dashed lines the deep potential well. It can be clearly seen that in this case, the propagation zones do not coincide, owing to the asymmetry of the magnetic repulsive forces on alternating magnetic pendulums. Section 5.5.2 will later show experimental results of an amplitude sweep occuring with excitation frequency 2.1 Hz which should be noted as falling in a propagation zone of the shallow well, and a bandgap of the deep potential well.

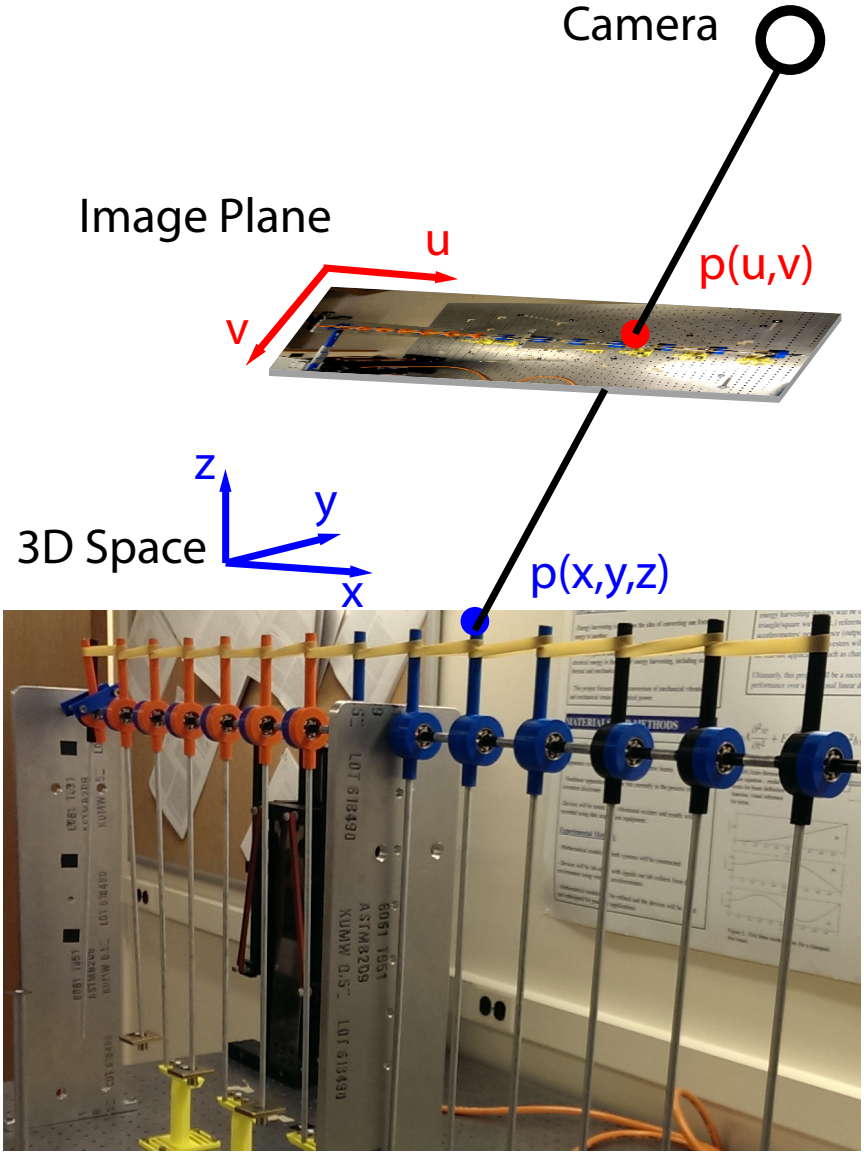

FIGURE 5.7: Illustration of the computer vision technique used for data collection from an overhead camera. The DLT method that allows camera calibration by corresponding known reference points in 3D space to their locations in the 2D image plane is then later used in reverse to solve for the (y,z) coordinates of point p from recorded (u,v) positions and the known x coordinates (due to the physical construction and constrained motion of the pendulums).

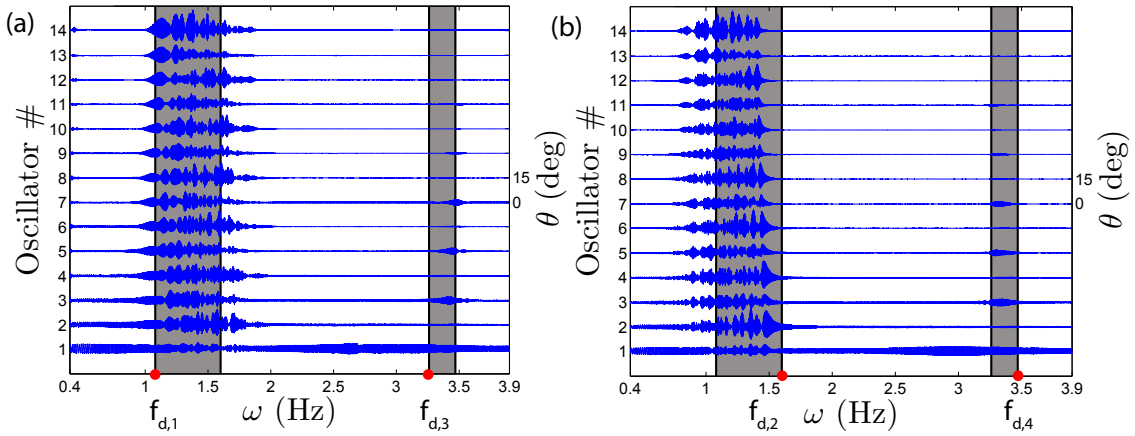

FIGURE 5.8: Experimental results showing the oscillations of each pendulum in a 7 unit cell dimer chain during a frequency (a) upsweep and (b) downsweep of duration t=430s. Initial conditions place the chain in the deep potential well of the asymmetrically bistable system. $f_{d,1} - f_{d,4}$ and the shaded areas represent the theoretically predicted propagation zones from Fig. 5.6. Each oscillator is vertically offset by 15 degrees for clarity with the right, vertical axis providing the relative scale.

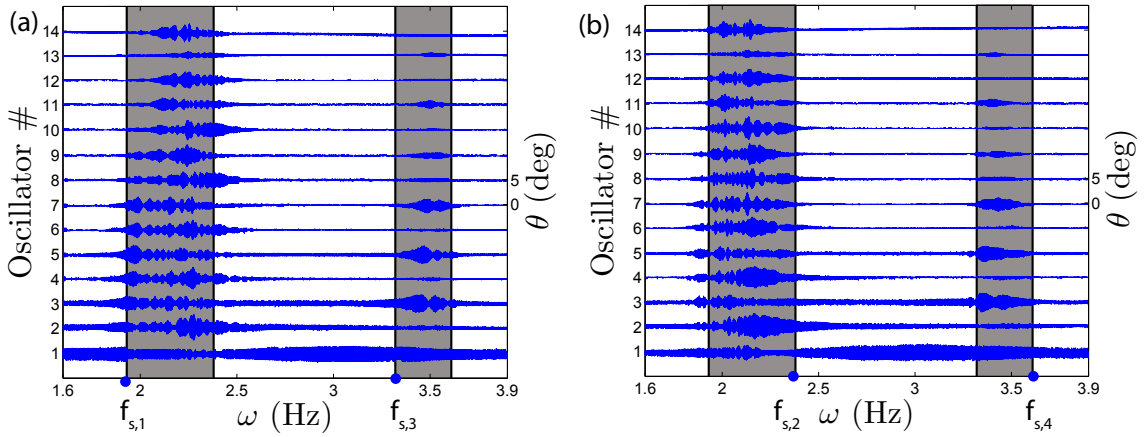

FIGURE 5.9: Experimental results showing the oscillations of each pendulum in an 7 unit cell dimer chain during a frequency (a) upsweep and (b) downsweep of duration t=430s. Initial conditions place the chain in the shallow potential well of the asymmetrically bistable system. $f_{s,1} - f_{s,4}$ and the shaded areas represent the theoretically predicted propagation zones from Fig. 5.6. Each oscillator is vertically offset by 5 degrees for clarity with the right, vertical axis providing the relative scale.

5.5 Experimental Results

Data collection for this experiment was performed using computer vision techniques with a single, overhead, 4 megapixel, video camera. The experimental setup is illustrated in Fig. 5.7. The direct linear transform (DLT) method was used to calibrate the camera's location through a customized version of a 3rd-party MATLAB toolkit DigitizingTools [88]. The 11 DLT coefficients are solved by minimizing the residuals of an overconstrained system of equations

$$\begin{aligned} u &= \frac{c_1 x + c_2 y + c_3 z + c_4}{c_9 x + c_{10} y + c_{11} z + 1} \\ v &= \frac{c_5 x + c_6 y + c_7 z + c_8}{c_9 x + c_{10} y + c_{11} z + 1}, \end{aligned} \tag{5.11}$$

using a minimum of 6 known reference coordinates. For increased redundancy, 33 reference points were used. A second function in the DigitizingTools package was then used to perform automatic point tracking of multiple points, specifically the top most point of each of the fourteen pendulums, and one additional point representing the vertical motion of the external shaker.

Once the DLT coefficients are obtained to calibrate the camera's position, Eq. 5.11 can be used in reverse to solve for coordinates in the 3D object space from their pixel positions in the image plane as generated by the auto-tracker. Generically, this results in a line comprising an infinite number of possible locations. However, due to the construction of the system, each tracked pendulum and vertical shaker has a known, fixed x coordinate and constrained motion only in the y-z plane, allowing the specific location on the ambiguous line to be chosen. The following equations represent Eq. 5.11 rearranged to solve for y and z

$$\begin{aligned} z &= \frac{z_{num}}{(vc_{10} - c_6)(c_3 - uc_{11}) + (uc_{10} - c_2)(vc_{11} - c_7)} \\ y &= \frac{c_1 x + c_3 z + c_4 - u(c_9 x + c_{11} z + 1)}{uc_{10} - c_2} \end{aligned} \tag{5.12}$$

where

$$z_{num} = (uc_{10} - c_2)(c_5x + c_8 - v(c_9x - 1)) \\ -(vc_{10} - c_6)(c_1x + c_4 - u(c_9x - 1)). \tag{5.13}$$

The markers tracked by the visual processing software were 0.159 cm circular dots, which filled 2-8 pixels at different points of the recorded video. With the 'find marker centroid' feature activated, errors were generally observed to be minimal. As an example, allowing for ± 2 pixels of error would correspond to approximately 0.0397 cm-0.159 cm in horizontal displacement measurement error. With an 8.9 cm leverage arm from the axis of rotation, variation of that size would result in errors on the order of 0.25°-1.0° of pendulum rotation. These maximal errors are about a factor of 10 smaller than the oscillation amplitudes during propagation zone behavior, and do not appear to affect the qualitative analysis of the system in the following sections.

Using these data collection and analysis techniques, Sec. 5.5.1 describes the frequency response of the system with results of both increasing and decreasing frequency sweeps to identify the linear spectra of the experimental system. Section 5.5.2 then provides experimental results for an amplitude sweep, in which passive bandgap reconfiguration is observed.

5.5.1 Frequency Response

The experimentally determined frequency response of the system is shown in Figs. 5.8 and 5.9 for behavior in the deep and shallow potential wells respectively. Each illustrates two propagation zones, a lower frequency acoustic mode and an optical mode at higher frequency in which the lighter oscillators have more prominent motion. The two figures include both an increasing and decreasing frequency sweep.

Due to low system damping, the transition at the end of a propagation zone, to attenuation behavior, is not precisely measurable since many oscillators maintained

noticeable amplitudes for a long transitory period before settling into the expected reduced behavior. This is evident by the large oscillations to the right of shaded regions in the frequency upsweeps of Figs. 5.8(a) and 5.9(a) and to the left of shaded regions in the frequency downsweeps in Figs. 5.8(b) and 5.9(b). To best compare the experimental results to the predicted bandpass zones, the transitions from attenuation to propagation should be the focus, as indicated by the labeled frequencies of Figs. 5.8 and 5.9.

The low frequency acoustic propagation zone was clearly identified in both potential wells. Strong propagation was also evident through the entire length of the chain, making the frequency bands easy to visually identify. The high frequency optical band was more difficult to identify experimentally since amplitudes decreased rapidly along the length of the chain, however the close qualitative agreement with predicted results is still evident in the shaded regions of Figs. 5.8 and 5.9.

The most striking difference between the lower and upper frequency propagation zones is the amplitude of pendulums near the end of the chain. In the low frequency zone, amplitudes are relatively constant along the entire length, whereas there is a noticeable decline in the higher frequency optical propagation zone, such that movement in the last unit cells is barely noticeable. These behaviors were both predicted in a previous theoretical study[89] and lend support to the assumption of light velocity dependent dissipation. With velocity dependent dissipation, the effects would be expected to be minor at slow speeds, but for a given amplitude, exciting the system at a higher frequency induces greater energy losses and therefore reduced propagation along the chain.

5.5.2 Passive Reconfiguration

A demonstration of passive bandgap reconfiguration is shown in Fig. 5.10 and the waterfall plot of Fig. 5.11. External excitation provided from a vertical shaker is

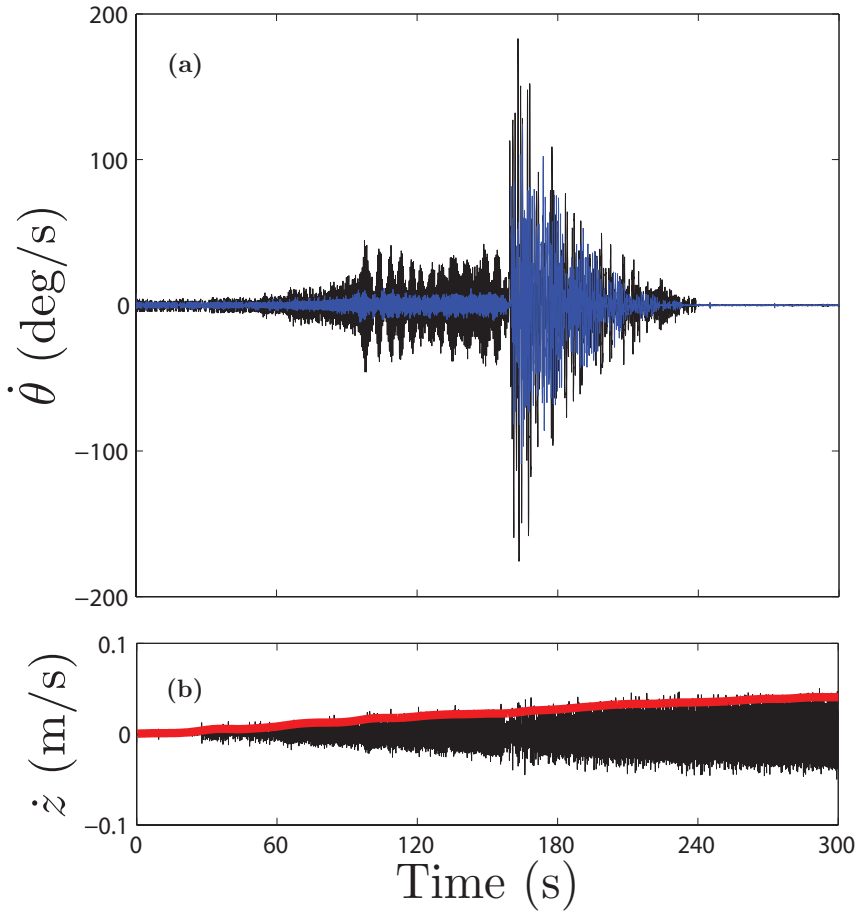

FIGURE 5.10: (a) Oscillations of the 11^{th} (black) and 12^{th} (blue/gray) oscillators in a 7 unit cell dimer chain during an amplitude sweep, shown in (b) where the black line represents velocity of the external shaker with large red(gray) points on each peak as a visual aid. Initial conditions place the chain in the shallow potential well of the asymmetrically bistable system with excitation of $\omega = 2.10\ Hz$, corresponding to a pass band in the shallow well and a stop band of the deep well. In this example, well escape is observed at t=160 s and attenuation zone behavior is realized at t=235 s.

increased linearly as shown in Fig. 5.10(b), and is provided at a constant frequency of 2.1 Hz, which falls in the propagation zone of the shallow well and the bandgap of the deep well, as seen in Fig. 5.6. Figure 5.11 shows the position of each oscillator along the chain during the sweep with the front displayed oscillator representing the start of the chain, and the back as the last. As the excitation amplitude increases, a bifurcation occurs near t=160 s. Through well escape into the deep potential well,

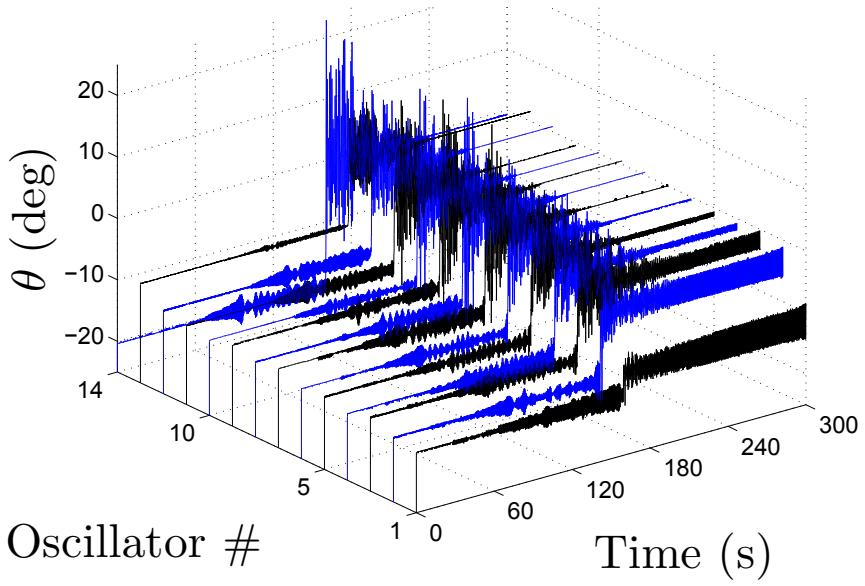

FIGURE 5.11: Oscillations of every pendulum in a 7 unit cell dimer chain during an amplitude sweep. Initial conditions place the chain in the shallow potential well of the asymmetrically bistable system with excitation of $\omega = 2.10\ Hz$, corresponding to a pass band in the shallow well and a stop band of the deep well. Once amplitudes in a single oscillator in the chain are sufficiently large that well escape occurs, the remaining oscillators are similarly pulled into the deep well and after a transitory period, attenuation is observed as amplitudes quickly reduce to near zero levels.

the system reconfigures its wave propagation characteristics. A transitory period of slightly over one minute results from the very low damping level in this system due to the low friction ball bearings and pendulums with added mass. This settling time could be significantly reduced with increased damping, though the loss in propagation when excited in the linear spectrum may offset any gains in performance. As was noted in Sec. 5.5.1, propagation in the upper frequency band is already significantly affected by dissipation, so this trade off of long settling times may be necessary in order to maintain the high level of wave propagation currently observed in the lower frequency band.

Once the system has settled in the deep potential well, this same input frequency 2.1 Hz is instead inside an attenuation zone, and Fig. 5.11 shows that most oscillators have reduced to near zero oscillation amplitude. Figure 5.10(a) details a representa-

tive unit cell, which has stationary velocities during the final minute of the sweep, despite the largest input excitation.

5.6 Conclusion

This chapter demonstrates a passive bandgap reconfiguration for an experimental chain of oscillators. For the case of asymmetric bistability, multiple equilibria arise, and the linear spectra of the two do not necessarily coincide. This allows the propagation behavior to be tuned such that propagation will occur in one well, whereas a bandgap will occur at this frequency in the neighboring well. This provides an opportunity for amplitude dependent filtering, in which low energy environmental input is allowed to be transmitted through the chain, while high amplitudes will instead trigger a well escape and be attenuated.

The study was motivated by recent developments of methods of active control through parameter tuning or component replacement, and acts as a complementary technique that may be beneficial in remote systems or those where manual intervention or monitoring is impractical. This phenomenon provides functionality that is in some ways qualitatively similar to a circuit breaker, and its primary applicability would be in systems with delicate components that are unable to endure sustained exposure to large oscillations.

6

A Hardening-type Nonlinear Energy Harvester with Excited Dynamic Magnifier

6.1 Introduction

There has been significant interest in energy harvesting methods over the past decade paralleling the need to power remote or autonomous sensors and devices. Piezoelectric beams emerged as a capable and robust source of gathering power from vibrating mechanical structures. Early work focused on improving maximum power or power per unit mass of these devices, which generally resulted from tuning linear resonance to an *a priori* known single frequency excitation source.

A significant drawback to those preliminary linear designs was the narrow bandwidth, which made them unsuitable for environments with multi-frequency or variable single-frequency input. Nonlinearities and combinations of linear oscillators were introduced as a way to overcome this obstacle and increase the robustness of a given harvester [28, 90–92]. Several notable examples fall in the categories of linear arrays [35–37], bistable oscillators [29–31], hardening/softening stiffness components [1, 32–34], frequency up-conversion [93], and active tuning [94, 95].

More recently, investigations into the performance of two degree of freedom systems have been shown to provide similar advantages. Dynamic magnifiers introduce a second mass in series between the harvester and excitation source [38–41] in order to drive larger amplitudes in the primary harvesting structure and increase the maximum power output for both harmonic forced excitation and base motion excitation [96]. An alternate configuration with the harvesting structure placed between the vibration source and auxiliary structure [42] has shown improved performance over the previous configuration, and is optimized by greatly preferred design parameters and without the need to modify the harvester's mass or stiffness [43, 44]. Though the magnifier mass is typically non-harvesting, proposed designs like the cutout beam allow both oscillators to produce significant power [97].

Coupled harvester arrays consist of two (or more) degree of freedom designs with multiple coupled oscillators directly connected to the same base. They have also been demonstrated to have a wider bandwidth than a single oscillator [45–47]. However, though peak power in these coupled systems is only slightly lower than the single degree of freedom peak, the effective bandwidth of these coupled systems is measured at a potentially significantly lower power level due to the presence of a central valley between the double peaks. A bistable, electrically coupled design has also shown improved broadband harvesting [98], but the work did not include an uncoupled or linear case for peak power comparison.

This study draws inspiration from both dynamic magnification and coupled oscillator systems by using a design similar to a coupled harvester array, but with component and parameter choice strategies more similar to dynamic magnifiers. Adding a coupled linear dummy oscillator that is similarly driven to a tuned hardening-type nonlinear harvester improves upon the uncoupled case without introducing the drawbacks of the inspiring designs. Models suggest that the addition of this excited dynamic magnifier results in an increased peak kinetic energy of the primary oscil-

lator, at a wider bandwidth, and without the undesirable central valley observed in linear coupled systems. This coupled system can outperform the uncoupled case even when total system mass is held constant, and does not require the significant added cost as in arrays where multiple energy harvesters are used. In practice, the largest drawback of using a hardening-type harvester is the difficulty in achieving the high amplitude solution, as opposed to a coexisting low amplitude solution. When properly tuned, the addition of an excited dynamic magnifier provides large improvements in the range of initial conditions that result in the high amplitude peak, allowing the oscillator to have a greater chance of realizing its maximum potential harvesting capacity.

6.2 System Description

The primary component in the modeled system is a hardening-type nonlinear energy harvesting oscillator as seen in the blue box of Fig. 6.1. The goals of adding an excited dynamic harvester will be to improve the peak kinetic energy, energy per unit mass, and bandwidth of the uncoupled harvester while minimizing added cost and retuning.

For simplicity, a coupled electrical circuit is not included in this model. Kinetic energy of the harvester is used instead as a value expected to be positively correlated with power withdrawn by an optimized electrical circuit. Improved peak kinetic energy should not come only from added mass. Peak kinetic energy should still be improved even when total mass is conserved. The harvester bandwidth is the effective frequency range over which the harvester can generate power above a given threshold when subjected to varying single frequency excitation.

In analyzing the different costs of the system addition, it is assumed that an energy harvester itself is the primary monetary cost of a system and components such as tip masses or fasteners are negligible. For the qualitative cost of design time,

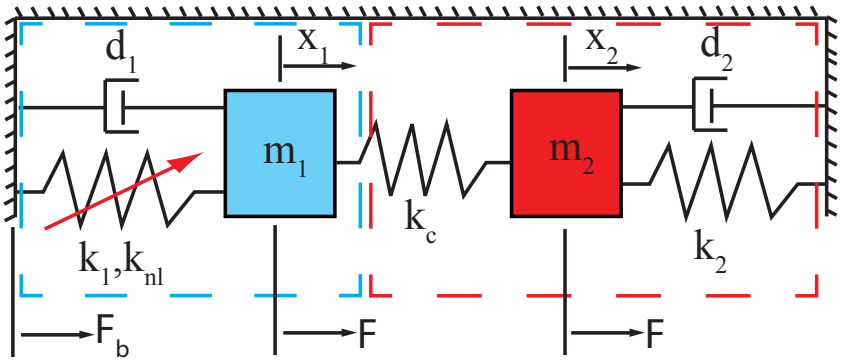

FIGURE 6.1: Block diagram of the system where the blue box contains the energy harvester and the red encloses the excited dynamic magnifier. Each oscillator has on-site stiffness and dissipation terms, as well as a connecting coupling spring. External forcing is provided to each mass by either direct force excitation F or base excitation F_b.)

plug-n-play components are generally preferred over add-ons that require a more significant system reconfiguration.

The auxiliary oscillator indicated by the red box of Fig. 6.1 is a simple linear oscillator, both in its on-site stiffness providing coupling to the base and in its coupling to the energy harvester.

Figure 6.1 illustrates the two types of excitation that will be considered, direct force excitation F applied to each mass and base motion excitation F_b applied through the on-site stiffness and damping terms. The following sections will demonstrate that the systems' behaviors are qualitatively similar for both cases.

6.3 Mathematical Model

This section describes the equations of motion of a given hardening-type energy harvester when an excited dynamic magnifier is added using either direct force or base motion excitation. In each case, the external force is assumed to be single frequency harmonic excitation. After qualitative similarity in the frequency response between the two forcing types is shown in Sec. 6.4.1, the following sections analyze

the direct force excitation case to minimize redundancy.

6.3.1 Direct Force Excitation EOM

In all following analysis, oscillator 1 will always indicate the energy harvester and 2 the excited dynamic magnifier or dummy oscillator. In this section, the energy harvester will have a hardening-type frequency response due to a Duffing style cubic restoring force. The equations of motion for the case where a harmonic excitation force is directly applied to both the magnifier and the harvester is given by

$$\begin{aligned} m_1\ddot{x}_1 + d_1\dot{x}_1 + k_1x_1 + k_{nl}x_1^3 + k_c(x_1 - x_2) &= F\sin\omega t \qquad (6.1)\\ m_2\ddot{x}_2 + d_2\dot{x}_2 + k_2x_2 + k_c(x_2 - x_1) &= F\sin\omega t, \qquad (6.2)\end{aligned}$$

where x_1 and x_2 are the positions, m_1 and m_2 are the masses, k_1 and k_2 are the on-site stiffnesses, k_{nl} is the cubic stiffness of the harvester, k_c is the coupling stiffness, and d_1 and d_2 are the damping coefficients when subjected to forced harmonic excitation of amplitude F and frequency ω.

These equations can be nondimensionalized as

$$\begin{aligned} y_1'' + 2\zeta_1y_1' + y_1 + \beta y_1^3 + \lambda(y_1 - y_2) &= F\sin\Omega\tau \qquad (6.3)\\ \mu y_2'' + 2\zeta_2\sqrt{\mu\eta}y_2' + \eta y_2 + \lambda(y_2 - y_1) &= F\sin\Omega\tau \qquad (6.4)\end{aligned}$$

where

$$\begin{aligned} \mu = \frac{m_2}{m_1}, \eta = \frac{k_2}{k_1}, \beta = \frac{k_{nl}}{k_1}, \lambda = \frac{k_c}{k_1},\\ \Omega = \omega\sqrt{\frac{m_1}{k_1}}, \zeta_i = \frac{d_i}{\sqrt{m_ik_i}} \qquad (6.5)\end{aligned}$$

and y_i is the nondimensionalized absolute position of the i^{th} oscillator.

6.3.2 Base Excitation EOM

For the case of base excitation with prescribed motion

$$z = F_b \sin \omega t, \tag{6.6}$$

each oscillator is driven through the on-site spring and damper. The equations of motion for the case of base excitation are then represented by

$$\begin{aligned} m_1\ddot{x}_1 + d_1(\dot{x_1} - \dot{z}) + k_1(x_1 - z) + k_{nl}(x_1 - z)^3 + k_c(x_1 - x_2) &= 0 \qquad (6.7) \\ m_2\ddot{x}_2 + d_2(\dot{x_2} - \dot{z}) + k_2(x_2 - z) + k_c(x_2 - x_1) &= 0. \qquad (6.8) \end{aligned}$$

By substituting $u_i = x_i - z$ as the nondimensionalized relative position of each oscillator, Eqs. 6.7 and 6.8 are nondimensionalized as

$$\begin{aligned} u_1'' + 2\zeta_1 u_1' + u_1 + \beta u_1^3 + \lambda(u_1 - u_2) &= \Gamma \sin \Omega\tau \qquad (6.9) \\ \mu u_2'' + 2\zeta_2\sqrt{\mu\eta}u_2' + \eta u_2 + \lambda(u_2 - u_1) &= \mu\Gamma \sin \Omega\tau \qquad (6.10) \end{aligned}$$

where the same parameter relationships of Eq. 6.5 have again been substituted and

$$\Gamma = k_1\Omega^2 F, \tag{6.11}$$

As expected, the two nondimensionalized sets of equations are identical except for the forcing term. The base excited case has mass and stiffness dependencies, and due to its frequency squared term, will generally use a much smaller value for the amplitude F_b.

6.4 Analysis

This section will perform analytical analysis and numerical simulations to demonstrate the behavior of the modeled system. First, the coupled system's frequency response will be directly compared to the uncoupled case. The next several subsections will investigate the effects of changing system parameters to provide insight into optimization and design robustness.

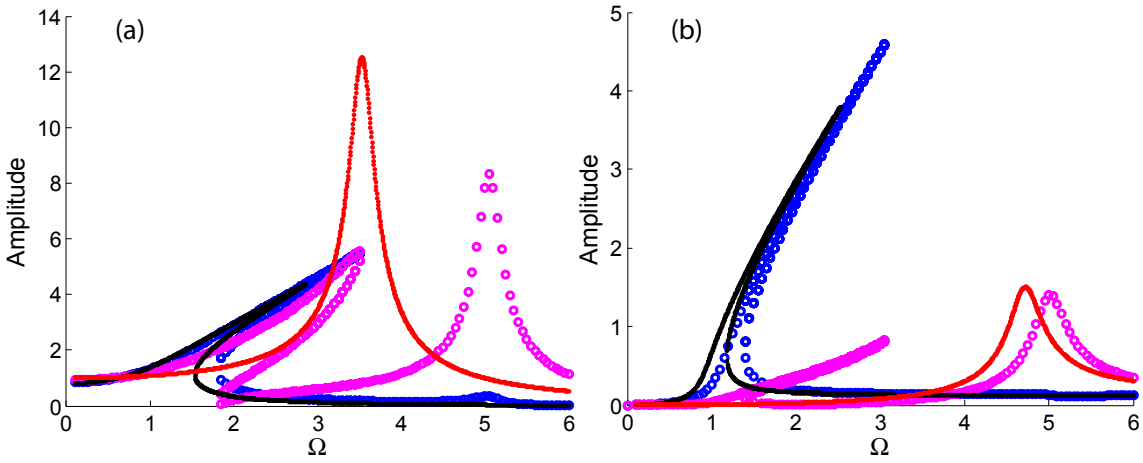

FIGURE 6.2: Comparison between the uncoupled and coupled cases for (a) direct force excitation and (b) base motion excitation. Black and Red (gray) dots represent the approximate analytical solutions for the uncoupled harvester and excited dynamic magnifier. Blue (dark gray) and magenta (light gray) circles represent the numerical solutions of the coupled system. Parameters for (a) are $\mu = 0.08, \eta = 1, \lambda = 1, \beta = 0.5, f = 1$. Parameters for (b) are $\mu = 0.18, \eta = 4.0, \lambda = 0.5, \beta = 0.5, f = 0.12$.

6.4.1 Frequency Response

Before analyzing the coupled system, performance of the original harvester is presented for comparison. The black and red dotted lines of Fig. 6.2(a) show example uncoupled oscillators of Eqs. 6.1 and 6.2 by setting $\lambda = 0$ and solving for a first order approximate analytical solution using the method of harmonic balance. As compared to the linear dummy oscillator, the peak of the hardening oscillator is clearly asymmetrical, with amplitude increasing with frequency. Allowing for the different F and F_b values in each form of excitation, Figs. 6.2(a) and 6.2(b) are qualitatively similar in the behavior of the uncoupled energy harvester.

The coupled case can be approached similarly. Substituting an assumed solution form of

$$y_1 = A_1 \cos \Omega\tau + B_1 \sin \Omega\tau \tag{6.12}$$

$$y_2 = A_2 \cos \Omega\tau + B_2 \sin \Omega\tau \tag{6.13}$$

into Eqs. 6.3 and 6.4 and performing a harmonic balance leads to the following set of equations

$$-\Omega^2 B_1 - 2z\Omega A_1 + B_1 + \frac{3}{4}\beta B_1^3 + \frac{3}{4}\beta A_1^2 B_1 + \lambda(B_1 - B_2) = F \tag{6.14}$$

$$-\Omega^2 A_1 - 2z\Omega B_1 + A_1 + \frac{3}{4}\beta A_1^3 + \frac{3}{4}\beta B_1^2 A_1 + \lambda(A_1 - A_2) = 0 \tag{6.15}$$

$$-\Omega^2 B_2 - 2z\Omega\sqrt{\mu\eta}A_2 + \eta B_2 + \lambda(B_2 - B_1) = F \tag{6.16}$$

$$-\Omega^2 A_2 - 2z\Omega\sqrt{\mu\eta}B_2 + \eta A_2 + \lambda(A_2 - A_1) = 0. \tag{6.17}$$

The closed form solution for this system would be quite long due to the cubic coefficients. However, it can be solved numerically using for example the MATLAB function fsolve, where coexisting solutions are found through iterating over multiple initial guesses.

The blue (dark gray) and magenta (light gray) open circles of Figs. 6.2(a) represent the numerical solutions of Eqs. 6.14-6.17. The coupled solution of Fig. 6.2(b) was similarly solved, substituting Γ and $\mu\Gamma$ for F as appropriate for the case of base excitation. Comparing the two forms of excitation, it is seen that achieving the same harvester response in each case requires different parameters in the excited dynamic magnifier. Figure 6.2(b) illustrates how this increase in mass and changes to stiffness parameters results in significantly lower oscillation amplitude in the dynamic magnifier for the case of base excitation, whereas the two oscillators had similar amplitudes in the direct excitation case.

Fig. 6.3 gives a better view of the performance improvement of the energy harvester with excited dynamic magnifier by comparing the frequency response of the coupled system to the default, uncoupled case. In this example, it can be seen that the coupled response of the energy harvester is largely unchanged at low frequencies, but there are several notable differences as frequency increases. Most importantly, it can be clearly seen that the peak amplitude and frequency have both significantly

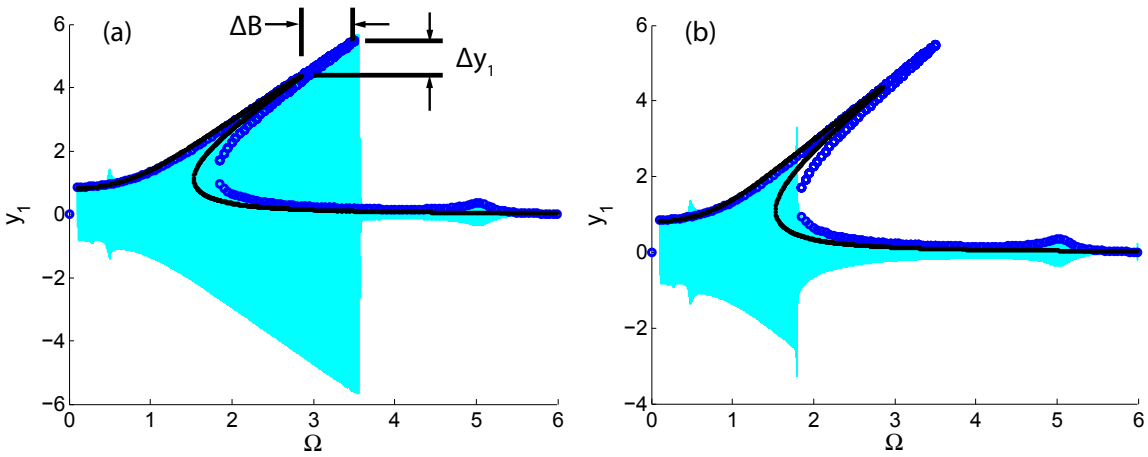

FIGURE 6.3: Time marching frequency (a) upsweep and (b) downsweep for the case of forced harmonic excitation. Cyan (light gray) is the position of the energy harvester during the sweep, Blue (dark gray) circles represent the numerical solution of the coupled system and the black line is the uncoupled approximate analytical solution for comparison. Parameters in both cases are $\mu = 0.08, \eta = 1, \lambda = 1, \beta = 0.5, f = 1$.

increased (by Δy_1 and ΔB respectively) providing greater peak power and a wider usable bandwidth. There is also an upwards shift in the bifurcation point where the high frequency, low amplitude solution begins. The final change is a small second peak corresponding to the coupled natural frequency of the excited magnifier.

Time marching numerical simulations show agreement with the numerically solved solutions. Figure 6.3 also shows an example forward and reverse frequency sweep with the analytical solutions overlaid for reference. Both directions illustrate a different aspect of wider bandwidth of the coupled system over the uncoupled. In the forward sweep, the high amplitude solution is maintained over a much wider frequency range. On the reverse sweep, the jump from low amplitude to the high amplitude solution occurs at a higher frequency, resulting in a greater frequency range spent at the high amplitude solution.

For simplicity, this basic model has omitted the electrical circuit that would necessarily accompany any energy harvester. The kinetic energy of the harvesting

mass will instead be used as a correlated result to give intuition as to the likely effectiveness of the design. Based on the assumed solution form of Eq. 6.12, the maximum kinetic energy of the harvester is represented by

$$T = 0.5\Omega r_1^2, \tag{6.18}$$

for the system normalized to a unit mass and where

$$r_1 = \sqrt{A_1^2 + B_1^2}, \tag{6.19}$$

is the amplitude of the energy harvester. Fig. 6.4 compares the kinetic energy of the original uncoupled energy harvester to the kinetic energy after adding the excited dynamic magnifier for different values of the nonlinear stiffness coefficient β. The dramatic increase in energy results from the combination of both increased amplitude and also the increased velocity due to the peak occurring at a higher frequency.

6.4.2 Stability

Stability analysis of the coupled system can be performed by allowing the coefficients of Eq. 6.12 to be time varying, for a solution of the form

$$y_i = A_i(\tau)\cos\Omega\tau + B_i(\tau)\sin\Omega\tau. \tag{6.20}$$

By assuming that these coefficients are slowly time varying such that $\ddot{A}_i = \ddot{B}_i = 0$, substituting this modified solution form into Eqs. 6.3 and 6.4 results in the following

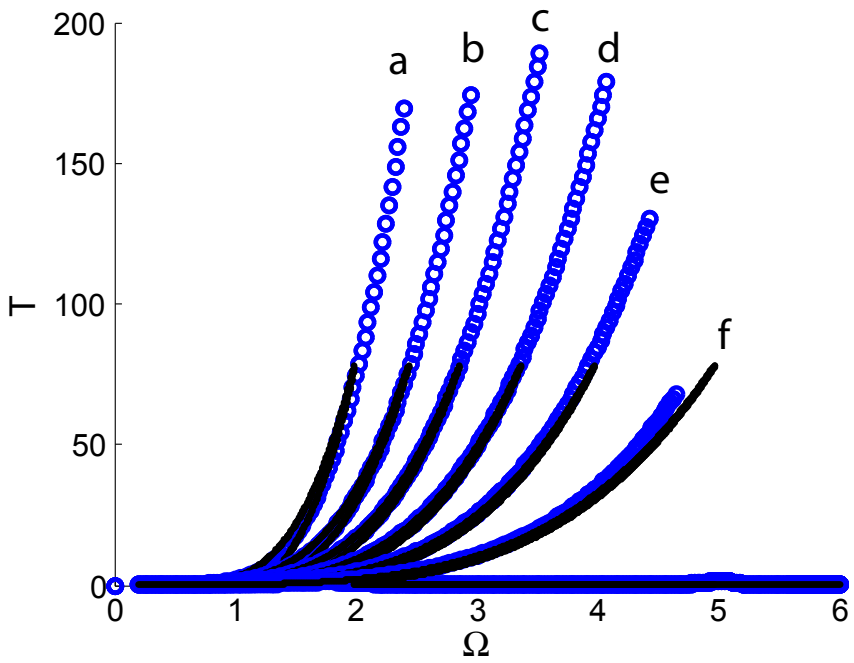

FIGURE 6.4: Kinetic energy of the uncoupled energy harvester (black points) and the energy harvester with excited dynamic magnifier (blue circles) for nonlinear coefficient $\beta =$ (a) 0.1, (b) 0.25, (c) 0.5, (d) 1.0, (d) 2.0, (e) 5.0. Parameters in each case are $\mu = 0.08, \eta = 1, \lambda = 1, F = 1$ with direct excitation.

system of equations.

$$\begin{bmatrix} 2\Omega & -2z & 0 & 0 \\ -2z & -2\Omega & 0 & 0 \\ 0 & 0 & 2\mu\Omega & -2z\sqrt{\mu\eta} \\ 0 & 0 & -2z\sqrt{\mu\eta} & -2\mu\Omega \end{bmatrix} \begin{bmatrix} A_1' \\ B_1' \\ A_2' \\ B_2' \end{bmatrix} =$$

$$\begin{bmatrix} -\Omega^2 B_1 - 2z\Omega A_1 + B_1 + \frac{3}{4}\beta B_1^3 + \frac{3}{4}\beta A_1^2 B_1 + \lambda(B_1 - B_2) - F \\ -\Omega^2 A_1 - 2z\Omega B_1 + A_1 + \frac{3}{4}\beta A_1^3 + \frac{3}{4}\beta B_1^2 A_1 + \lambda(A_1 - A_2) \\ -\Omega^2 B_2 - 2z\Omega\sqrt{\mu\eta}A_2 + \eta B_2 + \lambda(B_2 - B_1) - F \\ -\Omega^2 A_2 - 2z\Omega\sqrt{\mu\eta}B_2 + \eta A_2 + \lambda(A_2 - A_1) \end{bmatrix} \tag{6.21}$$

The Jacobian matrix is then the inverse of the left side matrix multiplied by

$$J = \begin{bmatrix} -2z\Omega + \frac{3}{2}\beta A_1 B_1 & \sigma_1 & 0 & -\lambda \\ \sigma_2 & 2z\Omega + \frac{3}{2}\beta A_1 B_1 & -\lambda & 0 \\ 0 & -\lambda & -2z\Omega\sqrt{\mu\eta} & -\Omega^2\mu + \eta + \lambda \\ -\lambda & 0 & -\Omega^2\mu + \eta + \lambda & 2z\Omega\sqrt{\mu\eta} \end{bmatrix} \tag{6.22}$$

which is the system of partial derivatives of the right side of Eq. 6.21 and where

$$\sigma_1 = -\Omega^2 + 1 + \frac{9}{4}\beta B_1^2 + \frac{3}{4}\beta A_1^2 + \lambda \tag{6.23}$$

$$\sigma_2 = -\Omega^2 + 1 + \frac{9}{4}\beta A_1^2 + \frac{3}{4}\beta B_1^2 + \lambda. \tag{6.24}$$

Stable solutions are then expected when the eigenvalues of the Jacobian matrix have negative real components when evaluated at the fixed points. Figures 6.7(b)-(c) show example cases where the hardening system results in an expected pair of coexisting solutions, one at high and the other at low amplitude (large dots), with an unstable solution in between (small dots).

6.4.3 Power Per Unit Mass

The preceding section analyzed the system under the assumption that a given energy harvester would be supplemented by the addition of a dynamic magnifier. This would often be the implementation method used, but there may also be cases where overall mass is sought to be minimized or maintained, and the additional mass for the magnifier must be subtracted from the harvester. Figure 6.5 shows example cases where the peak amplitude and frequency bandwidth can still be increased over the uncoupled case, even when total mass is maintained constant.

The blue circles and green squares of Fig. 6.5 show that the excited dynamic magnifier can increase both amplitude and kinetic energy over the uncoupled harvester when m_2 is sufficiently small. Since the cyan diamond line has a peak just

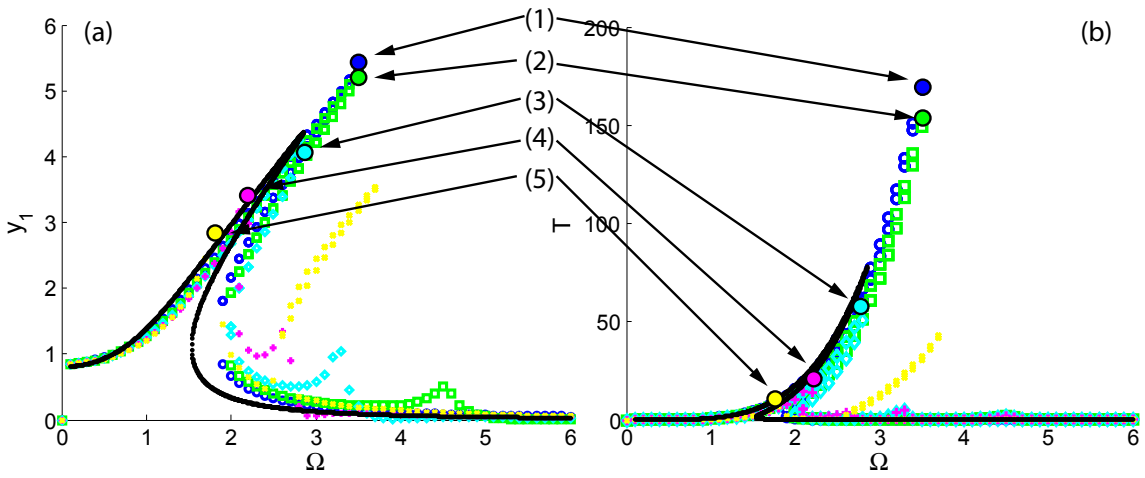

FIGURE 6.5: Numerical (a) amplitude and (b) maximum kinetic energy of the energy harvester with excited dynamic magnifier with overall mass conserved as compared to the uncoupled case (black line). Harvester mass is (1) 0.98 (2) 0.90 (3) 0.80 (4) 0.65 (5) 0.50, with $m_2 = 1 - m_1$. Large circles indicate the peak of each curve. Parameters in both cases are $\eta = 1, \lambda = 1, \beta = 0.5, f = 1$.

below the uncoupled case, it can be inferred that the limit in this example has m_2 slightly less than 0.2 in order to achieve superior power per unit mass as compared to the uncoupled case.

Line (5) of Fig. 6.5, the yellow x's, show the case where both the harvester and the magnifier have the same mass. This case is qualitatively similar to previously studied harvester arrays and provides a sharp contrast in behavior to the cases with a much smaller second mass. It's second peak is of comparable amplitude to the primary peak, and they have a central valley between them. In some sense, this could be considered to have a widened bandwidth over the uncoupled case, but when compared to the low second mass cases as in for example Line (1) of Fig. 6.5, superior performance in amplitude, bandwidth and kinetic energy is clearly evident in Line (1) with its larger single peak, without the central valley.

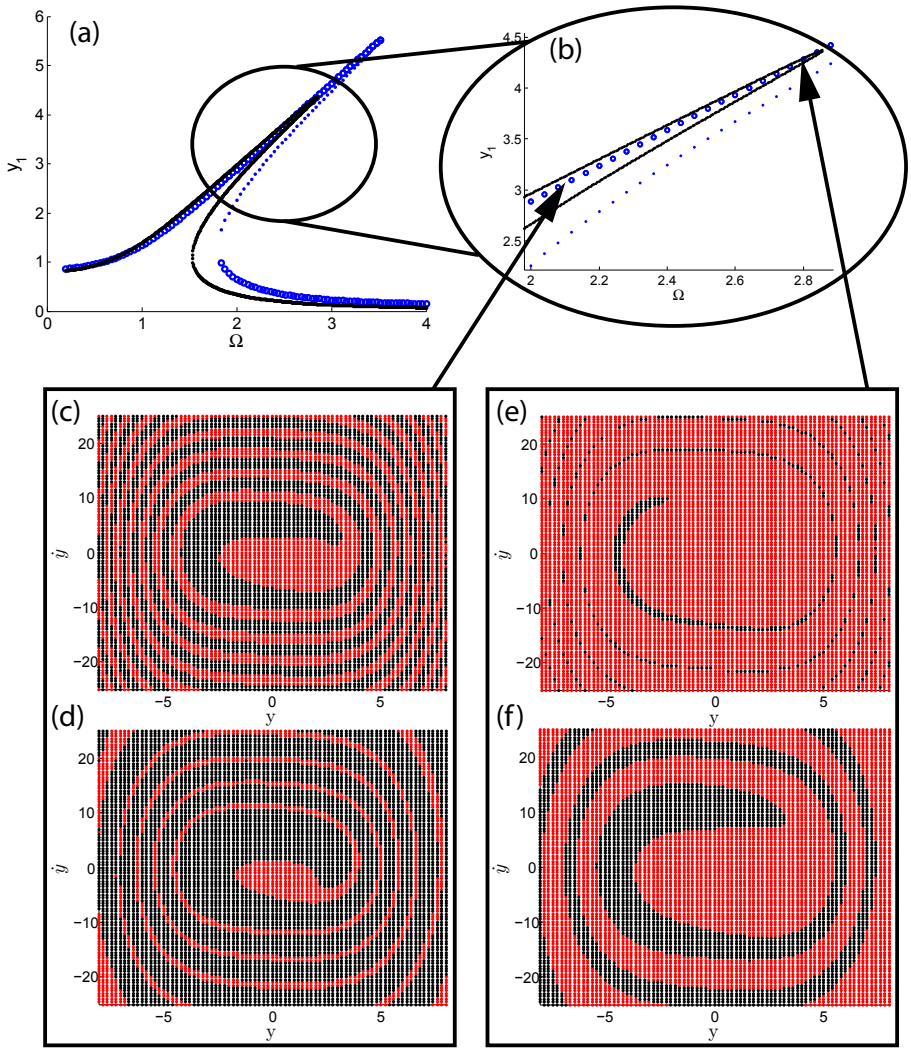

FIGURE 6.6: (a) Frequency response for an uncoupled nonlinear harvester (black dots) and harvester with excited dynamic magnifier (blue open circles and dots) for $\mu = 0.08, \beta = 0.5, \eta = 1.0, \lambda = 1.0, F = 1.0$ with forced harmonic excitation. (b) Zoomed in portion of the response to illustrate the much larger separation distance between the stable and unstable solutions near the peak after adding the magnifier. Basin of attraction diagrams show high amplitude solution (black) and low amplitude solutions (red/gray) at (c)-(d) Ω=2.1 and (e)-(f) Ω=2.8. The lower two plots (d) and (f) are the case with added excited dynamic magnifier and show a much greater range of values leading to the high amplitude solution as compared to the uncoupled case (c) and (e).

6.4.4 Basins of Attraction

A primary advantage of a hardening energy harvester over a similar linear device is the wider bandwidth due to its slanted peak. However, a significant drawback is that in this region of coexisting solutions, it is not always easy to obtain the desired high amplitude solution. Figures 6.6(a) and (b) provide insight as to why this is the case. Near the peak of hardening oscillator's frequency response, a stable and unstable solution are extremely close together. Figures 6.6(e) shows that just below the peak, at Ω=2.8, there are very few initial conditions that result in the high amplitude solution. Even in laboratory conditions, this peak can be very difficult to obtain experimentally. In the field, it would be extremely unlikely to obtain it organically through chance environmental input. Even looking lower down the peak, in this example at Ω=2.1, only roughly half of the initial conditions analyzed result in the high amplitude peak.

In addition to the higher peak and increased bandwidth that were shown in the previous section, Figures 6.6(d) and (f) show that a potentially more important benefit of adding an excited dynamic magnifier to a hardening-type harvester is that it makes these peak values easier to obtain. The basins of attraction for the dynamically magnified system show a significantly greater space of initial conditions that result in the high amplitude solutions over the frequency range of the uncoupled peak. This provides an important practical benefit in allowing an existing harvester to be more likely to achieve its harvesting capacity.

Multi-Frequency Behavior

As with most systems, the excited dynamic magnifier does have potential drawbacks and there are certain physical parameters that, if mistuned, can severely impair harvester performance. One of these is a resonance in the coupling spring that is a function of the coupling coefficient and the mass ratio. When this resonance aligns

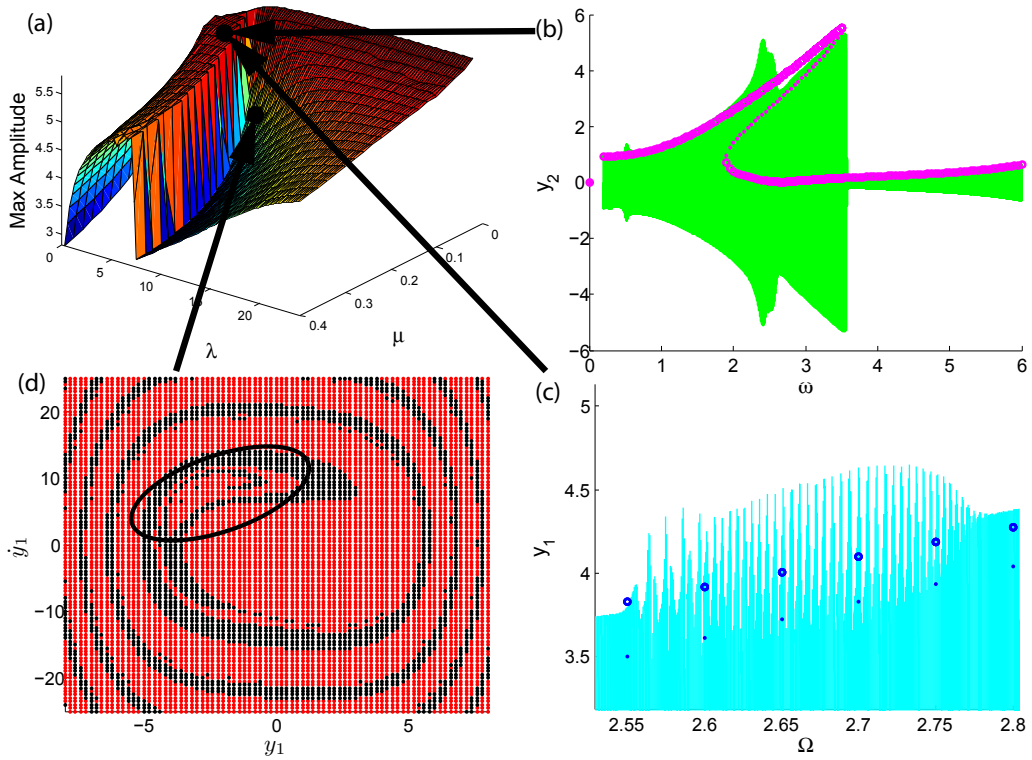

FIGURE 6.7: A series of frequency sweeps were performed with high coupling stiffness coefficients. (a) The energy harvester's maximum observed amplitude contains a large, unexpected trough. (b) Forward quasistatic sweep of the excited dynamic magnifier with $\mu = 0.08$ and $\lambda = 3.4$ shows high amplitude, multi-frequency behavior between $\Omega = 2.5$ through 2.8 which is not captured in the first order analytical solution. (c) The energy harvester also shows significant multi-frequency behavior, with amplitude oscillations on the order of the separation distance between stable (open circles) and unstable (dots) solutions. (d) Basin of attraction diagram at $\mu = 0.08$ and $\lambda = 3.5$ shows that a region of inital conditions (circled) that led to the high amplitude solution with lower coupling strength, now result in well-escape and settle into the low amplitude solution due to this higher order behavior.

near the peak of the energy harvester, the associated multi-frequency behavior can result in well-escape and make it more difficult to achieve the high amplitude solution.

This phenomenon is demonstrated in Figs. 6.7(a) and (b) which illustrate that there exist regions in the parameter space where the first order solution does not seem to adequately describe the coupled system's behavior near the peak. Specifically, higher order oscillations can be seen to destabilize the harvester in the frequency

range of interest. Though the first order approximate analytical solution predicts a stable higher peak, Figs. 6.7(b) and (c) clearly show that multi-frequency behavior is observed in both the magnifier and harvester, which can predictably perturb the energy harvester out of the high amplitude solution. A higher order model would be required to more accurately describe system response for masses and coupling coefficients falling in this large valley. It should be noted that the peaks in Figs. 6.7(b) and (c) are stable and can be reached with carefully selected initial conditions, however as shown in Figs. 6.7(d), this higher order behavior has significantly reduced the space of initial conditions that will settle into the high amplitude solution.

Multi-frequency behavior with high coupling near the peak is more significant than when it appears at a lower frequency with low coupling because of the proximity of the unstable solution. At $\Omega < 2.0$ for example, there is only 1 system solution, so this behavior has only a minor effect on the system. Near peak amplitude, however, there are 2 stable solutions separated by 1 unstable solution. Since the unstable solution is so close to the stable peak solution, this multi-frequency behavior can be sufficiently disruptive as to result in potential well escape, to the low amplitude solution. This phenomena must be taken into consideration during any design process since the behavior in this region of parameter space is likely undesirable. Two design choices that can help avoid this region are to decrease the coupling coefficient and increase the mass ratio, which both act to decrease the resonant frequency in the coupling spring, ideally to a frequency with only a single stable solution. However, as will be shown in the next section, these two design choices run contrary to kinetic energy optimization over those parameters.

6.4.5 Optimization

Figures 6.4 and 6.8 both provide insight into parameter relationships that would be used for system optimization. Figure 6.4 iterates over several values for the nonlinear

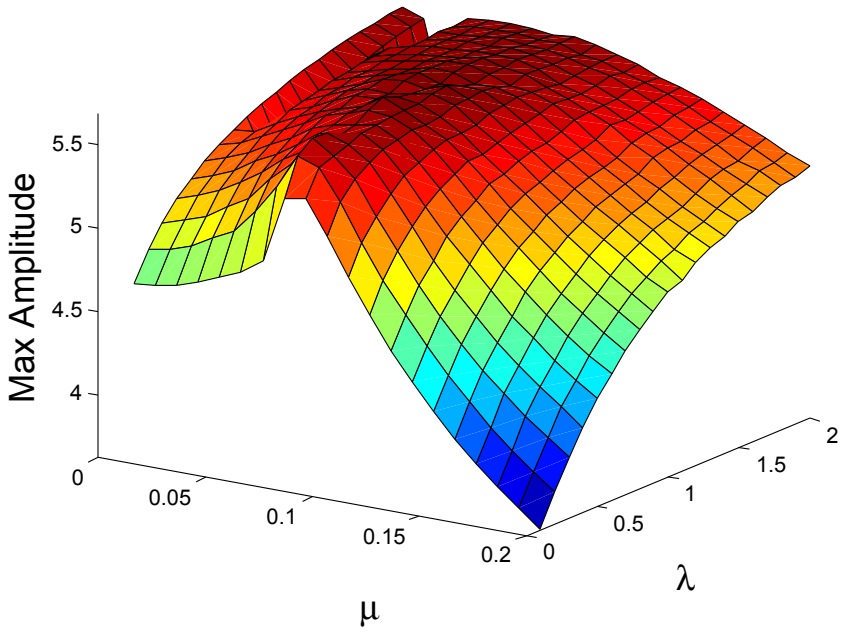

FIGURE 6.8: Maximum amplitude of the energy harvester over a range of mass ratios and coupling stiffnesses for the case of forced harmonic excitation. For low stiffnesses, the maximum harvester amplitude is seen near $\mu = 0.1$. The optimal mass ratio slowly decreases as coupling stiffness increases. Parameters used were $\beta = 0.5, \eta = 1, F = 1$.

stiffness coefficient of the energy harvester. In the uncoupled case, it can be seen that changing this parameter does not have an effect on the system's maximum kinetic energy. Lower amplitude of oscillations at higher frequencies is compensated for by increased velocity, maintaining the same kinetic energy. This relationship does not hold in the coupled case where it can be clearly seen that in this example, there is a peak kinetic energy level achievable using β of approximately 0.5. This value is a function of the natural frequency of the dynamic magnifier. Recall the location of the peak of the uncoupled dummy oscillator in Fig. 6.2(a). Maximum kinetic energy in the coupled harvester occurs when this peak is tuned slightly to the right of the uncoupled harvester's peak. This could be achieved as in Fig. 6.4 through changing the level of nonlinearity in the harvester, or by instead tuning the on-site stiffness or mass of the magnifier.

Figure 6.8 analyzes the relationship between the mass ratio and the coupling stiffness coefficient. For low coupling values, increasing the coupling coefficient λ generally increases the maximum harvester amplitude. It can also be seen that for these low levels of coupling, there is an optimal mass ratio. In this example, the maximum occurs near $\mu = 0.1$ for very low coupling and slightly decreases as coupling strength increases. However, it should be again noted that though the expected performance based on the first order analytical solution would be optimized simply by maximizing the coupling strength and minimizing the mass ratio, the real system is not so straightforward. Figure 6.6(a) demonstrated that there is a limit beyond which multi-frequency behavior disrupts the harvester near the peak, making the high amplitude solution more difficult to obtain. In practice, preferred system behavior will typically be achieved with the maximum coupling strength and associated optimal mass ratio, that still result in a coupling resonance at a sufficiently low frequency as to occur in the single stable solution portion of the harvester's frequency response curve.

6.5 Conclusion

Improving the performance of existing energy harvesting devices is an ongoing research effort in the engineering community. Three performance criteria often referenced are maximum power (or kinetic energy), power per unit mass and bandwidth. The model presented here for a hardening-type energy harvester with excited dynamic magnifier has shown improvements in all three categories over the comparable standalone harvester. It was demonstrated that the addition of an excited dynamic magnifier can achieve nearly identical amplitudes over the frequency range of the uncoupled harvester's peak, and the excited dynamic magnifier acts to extend the response to a higher peak amplitude at a higher frequency, thereby also resulting in an increase in maximum kinetic energy.

The system also avoids several drawbacks of related designs. This design does not utilize dual peaks which contain a lower power central valley like some previous dynamic magnifier and harvester array designs, and also does not require additional expensive components like the multiple energy harvesters used in harvester arrays.

The most important benefit of the excited dynamic magnifier may be the increased likelihood in multistable frequency ranges of obtaining the high amplitude solution. This greater range of initial conditions leading to the high amplitude solution makes use of the nonlinear harvester much more practical. Care must be taken in tuning however, since first-order analytical optimization of certain parameters (specifically the coupling stiffness and mass ratio) can result in undesired multi-frequency behavior, counteracting these benefits.

A proposed use for this technology would be for environments with varying single frequency excitation where a tuned hardening-type energy harvester is already in use. Addition of an excited dynamic magnifier allows high amplitude solutions across it's peak frequency range to be more easily achieved without retuning, while also extending the high amplitude solution over a greater frequency range, allowing the energy harvester to expand is operating range over a wider bandwidth.

7

Summary, Conclusions, and Future Directions

7.1 Summary and Conclusions

The second chapter provided two significant advances to the field of wave propagation for analyzing nonlinear chains. The first was providing a means to rearrange the equations of motion to isolate system parameters in order to utilize standard uncertainty analysis techniques. Using this method, a system designer can readily compare the robustness of a given model to different types of uncertainty in each physical parameter. The second contribution is in qualitative analysis of the effects of increased excitation amplitude. Previous works had already demonstrated that standard wave propagation analysis techniques could not be applied to nonlinear systems, however this chapter demonstrates the mechanism by which the solutions break down as amplitudes increase. It was also shown that these effects are much stronger at high frequency than low, and that bandgap regions are less prone to chaos and sub/super harmonics than propagation zones.

An experimental testbed for studying wave propagation was designed and simulated in the fourth chapter of this dissertation. It can be extremely difficult to

achieve wave propagation in a general chain of mechanical oscillators, with the primary challenge being overcoming system damping. The proposed testbed is able to minimize damping through the use of a pendulum design with low friction ball bearings, a long pendulum arm, and added mass. Another unique feature of this design is that the chain of pendulums are aligned axially, so that the direction of motion of each oscillator is out of plane of the direction of wave propagation. This differs from most granular chain designs, and provides increased safety in that there is no risk of collision between adjacent oscillators for any oscillation amplitude. This out of plane motion also makes it easier to provide rigid, permanent, external controls to individual oscillators.

In the field of wave propagation, the most significant contribution of this dissertation was described analytically in Chapter 3 and experimentally in Chapter 5. Most research in this area has focused on active control of bandgap regions. The most popular methods utilize tuning of design parameters or component replacement in order to change the system's behavior. These chapters demonstrate a supplemental technique for passive bandgap reconfiguration. By imposing an asymmetrical restoring force on a single oscillator in each unit cell, it is shown that each potential well has a unique set of wave propagation characteristics. The system can be tuned so that a propagation zone in one well corresponds to a bandgap in the other, leading to a possible safety feature of amplitude dependent filtering, similar to a mechanical circuit breaker. Low amplitude vibrations are able to pass through the chain, but if external excitation exceeds some threshold, well escape occurs and the system 'trips', and attenuates further vibration.

The final chapter investigated a new method for improving the performance of a nonlinear energy harvester by adding an excited dynamic magnifier. Inspired by standard dynamic magnifiers and harvester arrays, this model predicts benefits seen in both precursor designs, but without the primary drawbacks of either. After adding

the excited dynamic magnifier, the energy harvester should have a higher peak amplitude response and a wider effective bandwidth, and unlike the previous designs, it should also increase power efficiency and should not significantly increase overall system cost. Most importantly, it improves on the primary limitation of hardening-type harvesters by significantly increasing the range of initial conditions that lead to the high amplitude solution.

7.2 Future Directions for Research

Many sections of this dissertation have analyzed model systems or designed experimental testbeds. There should be opportunities in the future to leverage this work as a basis for experimental work. The chain of pendulums is an excellent resource for studies in mechanical wave propagation and could also be used for the reverse problem of dissipation, for example in the field of discrete breathers.

7.2.1 Wave Propagation

There are two areas that would naturally follow the wave propagation research performed in this dissertation. The first is in analyzing multistable systems with greater than two equilibria. The theoretical and experimental work performed here focused on strictly bistable systems. Even the longer chains were only stable when all unit cells were in the same potential well. A future project should expand this analysis to instead consider the case of hybrid equilibria in which unit cells can be in opposite potential wells. Preliminary theoretical analysis could be performed to provide insight to the expected behavior in the hybrid equilibria which could then be verified experimentally.

The primary shortcoming of the design for passive bandgap reconfiguration proposed in Chapters 4 and 6 is that there is currently no mechanism for reset. Once high amplitude excitation causes well escape and the system attenuates signals, the

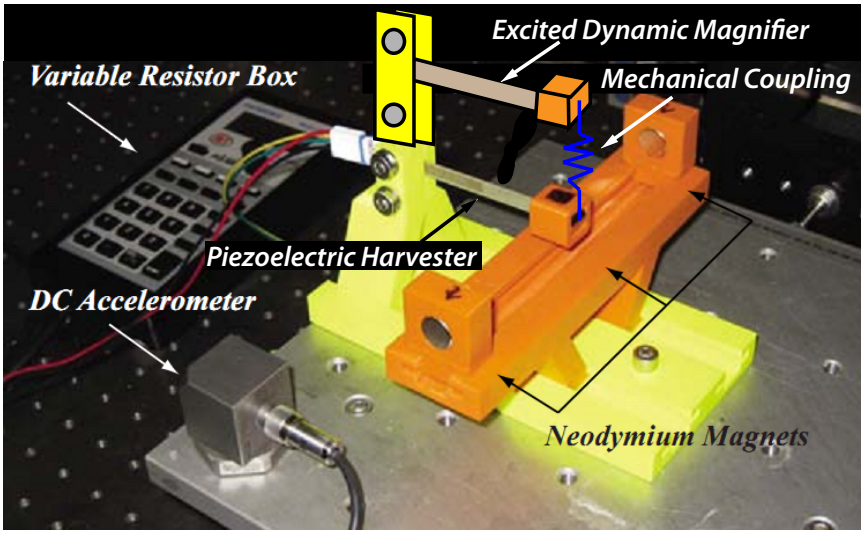

FIGURE 7.1: Drawing of a possible example system, modified from Ref. [1]. Two clamped free beams are excited by the same base excitation. The lower beam has a magnetic tip mass that creates a hardening stiffness. The upper beam has linear stiffness. The two tip masses are attached via a linear spring.

system will not revert to its propagating state after excitation later decreases. Collaboration with David Arnold's research group at the University of Florida may allow additional investigation into this topic. They are currently micro-fabricating chains of cantilevered beams with magnetic masses in order to replicate wave propagation behaviors similar to the systems in this document. An important feature of their model is that it may be possible to repolarize their magnets. Through the repolarization process it may be possible to create the functional equivalent of resetting the system from the deep to shallow potential well through periodic depolarization to a monostable condition and repolarization in such a manner as to ensure the oscillators begin in the shallow potential well.

7.2.2 Excited Dynamic Magnifier

Figure 7.1 shows a sample drawing of a system configuration that would be expected to have the same performance of the modeled system from Chapter 6, using the nonlinear energy harvester of Ref. [1] as a basis for comparison. The lower cantilever

beam represents a piezoelectric energy harvester with magnetic tip mass. Magnets on either side of the beam create a hardening frequency response in the harvester. The second beam would be an inexpensive dummy oscillator. Both are connected to the same base, and also connected to each other through a linear spring at the center of their tip masses. One difference between this proposed experimental design and the block diagram model of the previous chapter is that even with a linear coupling spring, this orientation would impose geometric nonlinearities in the coupling stiffness, however this is not expected to qualitatively impact performance.

The primary design challenge would be to determine the best means of attaching a spring or elastic band to each tip mass in order to allow parameter flexibility. It should also be noted that care should be taken in construction to minimize any possible torque on the beams induced by the coupling springs. Attaching the coupling spring to the center of the tip mass should minimize this effect.

Using a previously studied harvester design as a basis would be simpler from a design perspective because many of the components are already built and tested. More importantly, the direct comparison to published results of the standalone harvester would provide additional credibility to the claimed performance improvements predicted by the simulations.

Bibliography

[1] Stanton, S. C., MgGehee, C. C., and Mann, B. P., 2009. "Reversible hysteresis for broadband magnetopiezoelastic energy harvesting". *Applied Physics Letters,* **95**, p. 174103.

[2] Nesterenko, V. F., 1983. "Propagation of nonlinear compression pulses in granular media". *Journal of Applied Mechanics and Technical Physics,* **24**(5), pp. 733–743.

[3] Coste, C., Falcon, E., and Fauvre, S., 1997. "Solitary waves in a chain of beads under hertz contact". *Physical Review E,* **56**(5), November, pp. 6104–6117.

[4] MacKay, R. S., 1999. "Solitary waves in a chain of beads under hertz contact". *Physics Letters A,* **251**, January, pp. 191–192.

[5] Yang, X.-S., Wang, B.-Z., and Zhang, Y., 2004. "Pattern-reconfigurable quasi-yagi microstrip antenna using a photonic band gap structure". *Microwave and Optical Technology Letters,* **42**(4), August, pp. 296–297.

[6] Friesecke, G., and Wattis, J. A. D., 1994. "Existence theorem for solitary waves on lattices". *Communications in Mathematical Physics,* **161**(2), pp. 391–418.

[7] Lazaridi, A. N., and Nesterenko, V. F., 1985. "Observation of a new type of solitary waves in a one-dimensional granular medium". *Journal of Applied Mechanics and Technical Physics,* **26**, pp. 405–408.

[8] Mead, D. J., 1996. "Wave propagation in continuous periodic structures: research contributions from Southampton". *Journal of Sound and Vibration,* **190**(3), pp. 495–524.

[9] Nesterenko, V. F., 2000. *Dynamics of Heterogeneous Materials.* Springer.

[10] Kushwaha, M. S., Halevi, P., Dobrzynski, L., and Djafari-Rouhani, B., 1993. "Acoustic band structure of periodic elastic composites". *Physical Review Letters,* **71**(13), September, pp. 2022–2025.

[11] Kushwaha, M. S., Halevi, P., Martinez, G., Dobrzynski, L., and Djafari-Rouhani, B., 1994. "Theory of acoustic band structure of periodic elastic composites". *Physical Review B,* **49**(49), January, pp. 2313–2322.

[12] Brillouin, L., 1953. *Wave Propagation in Periodic Structures.* Dover.

[13] Martinsson, P. G., and Movchan, A. B., 2003. "Vibrations of lattice structures and phononic band gaps". *The Quarterly Journal of Mechanics and Applied Mathematics,* **56**, pp. 45–54.

[14] Szelengowicz, I., Hasan, M. A., Starosvetsky, Y., Vakakis, A., and Daraio, C., 2013. "Energy equipartition in two-dimensional granular systems with spherical intruders". *Physical Review E,* **87**(032204), pp. 032204–1–032204–5.

[15] Kevrekidis, P. G., Vainchtein, A., Garcia, M. S., and Daraio, C., 2013. "Interaction of traveling waves with mass-with-mass defects within a hertzian chain". *Physical Review E,* **87**(042911), pp. 042911–1–042911–13.

[16] Jayaprakash, K. R., Starosvetsky, Y., Vakakis, A. F., Peeters, M., and Kerschen, G., 2011. "Nonlinear normal modes and band zones in granular chains with no pre-compression". *Nonlinear Dynamics,* **63**, pp. 359–385.

[17] Jensen, J. S., 2003. "Phononic band gaps and vibrations in one- and two-dimensional mass-spring structures". *Journal of Sound and Vibration,* **266**, pp. 1053–1078.

[18] Farzbod, F., and Leamy, M. J., 2011. "Analysis of Bloch's method and the propagation technique in periodic structures". *Journal of Vibration and Acoustics,* **133**(031010), June, pp. 031010–1–031010–7.

[19] Vakakis, A. F., and King, M. E., 1995. "Nonlinear wave transmission in a monocoupled elastic periodic system". *Journal of Acoustic society of America,* **98**(3), September, pp. 1534–1546.

[20] Soljacic, M., and Joannopoulos, J. D., 2004. "Enhancement of nonlinear effects using photonic crystals". *Nature Materials,* **3**, April, pp. 211–219.

[21] Daraio, C., Nesterenko, V. F., Herbold, E. B., and Jinn, S., 2006. "Energy trapping and shock disintegration in a composite granular medium". *Physical Review Letters,* **96**(058002), February, pp. 058002–1–058002–4.

[22] Zhou, X.-Z., Wang, Y.-S., and Zhang, C., 2009. "Effects of material parameters on elastic band gaps of two-dimensional solid phononic crystals". *Journal of Applied Physics,* **106**, pp. 014903–1–014903–11.

[23] Herbold, E. B., Kim, J., Nesterenko, V. F., Wang, S. Y., and Daraio, C., 2009. "Pulse propagation in a linear and nonlinear diatomic periodic chain: effects of acoustic frequency band-gap". *Acta Mechanica,* **205**, pp. 85–103.

[24] Zhou, W., Mackie, D. M., Taysing-Lara, M., Dang, G., Newman, P. G., and Svensson, S., 2006. "Novel reconfigurable semiconductor photonic crystal-mems device". *Solid-State Electronics,* **50**(6), June, pp. 908–913.

[25] Edalati, A., Boutayeb, H., and Denidni, T. A., 2007. "Band structure analysis of reconfigurable metallic crystals: Effect of active elements". *Journal of Electromagnetic Waves and Applications,* **21**(15), pp. 2421–2430.

[26] Pennec, Y., Djafari-Rouhani, B., Vasseur, J. O., Khelif, A., and Deymier, P. A., 2004. "Tunable filtering and demultiplexing in phononic crystals with hollow cylinders". *Physical Review E,* **69**, p. 046608.

[27] Daraio, C., Nesterenko, V. F., Herbold, E. B., and Jin, S., 2006. "Tunability of solitary wave properties in one-dimensional strongly nonlinear phononic crystals". *Physical Review E,* **73**(026610), pp. 026610–1–026610–10.

[28] Daqaq, M. F., Masana, R., Erturk, A., and Quinn, D. D., 2014. "On the role of nonlinearities in vibratory energy harvesting: A critical review and discussion". *Applied Mechanics Reviews,* **66**, July, p. 040801.

[29] Mann, B. P., and Owens, B. A., 2010. "Investigations of a nonlinear energy harvester with a bistable potential well". *Journal of Sound and Vibration,* **329**, pp. 1215–1226.

[30] Stanton, S. C., MgGehee, C. C., and Mann, B. P., 2010. "Nonlinear dynamics for broadband energy harvesting: Investigation of a bistable piezoelectric inertial generator". *Physica D,* **239**, pp. 640–653.

[31] Vocca, H., Neri, I., Travasso, F., and Gammaitoni, L., 2012. "Kinetic energy harvesting with bistable oscillators". *Applied Energy,* **97**, pp. 771–776.

[32] Mann, B. P., and Sims, N. D., 2009. "Energy harvesting from the nonlinear oscillations of magnetic levitation". *Journal of Sound and Vibration,* **319**, pp. 515–530.

[33] Barton, D. A. W., Burrow, S. G., and Clare, L. R., 2010. "Energy harvesting from vibrations with a nonlinear oscillator". *Journal of Vibration and Acoustics,* **132**(2), March, p. 021009.

[34] Ramlan, R., Brennan, M. J., Mace, B. R., and Kovacic, I., 2010. "Potential benefits of a non-linear stiffness in an energy harvesting device". *Nonlinear Dynamics,* **59**(4), pp. 545–558.

[35] Liu, J.-Q., Fang, H.-B., Xu, Z.-Y., Mao, X.-H., Shen, X.-C., Chen, D., Liao, H., and Cai, B.-C., 2008. "A mems-based piezoelectric power generator array for vibration energy harvesting". *Microelectronics Journal,* **39**, pp. 802–806.

[36] Xue, H., Hu, Y., and Wang, Q.-M., 2008. "Broadband piezoelectric energy harvesting devices using multiple bimorphs with different operating frequencies". *IEEE Transactions on Ultrasonics, Ferroelectrics and Frequency Control,* **55**(9), September, pp. 2104–2108.

[37] Xiao, Z., qing Yang, T., Dong, Y., and cai Wang, X., 2014. "Energy harvester array using piezoelectric circular diaphragm for broadband vibration". *Applied Physics Letters,* **104**, p. 223904.

[38] Aldraihem, O., and Baz, A., 2011. "Energy harvester with a dynamic magnifier". *Journal of Intelligent Material Systems and Structures,* **22**, pp. 521–530.

[39] Zhou, W., Penamalli, G. R., and Zuo, L., 2012. "An efficient vibration energy harvester with a multi-mode dynamic magnifier". *Smart Materials and Structures,* **21**, p. 015014.

[40] Aladwani, A., Arafa, M., Aldraihem, O., and Baz, A., 2012. "Cantilevered piezoelectric energy harvester with a dynamic magnifier". *Journal of Vibration and Acoustics,* **134**, June, p. 031004.

[41] Wu, Z., Harne, R. L., and Wang, K. W., 2014. "Energy harvester synthesis via coupled linear-bistable system with multistable dynamics". *Journal of Applied Mechanics,* **81**, June, p. 061005.

[42] Cornwell, P. J., Goethal, J., Kowko, J., and Damianakis, M., 2005. "Enhancing power harvesting using a tuned auxiliary structure". *Journal of Intelligent Material Systems and Structures,* **16**, pp. 825–834.

[43] Tang, L., and Yang, Y., 2012. "A multiple-degree-of-freedom piezoelectric energy harvesting model". *Journal of Intelligent Material Systems and Structures,* **23**(14), pp. 1631–1647.

[44] Gibert, J. M., Alazemi, S., Paige, F. E., and Daqaq, M. F., 2012. "New insights into piezoelectric energy harvesting using a dynamic magnifier". In Proceedings of the ASME 2012 Conference on Smart Materials, Adaptive Structures, and Intelligent Systems, pp. 1–15. Stone Mountain, GA.

[45] Yang, Z., and Yang, J., 2009. "Connected vibrating piezoelectric bimorph beams as a wide-band piezoelectric power harvester". *Journal of Intelligent Material Systems and Structures,* **20**(5), pp. 569–574.

[46] Kim, I.-H., Jung, H.-J., Lee, B. M., and Jang, S.-J., 2011. "Broadband energy-harvesting using a two degree-of-freedom vibrating body". *Applied Physics Letters,* **98**, p. 214102.

[47] Peng, X., Wen, Y., Li, P., Yang, A., and Bai, X., 2013. "A wideband acoustic energy harvester using a three degree-of-freedom architecture". *Applied Physics Letters,* **103**, p. 164106.

[48] Moleron, M., Leonard, A., and Daraio, C., 2014. "Solitary waves in a chain of repelling magnets". *Journal of Applied Physics,* **115**, p. 184901.

[49] Doney, R. L., and Sen, S., 2005. "Impulse absorption by tapered horizontal alignments of elastic spheres". *Physical Review E,* **72**(041304), pp. 041304–1–041304–11.

[50] Doney, R., and Sen, S., 2006. "Decorated, tapered, and highly nonlinear granular chain". *Physical Review Letters,* **97**(155502), October, pp. 155502–1–155502–4.

[51] Ponson, L., Boechler, N., Lai, Y. M., Porter, M. A., Kevrekidis, P. G., and Daraio, C., 2010. "Nonlinear waves in disordered diatomic granular chains". *Physical Review E,* **82**(021301), pp. 021301–1–021301–9.

[52] Harbola, U., Rosas, A., Esposito, M., and Lindenberg, K., 2009. "Pulse propagation in tapered granular chains: An analytic study". *Physical Review E,* **80**(031303), September, pp. 031303–1–031303–10.

[53] Starosvetsky, Y., and Vakakis, A. F., 2010. "Traveling waves and localized modes in one-dimensional homogeneous granular chains with no precompression". *Physical Review E,* **82**(026603), pp. 026603–1–026603–14.

[54] Poulton, C. G., Movchan, A. B., McPhedran, R. C., Nicorovici, N. A., and Antipov, Y. A., 2000. "Eigenvalue problems for doubly periodic elastic structures and phononic band gaps". *Proceedings of the Royal Society London,* **456**, pp. 2543–2559.

[55] Romeo, F., and Rega, G., 2006. "Wave propogation properties in oscillatory chains with cubic nonlinearities". *Chaos, Solitons, and Fractals,* **27**, February, pp. 606–617.

[56] Narisetti, R. K., Leamy, M. J., and Ruzzene, M., 2010. "A perturbation approach for predicting wave propagation in one-dimensional nonlinear periodic structures". *Journal of Vibration and Acoustics,* **132**, June, pp. 031001–1–031001–11.

[57] Boechler, N., Daraio, C., Narisetti, R., Ruzzene, M., and Leamy, M. J., 2009. "Analytical and experimental analysis of bandgaps in nonlinear one-dimensional periodic structures". In IUTAM, Symposium on Recent Advances of Acoustic Waves in Solids, T.-T. Wu and C.-C. Ma, eds., 26, Springer Netherlands, pp. 209–219.

[58] Greene, J. B., and Karioris, F. G., 1970. "Force on a magnetic dipole". *American Journal of Physics,* **39**, pp. 172–175.

[59] Boyer, T. H., 1988. "The force on a magnetic dipole". *American Journal of Physics,* **56**(8), pp. 688–692.

[60] Yung, K. W., Landecker, P. B., and Villani, D. D., 1998. "An analytic solution for the force between two magnetic dipoles". *Magnetic and electrical Separation,* **9**, pp. 39–52.

[61] Fornasini, P., 2008. *The Uncertainty in Physical Measurements: An Introduction to Data Analysis in the Physics Laboratory.* Springer.

[62] Furlani, E. P., 2001. *Permanent Magnet And Electromechanical Devices.* Academic Press.

[63] Mann, B. P., Barton, D. A. W., and Owens, B. A. M., 2012. "Uncertainty in performance for linear and nonlinear energy harvesting strategies". *Journal of Intelligent Material Systems and Structures,* **23**, pp. 1451–1460.

[64] Lazarov, B. S., and Jensen, J. S., 2007. "Low-frequency band gaps in chains with attached non-linear oscillators". *International Journal of Non-Linear Mechanics,* **42**, pp. 1186–1193.

[65] Bernard, B. P., Owens, B. A. M., and Mann, B. P., 2013. "Uncertainty propagation in the band gap structure of a 1d array of magnetically coupled oscillators". *Journal of Vibration and Acoustics,* **135**(4), August, p. 041005.

[66] Hoogeboom, C., Man, Y., Boechler, N., Theocharis, G., Kevrekidis, P. G., Kevrekidis, I. G., and Daraio, C., 2013. "Hysteresis loops and multi-stability: From periodic orbits to chaotic dynamics (and back) in diatomic granular crystals". *EPL,* **101**(44003), pp. 44003–1–44003–6.

[67] Boechler, N., Theocharis, G., and Daraio, C., 2011. "Bifurcation-based acoustic switching and rectification". *Nature Materials,* **10**, pp. 665–668.

[68] D'Ambroise, J., Kevrekidis, P. G., and Lepri, S., 2012. "Assymmetric wave propagation through nonlinear pt-symmetric oligomers". *Journal of Physics A: Mathematical and Theoretical,* **45**(444012), pp. 444012–1–444012–16.

[69] Lepri, S., and Malomed, B. A., 2013. "Symmetry breaking and restoring wave transmission in diode-antidiode double chains". *Physical Review E,* **87**(042903), pp. 042903–1–042903–6.

[70] Zhou, W., Taysing-Lara, M., Dang, G., Harrison, L., Mackie, D., Ervin, M., and Newman, P. G., 2004. "Design and fabrication of a reconfigurable photonic bandgap waveguide device with mems features". In Conference on Lasers and Electro-Optics, Vol. 1, Optical Society of America, p. CWG3.

[71] Zhou, W., Mackie, D., Taysing-Lara, M., Dang, G., and Newman, P. G., 2005. "Novel reconfigurable semiconductor photonic bandgap-mems device". In 2005 International Semiconductor Device Research Symposium.

[72] Boechler, N., Yang, J., Theocharis, G., Kevrekidis, P. G., and Dario, C., 2011. "Tunable vibrational band gaps in one-dimensional diatomic granular crystals with three-particle unit cells". *Journal of Applied Physics,* **109**(074906), April, pp. 074906–1–074906–7.

[73] xiang Sun, H., yi Zhang, S., and ji Shui, X., 2012. "A tunable acoustic diode made by a metal plate with periodical structure". *Applied Physics Letters,* **100**(103507), pp. 103507–1–103507–4.

[74] Ziolkowski, R. W., 2003. "Fdtd simulations of reconfigurable electromagnetic band gap structures for millimeter wave applications". *Progress in Electromagnetics Research,* **41**, pp. 159–183.

[75] Na, J., 2012. "Bifurcations of traveling wave solutions for a class of nonlinear evolutions". *Applied Mathematical Sciences,* **6**(88), pp. 4381–4386.

[76] Doney, R., and Sen, S., 2005. Ordered and highly scalable granular media for shock mitigation. Tech. rep., Army Research Laboratory, September.

[77] Bernard, B. P., Peyser, J. W., Mann, B. P., and Arnold, D. P., 2012. "Using the mass ratio to induce band gaps in a 1d array of nonlinearly coupled oscillators". In Proceedings of the ASME 2012 International Design Engineering Technical Conferences, pp. 1–5. Chicago, IL.

[78] Hussein, M. I., Hulbert, G. M., and Scott, R. A., 2006. "Dispersive elastodynamics of 1d banded materials and structures: analysis". *Journal of Sound and Vibration,* **289**, pp. 779–806.

[79] Lydon, J., Jayaprakash, K. R., Ngo, D., Starosvetsky, Y., Vakakis, A. F., and Daraio, C., 2013. "Frequency bands of strongly nonlinear homogeneous granular systems". *Physical Review E,* **88**, p. 012206.

[80] Fath, G., 1998. "Propagation failure of traveling waves in a discrete bistable medium". *Physica D,* **116**, pp. 176–190.

[81] Hussein, M. I., Hulbert, G. M., and Scott, R. A., 2007. "Dispersive elastodynamics of 1d banded materials and structures: Design". *Journal of Sound and Vibration,* **307**, pp. 865–893.

[82] Qian, Z.-H., Jin, F., Li, F.-M., and Kishimoto, K., 2008. "Complete band gaps in two-dimensional piezoelectric phononic crystals with 1-3 connectivity family". *International Journal of Solids and Structures,* **45**, April, pp. 4748–4755.

[83] Wang, Y.-Z., Li, F.-M., Kishimoto, K., Wang, Y.-S., and Huang, W.-H., 2009. "Elastic wave band gaps in magnetoelectroelastic phononic crystals". *Wave Motion,* **46**, August, pp. 47–56.

[84] Ruzzene, M., and Baz, A., 2000. "Control of wave propagation in periodic composite rods using shape memory inserts". *Journal of Vibration and Acoustics,* **122**, April, pp. 151–159.

[85] Wang, Y., Song, W., Sun, E., Zhang, R., and Cao, W., 2014. "Tunable passband in one-dimensional phononic crystal containing a piezoelectric $0.62pb(mg_{1/3}nb_{2/3})o_3 - 0.38pbtio_3$ single crystal defect layer". *Physica E,* **60**, February, pp. 37–41.

[86] Puglisi, G., and Truskinovsky, L., 2000. "Mechanics of a discrete chain with bistable elements". *Journal of the Mechanics and Physics of Solids,* **48**, pp. 1–27.

[87] Bernard, B. P., and Mann, B. P., 2013. "Passive band-gap reconfiguration born from bifurcation asymmetry". *Physical Review E,* **88**(5), November, p. 052903.

[88] Hedrick, T. L., 2008. "Software techniques for two- and three-dimensional kinematic measurements of biological and biomimetic systems". *Bioinspiration & Biomimetics,* **3**, p. 034001.

[89] Bernard, B. P., Greenstein, J. E., and Mann, B. P., 2013. "Energy absorption in a 1d array of axially aligned pendulums with linear torsional coupling". In Proceedings of the ASME 2013 International Mechanical Engineering Congress and Exposition, no. 64470. San Diego, CA.

[90] Tang, L., Yang, Y., and Soh, C. K., 2010. "Toward broadband vibration-based energy harvesting". *Journal of Intelligent Material Systems and Structures,* **21**(18), pp. 1867–1897.

[91] Twiefel, J., and Westermann, H., 2013. "Survey on broadband techniques for vibration energy harvesting". *Journal of Intelligent Material Systems and Structures,* **24**(11), p. 1291.

[92] Harne, R. L., and Wang, K. W., 2013. "A review of the recent research on vibration energy harvesting via bistable systems". *Smart Materials and Structures,* **22**(12), p. 023001.

[93] Liu, H., Lee, C., Kobayashi, T., Tay, C. J., and Quan, C., 2012. "Piezoelectric mems-based wideband energy harvesting systems using a frequency-up-conversion cantilever stopper". *Sensors and Actuators A: Physical,* **186**, pp. 242–248.

[94] Challa, V. R., Prasad, M. G., and Fisher, F. T., 2011. "Towards an autonomous self-tuning vibration energy harvesting device for wireless sensor network applications". *Smart Materials and Structures,* **20**, pp. 025004–1–025004–11.

[95] Challa, V. R., Prasad, M. G., Shi, Y., and Fisher, F. T., 2008. "A vibration energy harvesting device with bidirectional resonance frequency tunability". *Smart Materials and Structures,* **17**, pp. 015035–1–015035–10.

[96] Tang, X., and Zuo, L., 2011. "Enhanced vibration energy harvesting using dual-mass systems". *Journal of Sound and Vibration,* **330**(21), pp. 5199–5209.

[97] Wu, H., Tang, L., Yang, Y., and Soh, C. K., 2013. "A novel two-degrees-of-freedom piezoelectric energy harvester". *Journal of Intelligent Material Systems and Structures,* **24**(3), pp. 357–368.

[98] Litak, G., Friswell, M. I., Kwuimy, C. A. K., Adhikari, S., and Borowiec, M., 2012. "Energy harvesting by two magnetopiezoelestic oscillators with mistuning". *Theoretical & Applied Mechanics Letters,* **2**(043009), pp. 043009–1–043009–5.

Biography

Brian Bernard was born on April 28, 1980 in Buffalo, NY. He received his BSE in Mechanical Engineering from Tulane University in New Orleans, LA in May 2002. He was commissioned as a Naval Officer in September 2002 after completion of Officer Candidate School in Pensacola, FL. Brian then spent 12 months at the Naval Nuclear Power Training Command and Nuclear Prototype Training Unit in Charleston, SC before reporting to the fast attack submarine USS Albany (SSN 753) where he held the positions of Chemical and Radiological Controls Assistant and Assistant Weapons Officer. Brian's final tour of duty in the Navy brought him to Philadelphia, PA where he was an instructor at the University of Pennsylvania Naval Science Department from 2007-2009.

Brian entered Duke's PhD program in 2009 with a James B. Duke fellowship and joined Dr. Brian Mann's Dynamical Systems Laboratory in 2011. During completion of his PhD, Brian has won numerous paper and presentation awards including an NSF travel grant to the 2013 ASME International Mechanical Engineering Congress & Exposition (IMECE) where he also won the Best Student Paper award in the Noise, Control and Acoustics division. He was named as a Preparing Future Faculty fellow in 2013 and completed a Certificate in College Teaching with his degree. Following his PhD, Brian will assume the position of Assistant Professor of Engineering at Schreiner University in Kerrville, TX.